Radical Kinetics and Its Control in Chemical Vapor Deposition of Amorphous, Microcrystalline and Polycrystalline Silicon Thin Films(Dissertation_全文)

AUTHOR(S):

Shirafuji, Tatsuru

Radical Kinetics and Its Control in Chemical Vapor Deposition of Amorphous, Microcrystalline and Polycrystalline Silicon Thin Films

1998

Tatsuru Shirafuji

Abstract

This thesis describes the roles of radicals in silicon chemical vapor deposition (CVD) using excited species generated in photo-CVD and plasma-enhanced CVD (PE-CVD). The thesis consists of 6 chapters.

In chapter 1, as an introduction, historical overview is described for understanding known facts concerning the radical kinetics in the silicon CVD.

In chapter 2, photo-CVD of a-Si:H thin films is presented, because photo-excited processes utilize only neutral radicals without charged ions and electrons, and they construct simple system in comparison to PE-CVD. Therefore, radical kinetics can be predicted only by solving rate equations for known reactions, and complex plasma physics is not required. In this chapter, before performing modeling and simulating photo-CVD system, it is presented that high quality a-Si:H films are obtained by using Xe resonance lamp (wavelength 147 nm) as a vacuum ultraviolet light source and Si_2H_6 as a source gas.

In chapter 3, the modeling and simulation are carried out for the purpose of understanding the reason why the combination of Si_2H_6 + 147 nm can prepare such high quality a-Si:H films. For comparison, the other combinations of SiH_4 + 147 nm and Si_2H_6 + 147 nm are also investigated. From the gas-phase and surface reaction simulations, it is shown that film quality is improved by suppressing contribution of biradicals such as SiH_2 and Si_2H_4, and by promoting contribution of monoradicals such as SiH_3 and Si_2H_5.

In chapter 4, the gas-phase reaction model constructed in the previous chapter is improved to be able to handle realistic PE-CVD of a-Si:H by using a local field approximation method. The density of SiH_2 radicals is measured by using an intra-cavity laser absorption spectroscopy for verifying gas-phase simulation results. On the basis of detailed analysis of the gas-phase simulation, the cause of increase in SiH_2 radical density with diluting source gas SiH_4 or Si_2H_6 by rare gases such as He, Ar and Xe is explained in terms of increase in dissociation degree of the source gas. Surface reaction simulation method is also improved to be able to handle surface migration of adsorbed precursors

by using a Monte-Carlo method. From the simulation, higher hydrogen concentration and formation of Si-H_2 bonds in the films deposited under higher SiH_2 radical composition are explained in terms of reduction of cross-linking reaction frequency due to surface roughness caused by higher sticking probability of SiH_2 radicals. The predicted growth schemes for different radical compositions show good agreement to the experimental results observed by using *in situ* ellipsometry.

In chapter 5, radical kinetics in poly-Si PE-CVD using SiF_4, SiH_4 and H_2 is investigated using both of *in situ* monitoring of the CVD process and its simulation. On the basis of the results obtained from the process monitoring and simulation, it is shown that major deposition precursor, crystalline-growth-promoting precursor and crystalline-nucleation-promoting precursor is SiH_3, F and H radicals, respectively.

In chapter 6, the present work is summarized and future aspects are presented.

Acknowledgments

I would like to express my deep gratitude to two Professors of Kunihide Tachibana and Hiroyuki Matsunami for their continuous guidance, encouragement, and critical supervision throughout this work. I am grateful to Professor Kenji Hashimoto for a critical reading of the manuscript and valuable comments on it from the view point of chemical engineering which I have tried to apply to semiconductor engineering in this thesis. I am indebted to Associate Professor Takashi Fuyuki who has supported and encouraged me for developing photo-CVD system, and to Associate Professor Yasuaki Hayashi who has supported me for developing *in situ* ellipsometry system and gave me valuable suggestions and techniques on the ellipsometry. I also wish to thank to Research Associate Masahiro Yoshimoto for his guide to the amorphous silicon research field and valuable suggestions in the field. Special thanks are due to Mr. Mikio Yamamuka and Mr. Wei-Ming Chen for their co-operation in simulation program development. Thanks are also due to Mr. Satoru Ohshima, Mr. Sagara Nakajima, Mrs. Yun-Fen Wang, Mr. Takeshi Genji, Mr. Tadashi Miyagi, Mr. Hisao Kondo, Mr. Shinji Nakajima and Mr. Mahito Sawada for their kind help in experiments. I thankfully acknowledge Dr. Yasuji Matsui and Dr. Akimasa Yuuki in Mitsubishi Co. Ltd. for their practical help in simulation and ICLAS, Dr. M. Taki for offering disk shaped VUV light source, and Mr. Shuhei Tsuchimoto and Mr. Tatsuo Morita in Sharp Corp. for offering plasma-CVD chamber.

Contents

Chapter 1

Introduction

Plasma enhanced chemical vapor deposition (PE-CVD) method can prepare silicon thin films in the form of amorphous (a-Si), microcrystalline (μc-Si) and polycrystalline (poly-Si). It should be noted that these films can be prepared, in comparison to conventional epitaxial growth, at lower temperature and on non-crystalline substrates available in larger size. This technique, therefore, now forms the basis for so-called 'Giant Microelectronics' consisting of large-area devices such as solar cells, linear sensors, thin film transistors and xerography. Deposition mechanisms of the films, however, have not been fully understood yet, even though research activity for them has been proceeding for two decades. This situation is mainly due to complex physics and chemistry in the plasma and on growing film surface. This thesis describes some results for understanding the plasma process for the deposition of silicon thin films on the basis of *in situ* gas-phase and surface diagnostics and reaction simulation. In this chapter, I present briefly historical overview of the research activity on silicon thin film deposition with the PE-CVD and related preparation methods, and explain the objectives and scope of this work. Finally I describe the constitution of this thesis.

1.1 PE-CVD of silicon thin films

The origin of recent development on PE-CVD of silicon thin films as an electronic material can be traced back to several important discoveries in the history of amorphous silicon technology.

The first one was preparation of hydrogenated amorphous silicon (a-Si:H) by Spear and Le Comber in 1975 [1, 2]. They discovered that glow-discharge decomposition of SiH_4 could make amorphous silicon thin films to either n- or p-type by substitutional doping from gas phase, while evaporated or sputtered

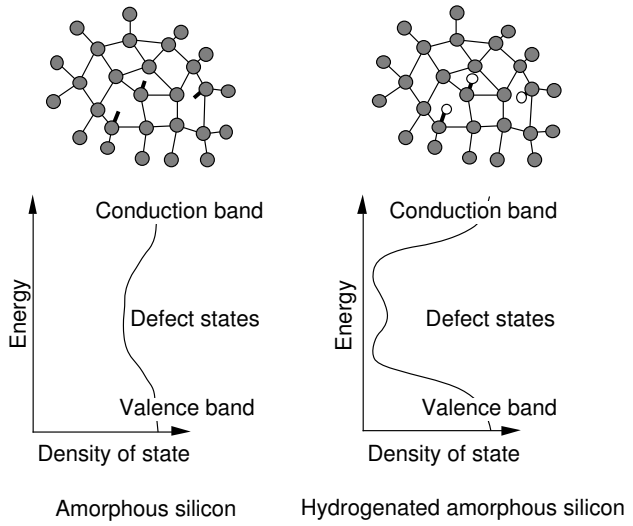

Fig. 1.1: Schematic representation of the structure of non-hydrogenated amorphous silicon and hydrogenated amorphous silicon, and their energy band diagram.

films in early work could not make due to a large density (10^{19}–10^{20} cm^{-3}) of dangling bonds and corresponding mid-gap states [3]. The dopability of PE-CVD films was found to be associated with the fact that the films contain 8–20 at.% hydrogen which terminates dangling bonds to reduce their density ($<10^{16}cm^{-3}$) and modifies whole structure [4] as shown in Fig.1.1.

The second one was preparation of hydrogenated microcrystalline silicon (μc-Si:H) by Matsuda *et al.* in 1980. They discovered that the PE-CVD could prepare the films containing crystalline phase at low substrate temperature of 200°C from highly H_2-diluted SiH_4 discharge [5]. The μc-Si films were composed of small crystalline grain with an average size of 30–200Å embedded in an amorphous matrix, and the dangling bonds surrounding the grain were terminated with hydrogen [6] as shown in Fig.1.2. They also clarified that the highly conductive fluorinated films (a-Si:H:F), which Ovshinsky and Madan had prepared from SiH_4 and SiF_4 [7, 8], had the same film structure.

The third one was by Shibata *et al.* in 1987 [9, 10], concerning preparation of polycrystalline silicon (poly-Si) which was characterized by a somewhat larger average grain size of typically 400–1000Å. They discovered that the polycrystalline silicon could be prepared at low temperature of 300°C through the reactions of SiF_4 with H radicals supplied from microwave discharge of H_2, and even epitaxial growth could be achieved on <100> oriented crystalline silicon substrates. They termed this method as Hydrogen-Radical-Enhanced CVD (HR-CVD). In 1991, Mohri *et al.* demonstrated the preparation of poly-

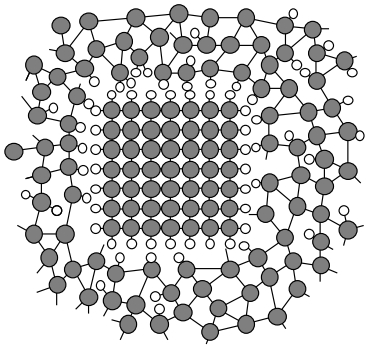

Fig. 1.2: Schematic representation of the structure of hydrogenated microcrystalline amorphous silicon.

Si at the same temperature by a conventional glow-discharge PE-CVD method using $SiH_4/SiF_4/H_2$ gas mixture [11]. Although, in 1979, Morin and Morel had demonstrated the possibility of preparing poly-Si by SiF_4/SiH_4 RF glow discharge at substrate temperature of higher than 450°C [12], it was clearly the work of the Shimizu's group [9, 10] that triggered the development of low temperature poly-Si growth from fluorinated precursors.

1.2 Diagnostics

1.2.1 Gas-phase process

Physical properties of plasma-deposited silicon thin films are sensitively influenced by discharge conditions such as pressure, gas flow rate, power and so on. Since numerous variants of plasma reactors are widely used, the deposition conditions must be optimized for the respective system. The material properties are, even now, empirically controlled by finding a good combination of the deposition parameters. Therefore, *in situ* observations of chemical species in gas phase was attempted for obtaining satisfactory reproducibility of the film properties and for more general understanding of the plasma chemistry.

The ionic and neutral species in the plasma can be investigated by means of mass spectrometry (MS), which has been applied to SiH_4 plasma for the first time by Drévillon *et al.* [13], Haller [14] and Turban *et al.* [15] in 1980. The common conclusion drawn from the MS was that the most dominant ions was SiH_3^+ and its density was $10^8 - 10^9$ cm^{-3} which was close to electron density. Although they could not observe neutral free radicals directly, Turban *et al.* concluded that such radicals must be responsible for film deposition, since the

ion flux was one to two orders of magnitude low to explain the deposition rate. This was confirmed by Matsuda *et al.* [16]. They measured a relative density of ionic species and neutral species in the realistic plasma condition of a-Si:H deposition using the MS under the ionizer-on and -off operations, and the density of ionic species was estimated to be lower by three or four orders of magnitude than the neutral species. Most of the researchers after that, therefore, fixed their eyes on the neutral species.

Kampas and Griffith [17], Hamasaki *et al.* [18], and Matsuda *et al.* [19] applied optical emission spectroscopy (OES) to the diagnostics of neutral species for the first time in 1980. However, this technique can detect only the light-emitting excited species, such as Si^*, SiH^*, H^* and H_2^*. At that time, many researchers correlated the emission intensity of these species to the film deposition rate and properties. However, the density of Si^* and SiH^* of excited states in the steady-state plasma was estimated to be 10^6–10^7 cm^{-3} using their optical transition probabilities [19]. These values were also lower by five or six orders of magnitude than the density (10^{12} cm^{-3}) of species required for explaining the observed deposition rate of a-Si:H. Due to this fact, researchers' eyes were turned upon neutral radicals in their ground states.

Detection of the ground-state species by means of spectroscopic methods requires excitation of the species from outside the plasma. Schmitt *et al.* [20] applied a laser induced fluorescence spectroscopy (LIFS) for the measurement of these species in 1984, and Matsumi *et al.* [21] revealed in 1986 that the density of Si and SiH was too low to explain the total deposition rate of a-Si:H within conventional deposition conditions. Consequently, it was speculated that the main precursors for the film deposition were likely to be neutral SiH_2 and SiH_3.

Hata *et al.* [22] applied a coherent anti-Stokes Raman Spectroscopy (CARS) for the detection of such neutral species in 1986. Although they could detect high-density (10^{14} cm^{-3}) species such as SiH_4, H_2 and Si_2H_6, they could not detect SiH_2 and SiH_3. Yamada *et al.* [23] had reported detection of SiH_2 and SiH_3 using an infrared laser absorption spectroscopy (IRLAS), and Itabashi *et al.* [24] in the same group applied this technique to realistic PE-CVD in 1988. They measured the density of SiH_3 to be in the order of 10^{12} cm^{-3} which could explain the deposition rate. Regarding SiH_2, however, they could not determine its density and only the upper limit of 5×10^9 cm^{-3} was estimated, because its density was lower than the detection limit of the IRLAS. The

absolute density of SiH_2 has been determined for the first time by Tachibana *et al.* using an intracavity laser absorption spectroscopy (ICLAS) which is described in this thesis, and it has been apparent to be in the order of 10^9 cm^{-3} [25].

1.2.2 Surface process

The surface, at which deposited film structure is finally determined, is the most important part of the deposition process. Diagnostics for the surface, however, was not so sophisticated as in the case of gas-phase diagnostics. Most of the conventional surface analysis techniques require ultra high vacuum (UHV) condition, as in Auger electron spectroscopy, X-ray photoelectron spectroscopy, reflection high energy electron diffraction and so on. These electron probes are generally incompatible with the reactive environment of the PE-CVD. A more promising approach is use of the optical probes, such as infrared reflection absorption spectroscopy (IR-RAS), ellipsometry and so on.

Application of ellipsometric analysis to *in situ* monitoring of thin film growth was proposed in 1980 by Theeten *et al.* [28, 29]. They applied a conventional rotating analyzer ellipsometry (RAE) to the vapor phase growth of GaAs, and demonstrated the observation of nucleation and growth sequences during the process. Drévillon applied this technique to *in situ* observation of a-Si:H deposition process by means of a fast polarization modulated ellipsometry (PME) in 1982 [30], and revealed that similar phenomena of nucleation and microstructural evolution were observed also in the a-Si:H deposition process [31]. Collins *et al.* demonstrated that the phenomena observed by the fast PME could be observed by using relatively slower conventional RAE [32], and expanded applicability of this technique toward growth of μc-Si [33].

Although ellipsometry is fast and reveals microstructural evolution and composition of the growing film, it does not contain any information concerning chemical bonds. In order to fully understand and improve film properties, we must obtain information concerning chemical reactions occurring on the growing film surface in addition to its microstructure. Before Wadayama *et al* applied an IR-RAS to *in situ* observation of the surface in 1988 [34], Matsuda *et al.* empirically proposed reaction mechanisms on the growing film surface by means of so-called radical-separation method in 1986 [35]. They confined plasma in a limited region above a substrate by placing a mesh electrode above it, and changed flux density of impinging radicals by changing the distance

from the bottom of the plasma region and the substrate. At the moment, the most dominant radical was believed to be SiH_3, and they constructed their model as the reaction of SiH_3 with the surface. From the observation of the square raw in the SiH_3 flux density dependence of the deposition rate, they deduced following bimolecular reactions for the film deposition,

$$\text{Si-H} + \text{SiH}_3 \rightarrow \text{Si-} + \text{SiH}_4 \tag{1.1}$$

$$\text{Si-} + \text{SiH}_3 \rightarrow \text{Si-SiH}_3 \tag{1.2}$$

Under the condition of elevated temperature, excess hydrogen was considered to desorb out through, for example, following reactions,

$$\text{Si-SiH}_3 + \text{Si-SiH}_3 \rightarrow \text{Si-SiH}_2\text{-SiH}_2\text{-Si} + \text{H}_2 \tag{1.3}$$

$$\text{Si-SiH}_3 \rightarrow \text{Si-SiH} + \text{H}_2 \tag{1.4}$$

Although *in situ* IR-RAS observation of the species such as $SiH_n(n{=}1\text{–}3)$ was performed by Wadayama *et al.* [34], its infrared absorption was caused by Si-H_n not only at the top surface but also in the bulk film. In 1990, Toyoshima *et al.* successfully distinguished absorptions of top surface and bulk region [36, 37]. They revealed that hydrogen bonding configuration of the growing film surface changes with substrate temperature, and the temperature higher than 400°C was accompanied with hydrogen desorption from the top surface. This observation became the most important one for supporting surface reaction models deduced by Matsuda *et al.* These reports triggered development of numerical modeling and simulation of surface reactions aiming at the prediction of structural properties of deposited films.

1.3 Modeling and simulation

In principle, PE-CVD of silicon thin films can be divided to three sequential processes.

(a) Primary process: The electron collisions which produce the reactive species such as ions and radicals according to the collision cross section, namely, electron impact dissociation,

(b) Gas-phase process: The gas-phase reactions which these species undergo during diffusion and drift to the surfaces, namely, secondary reactions and mass transport,

(c) Surface process: the surface reactions involved in film growth, namely, thin film deposition.

If these processes were connected sequentially, the modeling of PE-CVD would be rather easy. In reality, however, these are not. For example, source gas density changes with its electron impact dissociation and secondary reactions, the species produced through these processes also collide with electrons, and this process changes electron energy distribution. Therefore, research on the modeling and numerical simulation started almost simultaneously with the gas phase diagnostics in order to explain measured results or to predict them.

1.3.1 Primary process

Although quantitatively dominant species have already been known to be neutral radicals, there exist important species of ions and electrons which sustain plasma itself. Electrons in the plasma play an important role at the primary process of electron impact dissociation and ionization of parent gas molecules [38]. The rate constant of the dissociation and ionization is determined by electron impact cross sections, which have been measured and compiled as a function of electron energy by many workers [39]. Electron energy is basically determined by the acceleration in the electric field and/or magnetic field in the plasma. This can be predicted by solving Boltzmann transport equation or Monte Carlo simulation [40–42]. The electric field, however, is determined by the density distribution of electrons themselves and the ions produced by the electrons.

As can be understood from above consideration, the parameters concerning electrons, ions and field are not determined straight forward, but recursively. In order to predict these parameters in the plasma, therefore, we must perform numerical simulation by iterating solution of rate equations until stable solution is obtained. Recent progress of computational power has enabled us to perform the simulation within a reasonable time. My major interest is not details of the plasma structure, but density and flux of the neutral radicals. In this thesis, therefore, I used the most simple model known as a local field approximation proposed by Boeuf [43]. This model is not so powerful to describe the details of the plasma, but is enough to estimate the electric field and density and energy distribution of electrons which is important parameters to calculate primary reaction rate constant.

1.3.2 Secondary process

The first attempt for the modeling was made by Turban *et al.* in 1979 [44]. In their model, however, the primary processes were simplified into an electron-molecule reaction to produce only neutral radicals, which are treated as one active species. The dissociation rates were calculated with a semi-empirical rate constant independent on electron energy.

In order to perform totally self consistent simulation, data sets of electron collision cross section for SiH_4 were required at first. A set of cross sections of SiH_4 was obtained by Kline in 1982 [45] and Garscadden *et al.* in 1983 [46].

In 1982, Turban *et al.* determined cross section to produce ionized species of $SiH_n^+(n{=}0\text{–}3)$ [47], in which production of SiH_2^+ and SiH_3^+ showed the highest cross section value. In the same year, Perrin *et al.* determined total dissociation cross section [48], but each cross section value to produce $SiH_n(n{=}0\text{–}3)$ was not measured, and it was deduced by using the branching ratio on the basis of results on the ionization cross section.

In 1984, Tachibana presented a quasi-steady-state plasma chemistry model and its simulation for RF discharge in SiH_4 [49]. He obtained electron impact rate constants by convolving a semi-empirical electron distribution function with reported cross sections. Although the neutral chemistry and ion-molecule reactions in his model were treated in a self-consistent manner, the electron density was an input parameter whose value was based on experimental electrical probe measurements. He concluded that SiH_3 is the most abundant gas phase radical.

In 1988, Kushner presented a totally self-consistent model for the PE-CVD of a-Si:H in RF glow discharge in SiH_4/Ar mixture [50]. He obtained spatio-temporal dependence of electron impact rate constants by using a Monte Carlo simulation with a set of cross section data. By this method, he could treat the plasma chemistry with no assumptions concerning parameters such as the electron distribution function, dissociation rate, reactor geometry or reaction chain.

1.3.3 Final process

After the quantitatively dominant species were revealed to be neutral radical species of SiH_2 and SiH_3, several models for describing surface reactions were proposed. In the early years, surface reactions were believed to be similar to

those for thermal CVD, in which dominant radical was SiH_2 and it contributed to the film deposition. In 1981, Kampas *et al.* proposed following reaction scheme for film formation [51],

$$\text{Si-H}_{(s)} + \text{SiH}_{2(g)} \rightarrow \text{Si-SiH}_{3(s)}, \tag{1.5}$$

$$\text{Si-H}_{3(s)} + \text{Si-H}_{(s)} \rightarrow \text{Si-SiH}_{2(s)} + \text{H}_2, \tag{1.6}$$

on the basis of well known insertion reaction,

$$\text{SiH}_{4(g)} + \text{SiH}_{2(g)} \rightarrow \text{Si}_2\text{H}_{6(g)}. \tag{1.7}$$

However, SiH_2 was known to be highly reactive. In 1979, Perkins *et al.* had already suggested that such reactive radical cannot reach substrate surface through the crowd of parent source gas [52]. Brodsky *et al.* in 1980 [53] and Knights in 1981 [54] demonstrated a-Si:H deposition through the reaction of SiH_4 and atomic hydrogen, which was known to produce SiH_3 selectively as follows,

$$\text{SiH}_4 + \text{H} \rightarrow \text{SiH}_3 + \text{H}_2. \tag{1.8}$$

In 1983, Robertson *et al.* finally revealed the most abundant radical reaching substrate was SiH_3 from the results of threshold ionization mass spectroscopy [55].

Based on the above reports and simplified description of the surface reactions proposed by Matsuda *et al.*, Gleason *et al.*, in 1987, performed Monte Carlo simulation of the surface reactions in order to predict hydrogen content and the density of the deposited films [56]. Almost the same time, Kushner also performed more sophisticated surface reaction simulation although his model was phenomenological one [57]. McCaughy and He have improved their model by changing from the phenomenological one to Monte Carlo simulation, and revealed that contribution of high sticking probability species results in rough surface [58]. However, they did not give any experimental proofs of the predicted results. This will be presented in this thesis.

1.4 Scope of the thesis

Despite the huge number of research works concerning PE-CVD of silicon thin films, roles of each radicals impinging onto growing film surface are still not so clear that film properties can be predicted numerically. In order to clarify the roles of radicals on the film growth, it is required to investigate

correlation between film properties and gas-phase neutral radical composition. Realistic PE-CVD, however, is accompanied with the effect of ions in addition to neutral radicals although ion density is lower than radical density, and it may disturb pure radical effects. In this work, therefore, prototype of the model of gas-phase reactions is developed for the photo-CVD in which ions are not produced. After the verification of the applicability of the model, it is modified to the form which can handle PE-CVD.

Regarding the deposition of μc-Si and poly-Si, the deposition conditions are fairly different from typical a-Si:H deposition conditions, and hydrogen radical and fluorine containing radicals contribute to the appearance of crystalline phase in addition to SiH_3 which contribute to the deposition of a-Si:H. Roles of these radicals are not so understood than SiH_3 in the deposition of a-Si:H. In this work, therefore, I have investigated the effects of hydrogen radicals and fluorine containing radicals by using *in situ* ellipsometry and gas-phase reaction simulation technique.

1.5 Constitution of the thesis

In chapter 2, it is demonstrated that high quality a-Si:H films are prepared by the photo-CVD method in which Si_2H_6 and 147 nm are used as the combination of a source gas and excitation wavelength instead of conventional Si_2H_6 and 185 nm from a Hg lamp. In chapter 3, the properties of the films prepared with Si_2H_6 + 147 nm are compared to those with the other combinations of SiH_4 + 147 nm and Si_2H_6 + 185 nm, and effects of excitation wavelengths and source gases on the film properties are discussed with the aid of a numerical simulation of gas-phase and surface reactions. In chapter 4, the model developed in chapter 3 is modified to be applicable to PE-CVD of a-Si:H, and its results are compared to experimental results of *in situ* radical measurements. Improved surface reaction model is also presented, in which effect of surface roughness has been considered in the model, and compared to real time monitoring of surface conditions with the aid of *in situ* ellipsometry. In chapter 5, these techniques are expanded to the preparation of μc-Si and poly-Si deposition using SiF_4 in addition to SiH_4, and roles of several radicals on the appearance of crystallized phase are discussed. In chapter 6, conclusions of this work are summarized.

References

[1] W. E. Spear and P. G. Le Comber: Solid State Commun. **17** (1975) 1193.

[2] W. E. Spear and P. G. Le Comber: Philos. Mag. **33** (1976) 935.

[3] W. Paul, G. A. N. Connell and R. J. Temkin: Adv. Phys. **22** (1973) 529.

[4] J. C. Knights: *Proc. 10th Conf. Solid State Devices, Tokyo 1978*, Jpn. J. Appl. Phys. **18** Suppl. 18-1 (1979) p. 101.

[5] A. Matsuda, S. Yamasaki, K. Nakagawa, H. Okushi, K. Tanaka, S. Iizima, M. Matsumura and H. Yamamoto: Jpn. J. Appl. Phys. **19** (1980) L305.

[6] A. Matsuda, T. Yoshida, S. Yamasaki and K. Tanaka: Jpn. J. Appl. Phys. **20** (1981) L439.

[7] S. R. Ovshinsky and A. Madan: Nature **276** (1978) 482.

[8] A. Madan, S. R. Ovshinsky and E. Benn: Phil. Mag. B **40** (1979) 259.

[9] N. Shibana, K. Fukuda, H. Ohtoshi, J. Hanna, S. Oda and I. Shimizu: Mater. Res. Soc. Symp. Proc. **95** (1987) 225.

[10] N. Shibata, K. Fukuda, H. Ohtoshi, J. Hanna, S. Oda and I. Shimizu: Jpn. J. Appl. Phys. **26** (1987) L10.

[11] M. Mohri, H. Kakinuma, M. Sakamoto and H. Sawai: Jpn. J. Appl. Phys. **30** (1991) L778.

[12] F. Morin and M. Morel: Appl. Phys. Lett. **35** (1979) 686.

[13] B. Drévillon, J. Huc, A. Lloret, J. Perrin, G. de Rosny and J. P. M.Schmitt: Appl. Phys. Lett. **37** (1980) 646.

[14] I. Haller: Appl. Phys. Lett. **37** (1980) 282.

[15] G. Turban, Y. Catherine and B. Grolleau: Thin Solid Films **67** (1980) 309.

[16] A. Matsuda and K. Tanaka: Thin Solid Films **92** (1982) 171.

[17] F. J. Kampas and R. W. Griffith: Solar Cells **2** (1980) 385.

[18] T. Hamasaki, H. Kurata, M. Hirose and Y. Osaka: Appl. Phys. Lett. **37** (1980) 1084.

[19] A. Matsuda, K. Nakagawa, K. Tanaka, M. Matsumura, S. Yamasaki, H. Okushi and S. Iizima: J. Non-Cryst. Solids **35-36** (1980) 183.

[20] J. P. M. Schmitt, P. Gressier, M. Krishnan, G. de Rosny, J. Perrin: Chem. Phys. **84** (1984) 281.

[21] Y. Matsumi, T. Hayashi, H. Yoshikawa and S. Komiya: J. Vac. Sci. Technol. A **4** (1986) 1786.

[22] N. Hata, A. Matsuda and K. Tanaka: Jpn. J. Appl. Phys. **25** (1986) 108.

[23] C. Yamada and E. Hirota: Phys. Rev. Lett. **56** (1986) 923.

[24] N. Itabashi, K. Kato, N. Nishiwaki, T. Goto, C. Yamada and E. Hirota: Jpn. J. Appl. Phys. **27** (1988) L1565.

[25] K. Tachibana, T. Shirafuji and Y. Matsui: Jpn. J. Appl. Phys. **31** (1992) 2588.

[26] B. E. Hayden: *Vibrational Spectroscopy of Molecules on Surface*, Ed. J. T. Yates, Jr. and T. E. Madey (Prenum Press, New York, 1987) 267.

[27] R. M. A. Azzam and N. M. Bashara: *Ellipsometry and Polarized Light* (North Holland, Amsterdam, 1977).

[28] J. B. Theeten: Surf. Sci. **96** (1980) 275.

[29] F. Hottier and J. B. Theeten: J. Cryst. Growth **48** (1980) 644.

[30] B. Drévillon, J. Perrin, R. Marbot, A. Violet and J. L. Dalby: Rev. Sci. Instrum. **53** (1982) 969.

[31] B. Drévillon: Thin Solid Films **130** (1985) 165.

[32] R. W. Collins, A. H. Clark, S. Guha and C.-Y. Huang: J. Appl. Phys. **57** (1985) 4566.

[33] R. W. Collins: Appl. Phys. Lett. **48** (1986) 843.

[34] T. Wadayama, W. Suëtaka, A. Sekiguchi: Jpn. J. Appl. Phys. **27** (1988) 501.

[35] A. Matsuda and K. Tanaka: J. Appl. Phys. **60** (1986) 2351.

[36] Y. Toyoshima, K. Arai, A. Matsuda and K. Tanaka: Appl. Phys. Lett. **56** (1990) 1540.

[37] Y. Toyoshima, K. Arai, A. Matsuda and K. Tanaka: Appl. Phys. Lett. **57** (1990) 1028.

[38] For example, E. W. McDaniel, *Atomic Collisions Electron and Photon Projectiles* (Wiley, New York, 1989).

[39] For example, M. Hayashi, *Swarm Studies and Inelastic Electron-Molecule Collisions*, Ed. L. C. Pitchford, B. V. McKoy, A. Chutjian and S. Trajmar, (Springer, New York, 1985) p.167.

[40] A. Garscadden, G. L. Duke and W. F. Bailey: Appl. Phys. Lett. **43** (1983) 1012.

[41] M. J. Kushner: J. Appl. Phys. **54** (1983) 4958.

[42] B. M. Penetrante, J. N. Bardsley and L. C. Pitschford: J. Phys. D **18** (1985) 1087.

[43] J. P. Boeuf: Phys. Rev. A **36** (1987) 2782.

[44] G. Turban, Y. Catherine and B. Grolleau: Thin Solid Films **60** (1979) 147.

[45] L. E. Kline: IEEE Trans. Plasma Sci. **PS-10** (1982) 224.

[46] A. Garscadden, G. L. Duke and W. F. Bailey: Appl. Phys. Lett. **43** (1983) 1012.

[47] G. Turban, Y. Catherine and B. Groleau: Plasma Chem. and Plasma Processing **2** (1982) 61.

[48] J. Perrin, J. P. M. Schmitt, G. de Rosny, B. Drévillon, J. Huc and A. Lloret: Chem. Phys. **73** (1982) 383.

[49] K. Tachibana: Proc. 8th Symp. Ion Sources and Ion-Assisted Technol., Ed. Takagi (Institute of Electrical Engineering, Tokyo, Japan, 1984), p.319.

[50] M. J. Kushner: J. Appl. Phys. **63** (1988) 2532.

[51] F. J. Kampas and R. W. Griffith: Appl. Phys. Lett. **39** (1981) 407.

[52] G. G. A. Perkins, E. R. Austin and F. W. Lampe: J. Am Chem. Soc. **101** (1979) 1109.

[53] M. H. Brodsky, I. Haller: IBM Tech. Disclosure Bull. **22** (1980) 3391.

[54] J. C. Knights: Bull. Am. Phys. Soc. **26** (1981) 389.

[55] R. Robertson, D. Hills, H. Chatham and A. Gallagher: Appl. Phys. Lett. **43** (1983) 544.

[56] K. K. Gleason, K. S. Wang, M. K. Chen and J. A. Reimer: J. Appl. Phys. **61** (1987) 2866.

[57] M. J. Kushner: J. Appl. Phys. **62** (1987) 4763.

[58] M. J. McCaughy and M. J. Kushner: J. Appl. Phys. **65** (1989) 186.

Chapter 2

Photochemical vapor deposition of a-Si:H using Si_2H_6 and 147 nm excitation

2.1 Introduction

Since photochemical vapor deposition (photo-CVD) methods have been implemented for the deposition of silicon related materials for the first time [1–4], their major efforts have been to minimize damage due to high temperature in thermal CVD and/or high-energy particles in plasma enhanced CVD (PE-CVD). Concerning a-Si:H deposition, many kinds of photo-CVD methods have been examined for obtaining higher quality films than PE-CVD films from these view points [5–7]. The photo-CVD methods have another advantage that the films are prepared in pure radical chemistry without accelerated ions which interfere especially surface reactions through their bombardment on growing film surface. This fact enable us modeling and simulation of film deposition process by simply solving rate equations.

In this chapter, prior to the modeling and simulation of photo-CVD process, it is described that high quality a-Si:H films can be easily prepared by the photo-CVD method in which Si_2H_6 and 147 nm is used as a source gas and an excitation wavelength, respectively. A mechanism of the high-quality film deposition is described in the next chapter with the aid of gas-phase and surface reaction simulations by making the most of the advantage of the pure-radical-chemistry nature of photo-CVD processes. Since the combination of Si_2H_6 + 147 nm has lead to high quality films, substitutional doping to n- and p-type is also demonstrated for device applications.

2.2 Film preparation

2.2.1 Source gases, wavelengths and windows

Commercially available silicon containing gases are SiH_4, Si_2H_6 and Si_3H_8. Figure 2.1 shows photo absorption cross section spectra of these gases [8, 9].

Although Si_3H_8 shows the highest absorption cross section, it costs too much in contrast to the other gases. SiH_4 is the most utilized gas for the silicon thin film deposition processes, but it does not have enough photo absorption cross section. Therefore, Si_2H_6 is used as a main source gas in the photo-CVD presented in this thesis. In order to excite Si_2H_6 molecules, excitation wavelength must be less than 190 nm, which can be realized by using gas discharge lamps such as Ar (106.7 nm), He_{II} (121.5 nm), H_2 (121.6 nm), Kr (123.6 nm) and Xe (147.0 nm), D_2 (161 nm) or Hg (184.9 nm) as indicated in the same figure [10].

Most researchers have used combination of Si_2H_6 and Hg lamp (185 nm), because the Hg lamp is commercially available. However, its deposition rate is fairly low (0.6–1.5 nm/min) [6, 11] because of quite low photo absorption cross section of Si_2H_6 at 185 nm as shown in Fig.2.1. Higher deposition rate of 330 nm/min can be obtained by increasing photon numbers as in the case of ArF (195 nm) excimer laser photo-CVD [12]. However, obtained film quality is not very good due to too much hydrogen concentration in the films [12]. Therefore, effective decomposition of source-gas molecules by shorter-wavelength light (higher-energy photons) is expected to lead to high deposition rate with keeping high quality.

Although He, H_2 or Kr seem to be the best choice, there are no window materials that have reasonable transmittance with realistic thickness as shown in Fig.2.2 [13]. In this work, therefore, a combination of Xe resonance lamp and MgF_2 window is used for film deposition. The source gas used this chapter is Si_2H_6, because absorption cross section of SiH_4 is fairly low for realizing reasonable deposition rate.

2.2.2 Film preparation procedure

Figure 2.3 shows the photo-CVD apparatus, in which a low-pressure discharge of Xe gas generated by microwave (2.45 GHz) is used for a VUV light source [14]. A quartz tube (30 mm diameter) is inserted into a rectangular waveguide

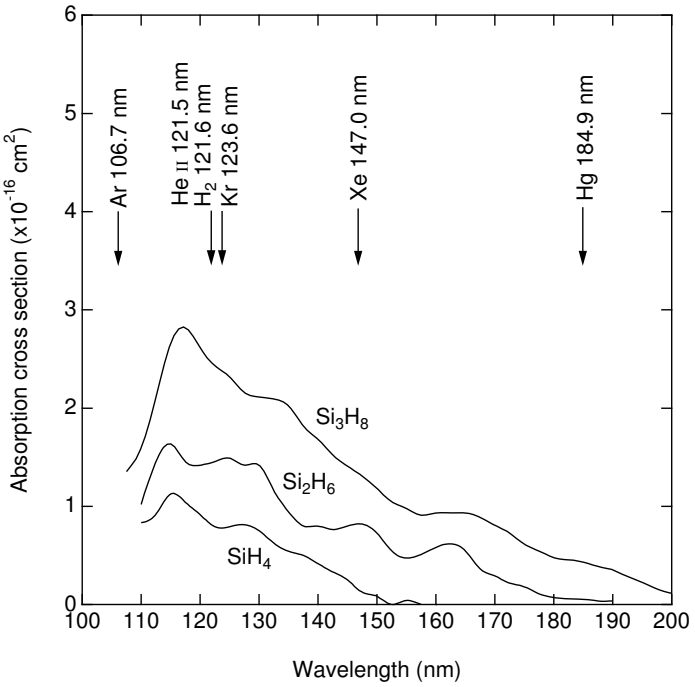

Fig. 2.1: Photo absorption cross section spectra of SiH_4, Si_2H_6 and Si_3H_8 molecules. Emission wavelengths of several gas-discharge lamps are indicated by arrows.

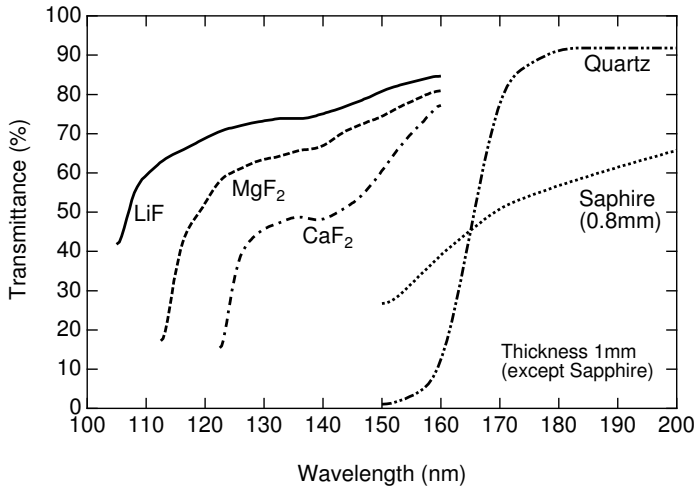

Fig. 2.2: Transmittance spectra of several window materials. Thickness of each window material is 1 mm except sapphire window.

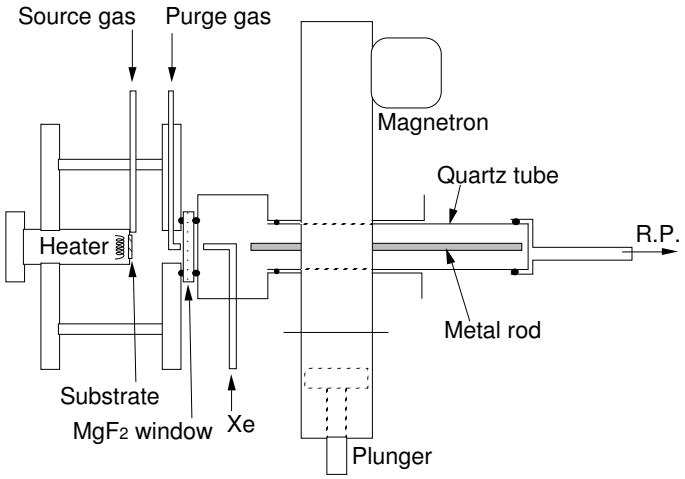

Fig. 2.3: Schematic representation of the photo-CVD apparatus, which consists of two parts of a deposition chamber and a VUV (wavelength 147 nm) light source driven by microwave excitation of Xe gas. The VUV light is fed into deposition chamber through the hole (aperture 24 mm diameter) on which an MgF_2 window (3 mm thick, 35 mm diameter) is mounted.

normally to the H plane. Pressure in the quartz tube are kept constant at 0.1 Torr by controlling the flow rate of Xe and the conductance of the evacuation line of the rotary pump. The typical emission spectrum of the Xe lamp is shown in Fig.2.4 for a pressure of 0.1 Torr and an input power of 100 W. A window made of MgF_2 (3 mm thick, 35 mm diameter) is used between the reaction chamber and the lamp. Effective aperture diameter for feeding the VUV light is 24 mm. Distance between the window and substrate is 40 mm. Although the window is blown with N_2 at a flow rate of 250 cc/min to prevent the deposition of films on it, it is cleaned with the 5-1 etchant (HNO_3:HF=1:5) after each run.

Corning 7059 glass substrates are used for optical (UV and visible region) and electrical characterization of deposited films. Polished crystalline silicon wafers with high resistivity (>40Ωcm, both-sides mirrored) are used for infrared absorption measurements. The glass and silicon substrates are cleaned by isopropyl alcohol, acetone and methyl alcohol in this order. The cleaned silicon substrates are etched by diluted HF (5%) for native-oxide removal and rinsed with de-ionized water. The cleaned glass substrates are rinsed with aqua regia (HNO_3:HCl=3:1) for the purpose of removing heavy metal impurities that might affect on electrical measurements.

Films are deposited using 100% Si_2H_6 with a flow rate of 2.5 sccm. The

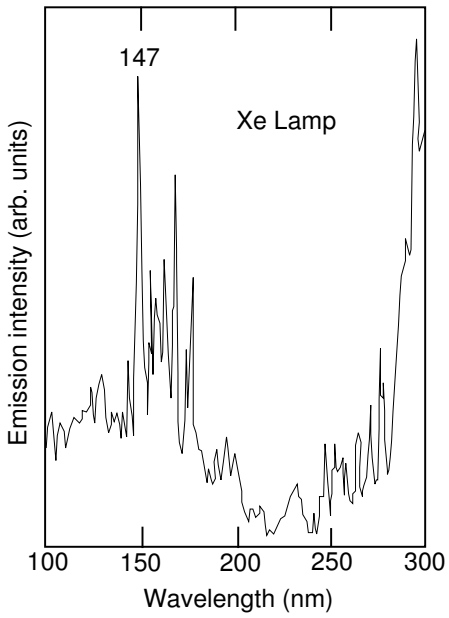

Fig. 2.4: A typical emission spectrum of the Xe lamp operated under the condition of microwave power 100 W and pressure 0.1 Torr.

total pressure of the reaction chamber is 2.0 Torr. Substrate temperature (T_{sub}) is varied in the range of 200–400°C. The typical deposition rate and the thickness of the films is 0.6 nm/min and 300 nm, respectively.

2.3 Properties of a-Si:H films from Si_2H_6 + 147 nm

2.3.1 Electrical and optical properties

Figure 2.5 shows typical temperature dependence of dark conductivity of deposited films, which is shown as a function of reciprocal temperature, namely, as an Arrhenius plot. The Arrhenius-plot characteristics of the films shows good linearity in the range of 30–180°C. This result indicates that activation-type conduction is dominant in the films. In contrast to the hopping conduction in which electrons are transported by the repetition of being captured at a trap and hopping to another trap, electrons are excited (or activated) from valence band to conduction band and transported as free carriers in the activation-type conduction [17]. Therefore, this result suggests low density of traps in the films.

The activation energy E_{act} obtained from the linear region of the Arrhenius plot is shown in Fig.2.6 together with optical energy gap E_{opt} which is deter-

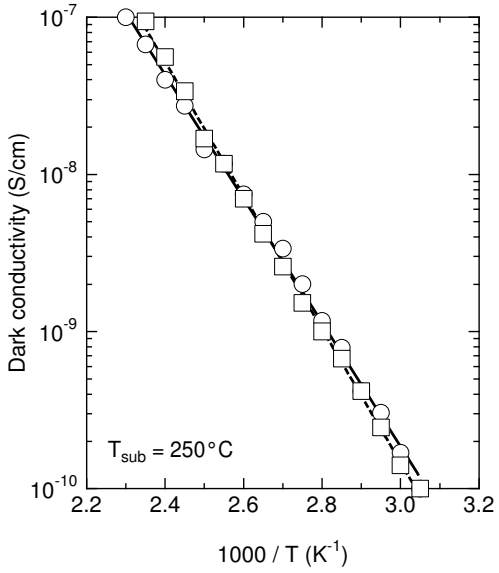

Fig. 2.5: An example of dark conductivity for an undoped a-Si:H film as a function of reciprocal temperature. The film has been prepared at substrate temperature of 250°C.

mined from the Tauc's plot [18] of optical absorption coefficients of the films. The activation energy is in the range of 0.75–0.85 eV for $T_{\rm sub}$ of 200–300°C. Activation energy corresponds to the energy from Fermi level to conduction band edge (or mobility edge) [17]. On the other hand, the optical energy gap of the films is in the range of 1.60–1.65 eV, which is close to twice of the activation energy. This indicates that the Fermi level of the films is close to the middle of energy gap, and means that ideal intrinsic undoped a-Si:H films can be prepared with the VUV photo-CVD method using Si_2H_6 and 147-nm excitation. This nature is also confirmed from the fact that the films have fairly low conductivity of 10^{-11} S/cm as described in the next section.

2.3.2 Photoelectric properties

Figure 2.7 shows the photo- and dark conductivity of the undoped films. The photoconductivity is measured under air mass one (AM1) (100 mW/cm^2) illumination. The dark conductivity is as low as 10^{-11} S/cm and the photoconductivity is as high as 10^{-5} S/cm. Both of the photo- and dark conductivity do not show any explicit dependence on $T_{\rm sub}$ in the range of 200–400°C. The high photoconductivity of 10^{-5} S/cm suggests that the films have a low density of defects which capture photo-generated carriers [19].

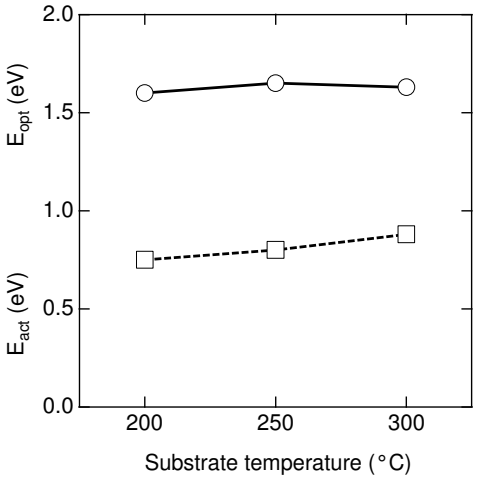

Fig. 2.6: Optical energy gap E_{opt} obtained from optical absorption measurements, and activation energy E_{act} obtained from temperature dependence of dark conductivity.

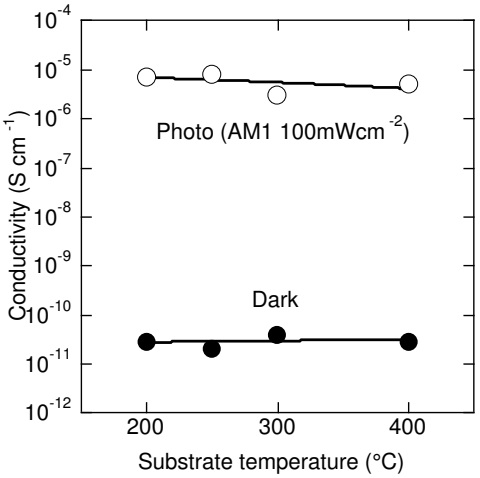

Fig. 2.7: Conductivity of the undoped films under dark and during illumination by AM1 light at 100 mW/cm^2.

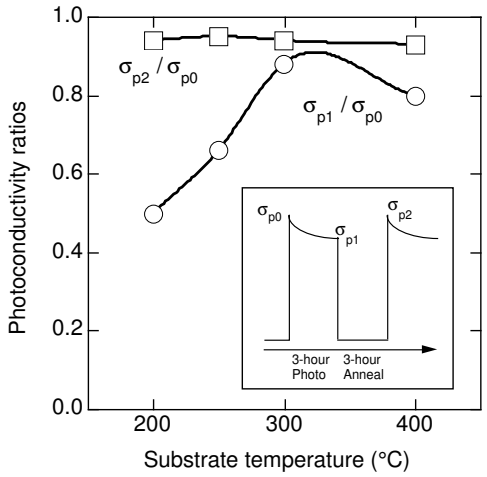

Fig. 2.8: Change of photoconductivity after illumination (AM1, 100 mW/cm^2) and after annealing at 230°C for 3 hours.

Although high photoconductivity of a-Si:H is useful for photovoltaic applications, it is known to be degraded by long-term illumination and to be recovered by heating (annealing) for several hours. This phenomenon is known as Steabler-Wronski (S-W) effect [20]. In order to investigate the S-W effect, light-soaking has been examined on the deposited films. Figure 2.8 shows the ratios σ_{p1}/σ_{p0} and σ_{p2}/σ_{p0}, where the symbols σ_{p0} and σ_{p1} are the initial photoconductivity under AM1 (100 mW/cm^2) and the final photoconductivity after 3-hour illumination, respectively. The symbol σ_{p2} is the photoconductivity of the films annealed at 230°C for 3 hours after the illumination.

The ratio σ_{p1}/σ_{p0} indicates the durability of the photoconductivity under the illumination. The durability depends on substrate temperature, whereas the initial photoconductivity does not depend on it. The ratio σ_{p1}/σ_{p0} is higher than 0.5 and reaches 0.9 for T_{sub} of 300°C. The degraded photoconductivity recovers up to 0.95 of the initial one by the annealing. The high durability of $\sigma_{p1}/\sigma_{p0} = 0.9$ against the illumination is promising for solar cell applications.

2.3.3 Hydrogen bonding configuration

Hydrogen atoms incorporated in a-Si:H films are known to exist in the form of Si-H, Si-H_2, Si-H_3 and (Si-H_2)$_n$ [21]. These bonds have specific IR absorption bands corresponding to their vibration modes such as stretching, bending and wagging modes. Example of an IR absorption spectrum of the photo-CVD

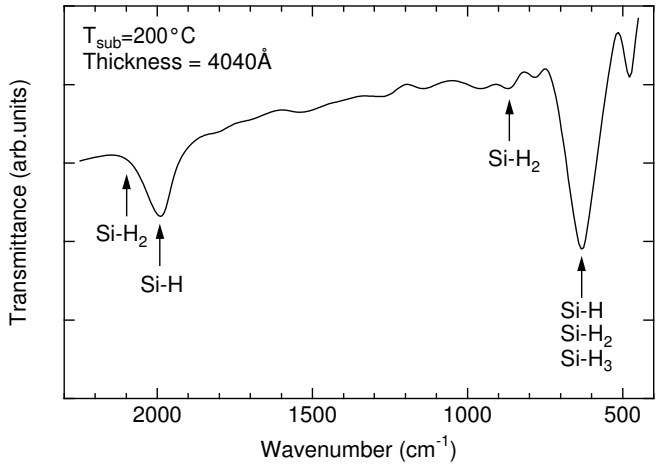

Fig. 2.9: Example of an infrared transmittance spectrum for the undoped film deposited by using the VUV photo-CVD method at substrate temperature of 200°C.

film is shown in Fig.2.9. The peaks for stretching mode of Si-H, Si-H_2 and Si-H_3 bonds are known to appear at separated wavenumber of 2000, 2090 and 2140 cm^{-1}, respectively, while those of bending and waging modes appear at almost the same wavenumber [22, 23]. Therefore, one can investigate hydrogen incorporation scheme from an IR absorption spectrum around 2000 cm^{-1}, although the peak at 2090 cm^{-1} is claimed to appear due to incorporation of Si-H bonds in voids [25] and Si-HX [26] (where X is contamination such as oxygen, nitrogen, halogen or carbon).

Fig.2.10 shows infrared absorption coefficient around 2000 cm^{-1} for the photo-CVD films. The spectra mainly consist of the component centered at 2000 cm^{-1} for Si-H stretching mode. The component at 2090 cm^{-1} is much smaller than the component at 2000 cm^{-1}. High photoconductivity duration of the photo-CVD films is regarded as a result of the small intensity of 2090 cm^{-1} component, because the photoconductivity duration is known to be improved by reducing density of Si-H_2 bonds and/or contamination [27, 28].

2.3.4 Hydrogen concentration

For the purpose of quantitative analysis, Si-H bond density N(Si-H) in the films has been deduced from integrated IR absorption coefficients around 2000 cm^{-1}, which is calculated by using following equation;

$$N(\text{Si-H}) = A \int \frac{\alpha(\omega)}{\omega} \mathrm{d}\omega, \tag{2.1}$$

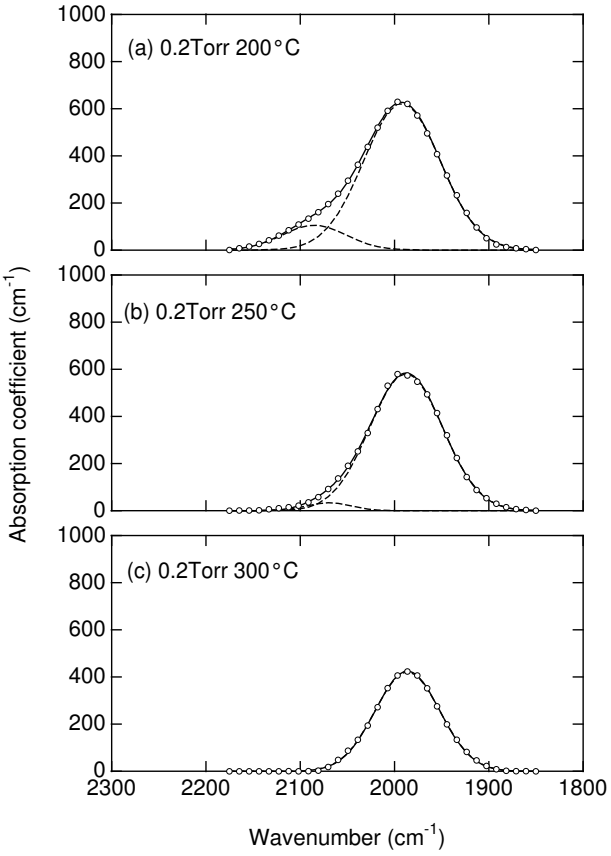

Fig. 2.10: IR absorption coefficients around 2000 cm^{-1} for the undoped films deposited by using the VUV photo-CVD methods at substrate temperatures ranging from 200 to 300°C.

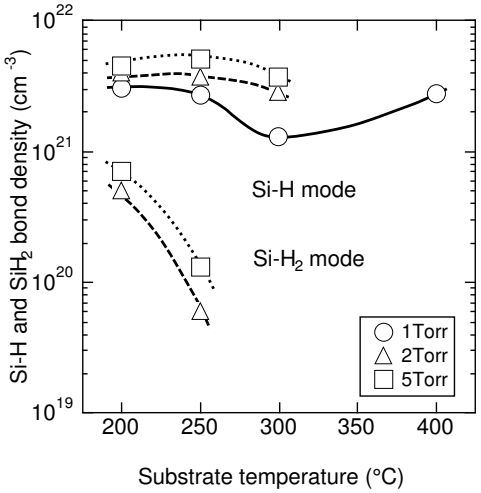

Fig. 2.11: Number density of Si-H_n bonds in the photo-CVD films measured as a function of substrate temperature.

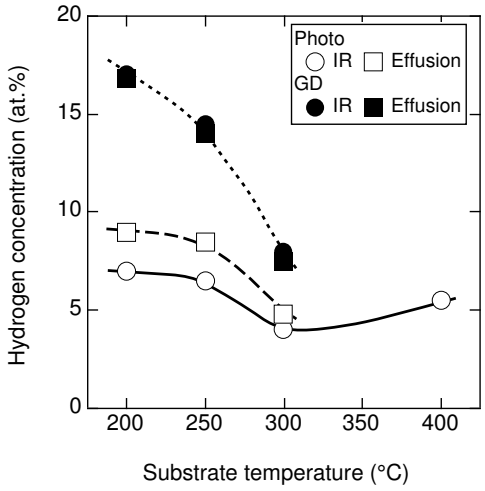

Fig. 2.12: Total hydrogen concentration obtained from IR absorption spectra and hydrogen effusion experiments.

where $\alpha(\omega)$ is absorption coefficient at wavenumber ω. Value of the proportionality constant A is reported to be 1.4×10^{20} cm^{-2} [15]. Deconvoluting the peak around 2000 cm^{-1} into two components of 2000 and 2090 cm^{-1}, N(Si-H) and N(Si-H_2) can be deduced separately, in which the proportionality constant for Si-H_2 bonds becomes a half of the value of A.

Fig.2.11 shows deduced density of Si-H and Si-H_2 bonds in the deposited films. Total hydrogen concentration C_H might not be equal to N(Si-H)+2N(Si-H_2) due to the ambiguity in the assignment for 2090 cm^{-1}. Therefore, a hydrogen effusion experiment has been performed as a direct method for determination of hydrogen concentration [16]. Fig.2.12 shows obtained C_H normalized to atomic % using the atomic density of crystalline Si (5×10^{22} cm^{-3}). For comparison, C_H for the films deposited by using a PE-CVD method and SiH_4 as a source gas is also shown in the same figure. As can be understood from Fig.2.12, similar tendency has been obtained for both determination methods.

As in these figures, the hydrogen concentration in the photo-CVD films decreases from 9 to 5 at.% with increasing T_{sub} from 200 to 300°C. For T_{sub} higher than 400°C, the concentration of Si-H is kept at around 5 at.%. These values are fairly low in comparison to the value for the PE-CVD films. From the results of Si-H and total hydrogen concentration measurements, the photo-CVD films are found to have a small amount of hydrogen. Recently it is suggested that the hydrogen concentration has a tendency to become low as deposition rate decreases [29, 30]. Although the low deposition rate of 0.6

nm/min for the photo-CVD may be a cause of the low hydrogen concentration, the hydrogen concentration in the films deposited using a Xe resonance lamp is lower by 5 at.% than that using a D_2 lamp (161 nm) even for almost the same deposition rate of 1.25 and 1.40 nm/min, respectively [14]. From this results, the low hydrogen concentration is related with natures of precursors produced by high-energy excitation and/or by photolysis of Si_2H_6 molecules with the Xe resonance lamp. In fact, the photon energy (8.4 eV) of the Xe resonance lamp is higher than energies to excite Si_2H_6 to some low-lying states 1^1A_{2u} (transition energy; 7.95 eV) and 1^1E_u (transition energy; 8.39 eV) [9], while the photon energy (7.7 eV) of the D_2 lamp is lower than these transition energies. This also suggests that the precursors produced with different excitation energy have different natures and different effects on a growing film.

One might be afraid that the suppression of the hydrogen concentration causes the increase of dangling bonds. High photo- and dark conductivity ratio, however, shows that the dangling bonds are kept at a low density in spite of the low hydrogen concentration in the films. Below-gap absorption measurements have actually revealed that the dangling-bond density is rather decreased. Details are described in the following section.

2.3.5 Defect-state density

Below-gap ($h\nu$<1.8 eV, the region B and C) absorption coefficients are measured using a constant photocurrent method (CPM) [31] in a dc mode and merged to the absorption coefficients (the region A) determined by transmission and reflection measurements [32] in the range of $h\nu$>1.8 eV. The results are given in Fig.2.13. The closed symbols in the figure represent experimental points from the CPM measurements, and the open symbols are those from the optical transmission and reflection measurements of the films.

The exponential absorption tail (the region B of straight line in the range of 1.4–1.8 eV) corresponds to the transition from localized states in the valence-band tail to extended states in the conduction band. The absorption is expressed as follows,

$$\alpha(h\nu) = \alpha_0 \exp\left(\frac{h\nu}{E_u}\right). \tag{2.2}$$

where E_u is the reciprocal gradient of the straight line, namely Urbach energy. The Urbach energy indicates the spread of the exponential band tail of the valence band, and the tail is led by structural disorder [33]. The value of

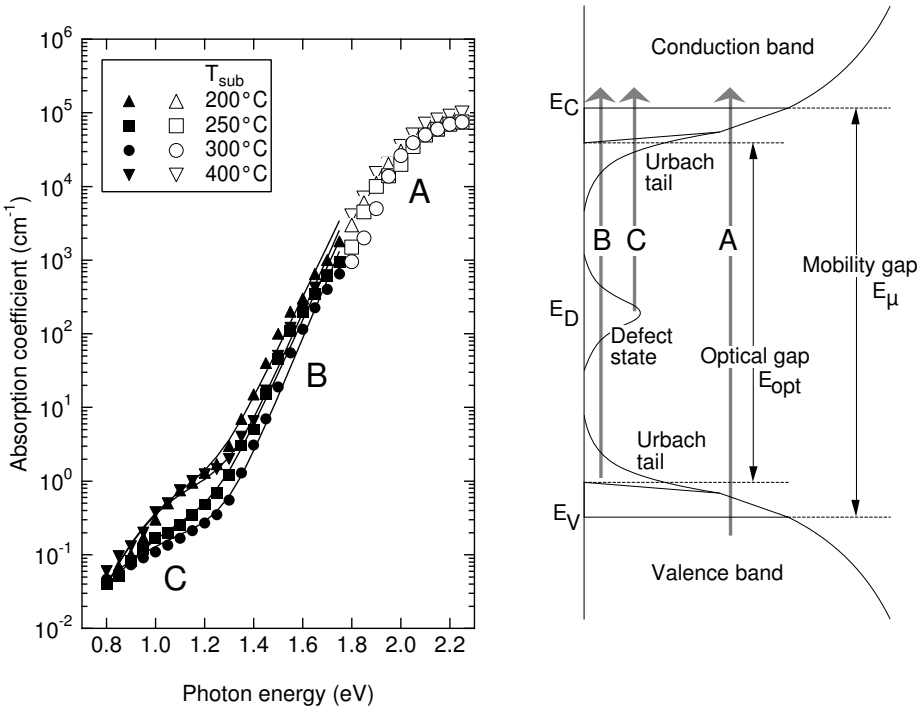

(a) Absorption coefficient (b) Transition schemes

Fig. 2.13: (a) Below-gap optical absorption coefficients versus photon energy for a-Si:H films deposited at substrate temperature ranging 200–400°C. Open symbols and closed ones are data measured using transmission/reflection and constant photocurrent methods, respectively. Solid lines are fitted results. (b) Schematic of photo-excited transition of electrons in a amorphous semiconductor. The transition schemes A, B and C correspond to the absorption regions A, B and C in the figure (a), respectively.

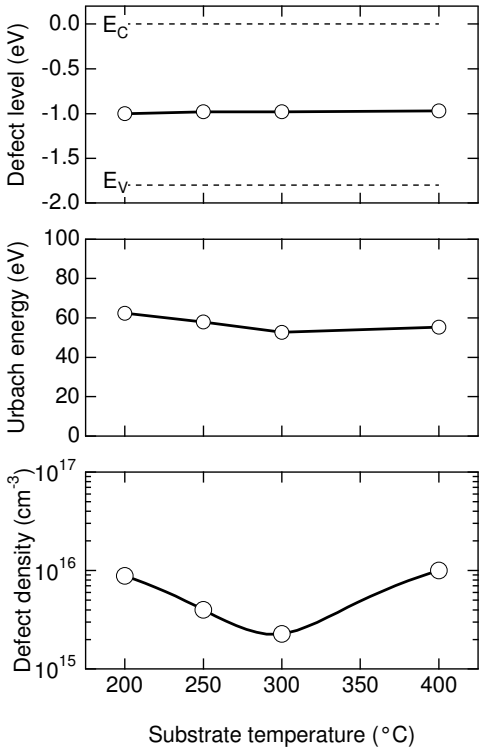

Fig. 2.14: (a) Energy level of the defect states, (b) Urbach energy and (c) defect density deduced from the data of constant photocurrent measurements for a-Si:H films deposited at substrate temperature of 200–400°C.

$E_{\rm u}$ obtained is shown in Fig.2.14 which decreases from 60 to 52 meV as $T_{\rm sub}$ increases from 200 to 300°C. This result shows that the structural disorder is reduced as $T_{\rm sub}$ increases from 200 to 300°C. For $T_{\rm sub}$ higher than 400°C, $E_{\rm u}$ increases to 56.4 meV, which is suspected to be due to the inclusion of contamination described later.

The shoulder (the region C) of the absorption coefficient below 1.4 eV corresponds to the transition from the defect states in the mid gap to the extended states in the conduction band. The defect-state density is obtained by fitting the measured absorption coefficients and calculated ones [31], in which the defect-state density $N_{\rm G}(\epsilon)$ in the mid-gap is supposed to have a broad Gaussian shape characterized by center level E_1 below the conduction-band edge, dispersion W and height $N_{\rm G}(-E_1) = (2\pi)^{-1/2}(A/W)$, namely,

$$N_{\rm G}(\epsilon) = \frac{A}{(2\pi)^{1/2}W} \exp\left[-\frac{(\epsilon + E_1)^2}{2W^2}\right]. \tag{2.3}$$

The density of the extended states in the conduction band is supposed to have a parabolic shape corresponding to a free electron as follows [34],

$$g_{\rm C}(\epsilon) = 6.7 \times 10^{21} \times \epsilon^{1/2} \quad (\epsilon > 0). \tag{2.4}$$

In eqs.(2.3) and (2.4), ϵ is an energy separation measured from the conduction-band edge, i.e. $\epsilon = E - E_{\rm C}$. The optical absorption is calculated as follows [35],

$$\alpha(h\nu) = \frac{C}{h\nu} \times \int N_{\rm G}(\epsilon - h\nu) g_{\rm C}(\epsilon) d\epsilon, \tag{2.5}$$

where the constant C is corresponding to the transition matrix element. The value of $C = 3.8 \times 10^{-38}$ cm^{5}eV^2 has been obtained from $\alpha = 1.5 \times 10^5$ cm^{-1} at $h\nu = 2.5$ eV for the photo-CVD films which have $E_{\rm opt} = 1.75$ eV. The integration of eq.(2.3) has been carried out from 0 to 2.5 eV as a reasonable limit, because the integration over 2.5 eV made no significant changes on the results. The fitting parameters A, W and E_1 are determined almost uniquely, because the effects of changing parameters A, W, E_1 on the shoulder of absorption coefficients are independent as follows: a parallel shift of the shoulder, a change of the shoulder curvature and a vertical shift of the shoulder, respectively.

The fitted results are shown in Fig.2.13 by solid lines. The defect-state density A shown in Fig.2.14 decreases from 9.0×10^{15} to 2.2×10^{15} cm^{-3} as $T_{\rm sub}$ increases from 200 to 300°C, but it increases to 1.0×10^{16} cm^{-3} as $T_{\rm sub}$ increases to 400°C. The lowest defect-state density of the photo-CVD films is comparable or low compared with that of films prepared by advanced techniques [39, 40]. The average value of E_1 is 1.0 eV which agrees with the energy level of dangling bonds suggested by other workers [31, 41]. From these results, it is concluded that the dangling-bond density in the photo-CVD films is kept low in spite of the small amount of hydrogen in the films.

With the change in the defect-state density caused by increasing $T_{\rm sub}$, the degradation of photo-conductivity after AM1 (100 mW/cm^2) 3-hour illumination decreases from 50 to 10% for $T_{\rm sub}$ of 200–300°C and increases to 20% for $T_{\rm sub} = 400$°C. Initial dark conductivity and photo- to dark conductivity ratio, however, are not so much altered and kept at the excellent value of $\sim 10^{-11}$ S/cm and 10^5–10^6, respectively. These results mean that, within the deposition conditions studied in this work, the change in the defect-state density in the range 10^{15}–10^{16} cm^{-3} correlates with the change of the photoconductivity degradation, but it does not correlate with the initial dark and photoconductivity.

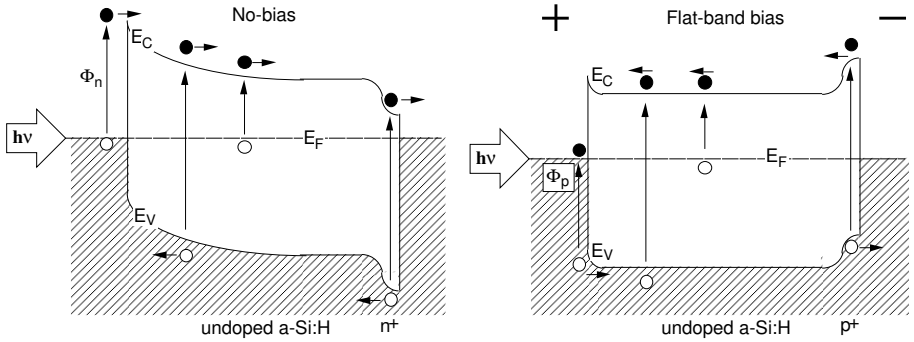

Fig. 2.15: Schematic band diagram for internal photo emission spectroscopy for obtaining (a) Φ_n and (b) Φ_p, in which n^+ with no bias voltage and p^+ layer with bias voltage for preparing flat-band condition, respectively.

The defect-state density decreases with increasing T_{sub} in the range 200–300°C, but it increases for $T_{sub} = 400$°C. As a cause for the increase of the defect-state density, the contamination of impurities is suspected to arise on the growing film due to out-gas from chamber walls and substrate holder. Improvements of the chamber must be considered in case of high T_{sub} deposition even for the photo-CVD method.

2.3.6 Mobility gap

Mobility gap is determined using an internal photoemission method [36]. Sample structures of semitransparent metal/i/p^+/ITO and semitransparent metal/i/n^+/ITO are used to determine the separations Φ_{Bp} and Φ_{Bn} of the valence- and conduction-band edges from the metal Fermi level. The intrinsic layer is deposited on the p^+- and n^+-layers to prepare the structure rejecting the flow of electrons and holes for the measurements, respectively, as shown in Fig.2.15. Ni and Al are used as semitransparent metal contacts on the i-layer. The energy separations Φ_{Bp} and Φ_{Bn} are determined from the photon energy dependence of photocurrent at room temperature using the Fowler's relation for photoemission as follows [37, 38];

$$Y(h\nu) \propto (h\nu - \Phi_B)^2, \tag{2.6}$$

where yield $Y(h\nu)$ is defined as photocurrent per incident photon, and Φ_B corresponds to Φ_{Bp} or Φ_{Bn}. The photon energy has been varied in the range 1.0–1.3 eV. The energy separations Φ_{Bp} and Φ_{Bn} are determined by extrapolation on $Y(h\nu)^{1/2}$ versus $h\nu$ plot. Mobility gap E_μ is obtained from the sum

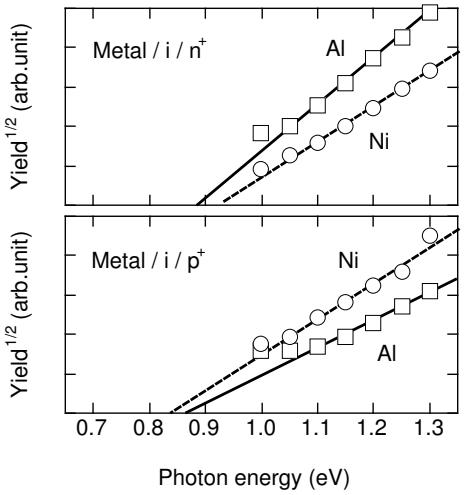

Fig. 2.16: Examples of $Y(h\nu)^{1/2}$ vs. $h\nu$ plot for the film deposited at 300°C. The points extrapolated onto the photon energy axis in (a) and (b) indicate Φ_{Bn} and Φ_{Bp}, respectively.

of Φ_{Bp} and Φ_{Bn}. Figs.2.16(a) and 2.16(b) show the examples of the plot to obtain Φ_{Bp} and Φ_{Bn} for the film deposited at $T_{\mathrm{sub}} = 300$°C.

The results obtained using Ni as the semitransparent metal contact are shown in Fig.2.17. The results for Al are consistent with the difference between the work functions of Ni (4.9 eV) and Al (4.3 eV) [42], because Φ_{Bp} for Ni is larger than that for Al, and Φ_{Bn} for Ni is smaller than that for Al. The sums of Φ_{Bp} and Φ_{Bn} i.e. E_μ obtained for Ni and Al almost agree with each other.

The difference between the mobility gap and the optical gap, i.e. $E_\mu - E_{\mathrm{opt}}$, is attributed to the energy width of the localized states at the edge of the conduction or the valence bands. For the films deposited at T_{sub} of 200–300°C, the photo-CVD films show a gap difference of $E_\mu(1.80) - E_{\mathrm{opt}}(1.75) = 0.05$ eV, while the PE-CVD films reported recently show $E_\mu(1.89) - E_{\mathrm{opt}}(1.73) = 0.16$ eV [36]. This result means that the energy width of the localized states near the band edges of the photo-CVD films deposited at T_{sub} of 200–300°C is narrower than those of conventional PE-CVD films. This undoped a-Si:H is useful as an i-layer in p-i-n solar cell structures, since the carriers in the i-layer may have a long life time because of the low localized-state density at band edges.

The correlation between E_μ and E_{u} which are both related with structural disorder and localization of electronic states, is not found in this study, since

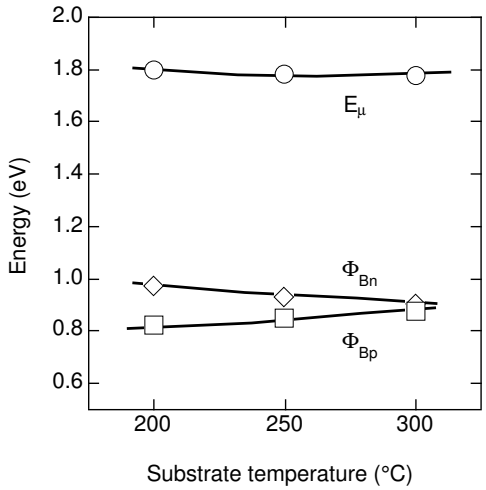

Fig. 2.17: Mobility gap determined by using an internal photoemission method on a-Si:H films deposited at substrate temperature of 200–300°C. The a-Si:H films have $E_{\rm opt} = 1.75$ eV.

E_μ does not show any explicit dependence on $T_{\rm sub}$ as in Fig.2.17, whereas $E_{\rm u}$ decreases with increasing $T_{\rm sub}$ in the range 200–300°C as in Fig.2.14.

2.4 Doping characteristics

As the films deposited with Si_2H_6 + 147 nm have shown excellent properties, substitutional doping for n- and p-type has also been examined for the purpose of revealing applicability to the photovoltaic devices such as solar cells, xerography, image sensors and so on. The substrate temperature has been kept at 250°C. Phosphine (PH_3) and diborane (B_2H_6) are used as dopant gases for n- and p-type doping, respectively.

2.4.1 Dark conductivity

Figures 2.18(a) shows dark conductivity as a function of dopant composition. The temperature dependence of the dark conductivity has shown a good linear relation in the Arrhenius plot for all samples in the range of 30–180°C. This indicates that activation-type conduction is dominant even in the doped films. Figure 2.18(b) shows the activation energy of the dark conductivity.

The dark conductivity reaches 4.0×10^{-3} S/cm and 1.5×10^{-3} S/cm at a dopant composition of 2% (PH_3/Si_2H_6) and 5%(B_2H_6/Si_2H_6), respectively.

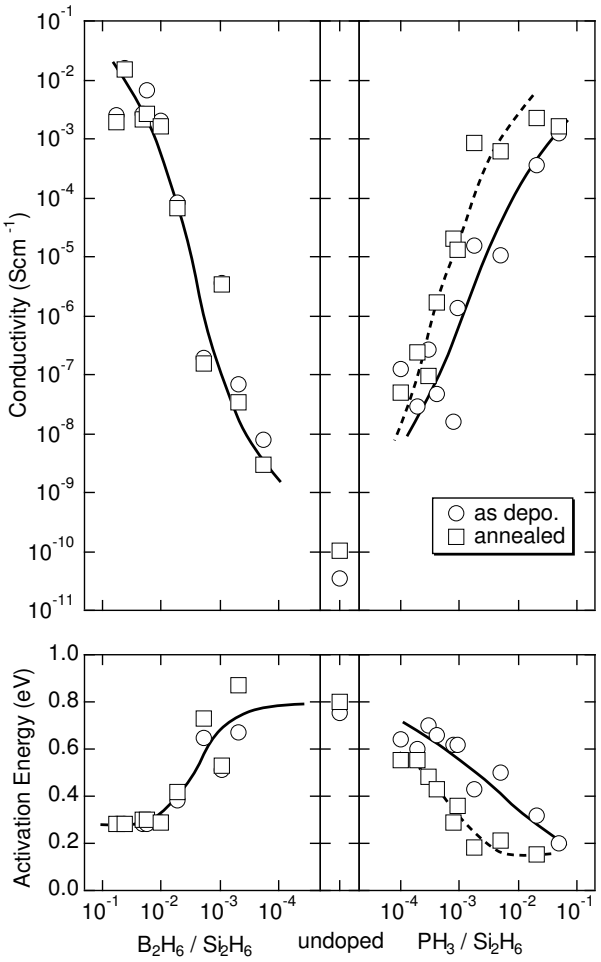

Fig. 2.18: Conductivity of the doped films as a function of dopant gas composition, and activation energy of the conductivity determined from its temperature dependence.

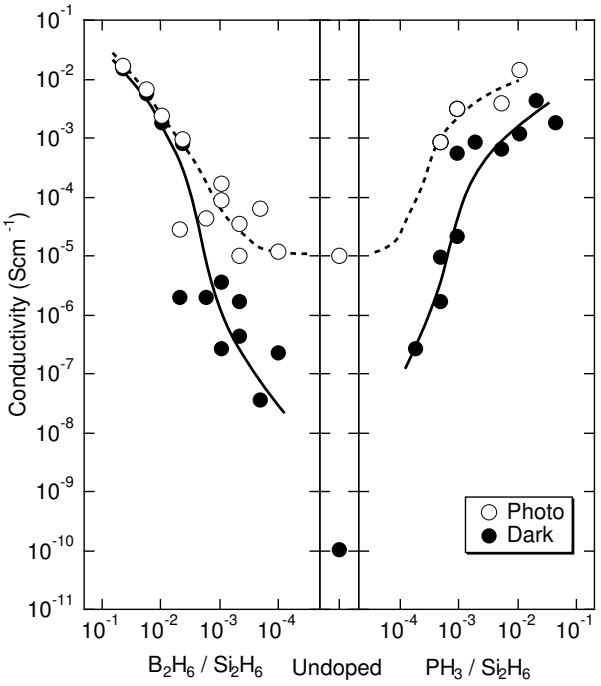

Fig. 2.19: Photo- and dark conductivity of phosphorus-doped, boron-doped and undoped films as a function of the activation energy of the dark conductivity. The films were deposited at T_{sub} of 250°C. The photoconductivity was measured under AM1 (100 mW/cm^2) illumination.

These values are about 10^8 of the dark conductivity of undoped films. The activation energy of the dark conductivity decreases with increasing doping composition. The minimum values are 0.17 eV and 0.21 eV for n- and p-type doping, respectively. From these results, it is concluded that both n- and p-type doping are achieved for a-Si:H deposited by using the VUV photo-CVD method.

For n-type doping, the dark conductivity is improved by a factor of 10 after annealing at 230°C for 3 hours as in Fig.2.18. This indicates phosphorus atoms in the as-deposited films is not activated sufficiently. The improvement in the conductivity is not observed for the p-type films.

2.4.2 Photoconductivity

Figure 2.19 shows photoconductivity (open symbols) of the films, in which dark conductivity (closed symbols) is also shown for comparison. Besides the change in the dark conductivity with the shift of Fermi level by substitutional

doping, there is a change in photoconductivity too. The photoconductivity has been measured under AM1 (100 mW/cm^2) illumination. There is a certain difference between the photoconductivity profiles for the boron-doped and phosphorus-doped films. The boron-doped films show constant photoconductivity, and the values are almost the same as that of undoped films. In contrast to the boron-doped films, the phosphorus doped films show the increase in the photoconductivity.

In order to clarify the cause of the increase in photoconductivity of phosphorus doped films, photoconductivity of the phosphorus doped films has been investigated in detail. For this purpose, light source for measuring photoconductivity has been changed to monochromatic light from a He-Ne laser ($h\nu$=1.96 eV) with known photon flux of 7.0×10^{14} cm^{-2} s^{-1}. Generally, the photoconductivity $\Delta\sigma$ is expressed as follows [19];

$$\Delta\sigma = e\eta\mu\tau\Phi(1-R)\{1-\exp(-\alpha d)\}/d, \tag{2.7}$$

where η is quantum yield, μ drift mobility, τ life time, Φ photon flux, R reflectivity, α absorption coefficient, and d thickness. There are three parameters R, α and $\eta\mu\tau$, which are expected to contribute to the increase of the photoconductivity. Other parameters are not affected by doping conditions. The reflectivity R was not so much altered by doping conditions. The absorption coefficients α of the phosphorus-doped films are less than that of the undoped films, which rather results in the decrease in photoconductivity and does not explain the increase in it. The product $\eta\mu\tau$ shows an increase by the two orders of magnitude with the phosphorus doping compared with that of the undoped film as shown in Fig.2.20. This increase in $\eta\mu\tau$ is regarded as the cause of the increase in the photoconductivity by the phosphorus doping. Anderson *et al.* explains that the life time τ is extended due to the filling of empty recombination centers with the shift of Fermi level toward the conduction-band side [43]. The photo-CVD films, however, show higher photoconductivity than PE-CVD films [44, 45] as shown in Fig.2.21.

This result suggests that the empty recombination centers are kept at low density. Thus, the defect density of the films has been investigated. Figure 2.22 shows the defect density of the phosphorus-doped films, which is estimated from below-gap absorption coefficients measured using a CPM. The defect density obtained is proportional to the squared root of the dopant-gas ratio. This results is consistent with a model of defect creation based on a mass-action law proposed by Street [46], which suggests that the same mechanism

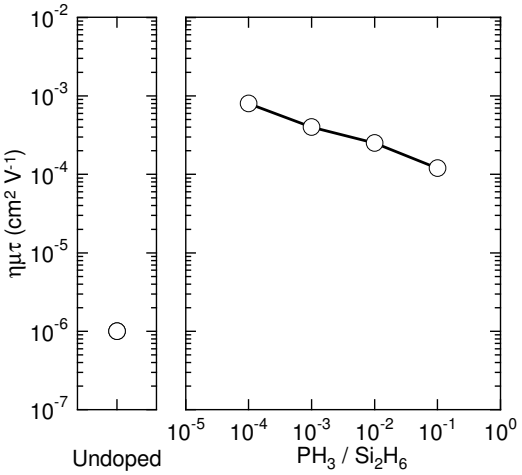

Fig. 2.20: The product $\eta\mu\tau$ of phosphorus-doped and undoped films for the illumination of a He-Ne laser ($h\nu$=1.96 eV, 7.0×10^{14} cm^{-2} s^{-1}).

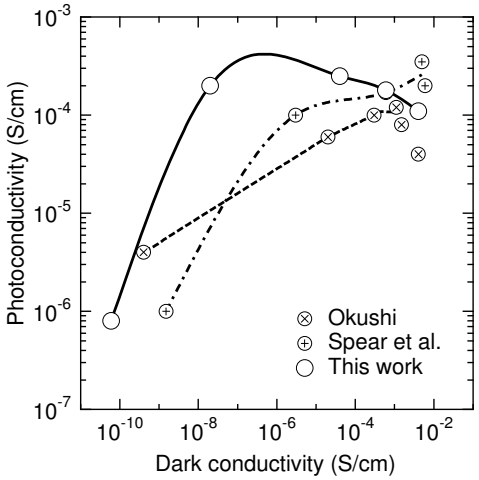

Fig. 2.21: Photoconductivity as a function of dark conductivity for phosphorus-doped and undoped films deposited at $T_{\rm sub}$ of 250°C. The photoconductivity was measured under the illumination of a He-Ne laser ($h\nu$=1.96 eV, 7.0×10^{14} cm^{-2} s^{-1}).

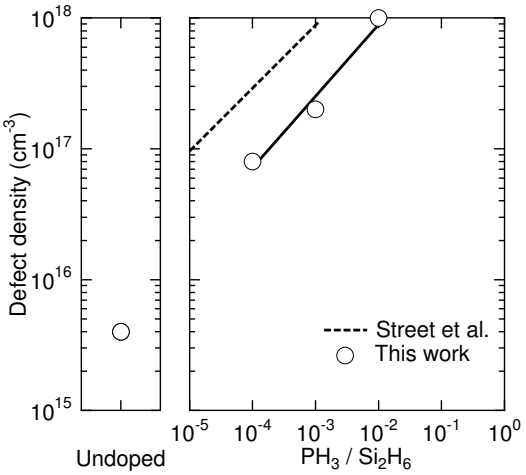

Fig. 2.22: Defect density of phosphorus-doped and undoped films estimated from below-gap absorption coefficients measured using a CPM.

works for the photo-CVD films. Although there is no drastic reduction in the defect density, the value is relatively low compared with that for PE-CVD films [47]. This low defect density is considered to be a cause of the increase in the photoconductivity, in addition to the filling of empty recombination centers by the shift of Fermi level.

2.4.3 Optical energy gap

In the case of opt-electric devices such as solar cells, the transparency of the films is important. In p/i/n structure for solar cells, p-type layer should transmit photons to the undoped i-layer for the generation of photo carriers. Therefore, $E_{\rm opt}$ of the doped films has been measured. Figure 2.23 shows $E_{\rm opt}$ as a function of dopant composition. As in the figure, phosphorus doped films have almost the same $E_{\rm opt}$ to undoped films. However, $E_{\rm opt}$ for boron doped films decreases when the doping composition exceeds 10^{-3}. The value of $E_{\rm opt}$ for PE-CVD films is shown in the same figure for comparison. As can be understood from the figure, optical properties of the films are almost the same to the PE-CVD films. In order to compensate the reduction in $E_{\rm opt}$, therefore, higher band-gap host materials such as a-SiC:H should be used for the preparation of the window layer as in PE-CVD methods.

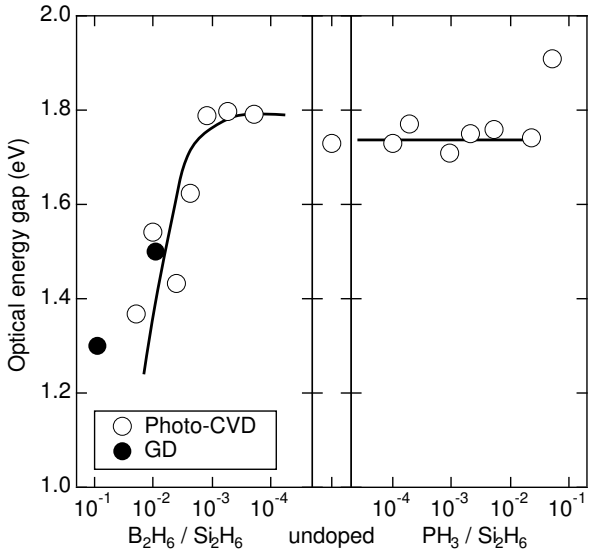

Fig. 2.23: Optical energy gap of doped films as a function of dopant composition.

2.5 Summary

In summary, a photo-CVD method using Si_2H_6 and VUV (147 nm) light has been revealed to be able to prepare a-Si:H films with excellent properties.

Undoped films show dark conductivity as low as 10^{-11} S/cm and photoconductivity as high as 10^{-5} S/cm under AM1 (100 mW/cm^2) illumination. These excellent properties do not depend on $T_{\rm sub}$ in the range of 200–400°C, and neither on the defect density of the films. The photoconductivity degradation after the 3-hour illumination and the defect density depend on $T_{\rm sub}$, and reach as low as 10 at.% and 2.2×10^{15} cm^{-3}, respectively, for $T_{\rm sub}$ of 300°C.

The hydrogen bonding configuration is mainly Si-H and the hydrogen concentration reaches as low as 5 at.%. In spite of the low hydrogen concentration, the photo-CVD films have low defect-state density of 2.2×10^{15} cm^{-3}, which suggests that the dangling-bond density is suppressed enough by a small amount of hydrogen. The mobility gap of the films is closer to the optical gap than that of PE-CVD films, which means that the energy width of localized states near the band edges is narrower than that of PE-CVD films.

Substitutional doping has also been successfully achieved by using PH_3 and B_2H_6 as dopant gases. Dark conductivity is controlled from 10^{-11} to 10^{-3} S/cm for both the phosphorus- and boron-doped films. Although optical energy gap decreases with increasing doping level concerning boron doped films as known for PE-CVD films, it can be compensated by using a-SiC:H as a host material.

Regarding the phosphorus-doped films, they show much higher photoconductivity than the dark conductivity in comparison to the boron-doped films. The increase in the photoconductivity is due to the increase of $\eta\mu\tau$, which is said to be due to the filling of empty recombination centers by the shift of Fermi level. The defect density of the phosphorus-doped films is relatively low compared with that of PE-CVD films, which may contribute to the additional increase in $\eta\mu\tau$ besides the increase by the shift of Fermi level.

References

[1] H. Niki and G. J. Mains: J. Phys. Chem. **68** (1964) 304.

[2] M. Kumagawa, H. Sunami, T. Terasaki and J. Nishizawa: Jpn. J. Appl. Phys. **7** (1968) 1332.

[3] T. Saitoh, S. Muramatsu, S. Matsubara and M. Migitaka: Jpn. J. appl. Phys. **22** Suppl. 22-1 (1982) 617.

[4] T. Saitoh, S. Muramatsu, T. Shimada and M. Migitaka: Appl. Phys. Lett. **42** (1983) 678.

[5] H. Ito, M. Hatanaka, K. Mizuguchi, K. Miyake and H. Abe: Proc. 4th Symp. Dry Process (The IEEJ, Tokyo, 1982) p.100.

[6] Y. Mishima, M. Hirose, Y. Osaka, K. Nagamine, Y. Ashida, N. Kitagawa and K. Isogaya: Jpn. J. Appl. Phys. **22** (1983) L46.

[7] T. Inoue, M. Konagai and K. Takahashi: Appl. Phys. Lett. **43** (1983) 774.

[8] U. Itoh, Y. Toyoshima, H. Konuki, N. Washida and N. Ibuki: J. Chem. Phys. **85** (4867) 1986.

[9] E. Kawai, K. Kasatani, M. Kawasaki, H. Sato and K. Hirao: Jpn. J. Appl. Phys. **28** (1989) 247.

[10] A. N. Zaidel and E. Y. Shreider: *Vacuum Ultraviolet Spectroscopy* (Ann-Arbor-Humphrey, Ann Arbor, 1970).

[11] K. Kumata, U. Itoh, Y. Toyoshima, N. Tanaka, H. Anzai and A. Matsuda: Appl. Phys. Lett. **48** (1986) 1380.

[12] A. Yamada, K. Konagai and K. Takahashi: Jpn. J. Appl. Phys. **24** (1985) 1586.

[13] K. Takahashi, H. Matsunami, Y. Murata and M. Hanabusa: *Hikarireiki Process no Kiso* (Kogyochosakai, Tokyo, 1994) pp.58–59.

[14] T. Fuyuki, K. -Y. Du, S. Okamoto, S. Yasuda, T. Kimoto, M. Yoshimoto and H. Matsunami: J. Appl. Phys. **64** (1988) 2380.

[15] C. J. Fang, L. Ley, H. R. Shanks, K. J. Gruntz and M. Cardona: Phys. Rev. B **22** (1980) 6140.

[16] H. Fritsche, M. Tanielian, C. C. Tsai and P. U. J. Gaczi: J. Appl. Phys. **50** (1979) 3366.

[17] H. Overhof and P. Thomas: *Electronic Transport in Hydrogenated Amorphous Semiconductors* (Springer-Verlag, Berlin, 1989) Chapter 2. Elementary Treatment of Transport in Amorphous Semiconductors.

[18] M. H. Cohen: J. Non-Cryst. Solids **4** (1970) 391.

[19] R. H. Bube: *Photoconductivity of Solids* (John Wiley & Sons, Inc., New York, 1960) Chapter 3. Photoconductivity Processes.

[20] D. L. Steabler and C. R. Wronski: Appl. Phys. Lett. **31** (1977) 292.

[21] M. H. Brodsky, M. Cardona and J. J. Cuomo: Phys. Rev. B **16** (1977) 3556.

[22] G. Lucovsky, R. J. Nemanich and J. C. Knights: Phys. Rev. B **19** (1979) 2064.

[23] H. Shanks, C. J. Fang, L. Ley, M. Cardona, F. J. Demond and S. Kalbitzer: Phys. Stat. Sol. (b) **100** (1980) 43.

[24] M. Cardona: Phys. Stat. Sol. (b) **118** (1983) 463.

[25] H. Wagner and W. Beyer: Solid State Commun. **48** (1983) 585.

[26] G. Lucovsky: Solid State Commun. **29** (1979) 571.

[27] N. Nakamura, T. Takahama, M. Isomura, M. Nishikuni, K. Yoshida, S. Tsuda, S. Nakano, M. Ohnishi and Y. Kuwano: Jpn. J. Appl. Phys. **28** (1989) 1762.

[28] Y. Kuwano and S. Tsuda: Proc. Int. Conf. on Stability of Amorphous Silicon Alloy Materials and Devices, California, U.S.A., 1987, AIP Conf. Proc. **157** (1987) 378.

[29] Y. Hishikawa, M. Ohnishi and Y. Kuwano: Amorphous Silicon Technol. 1990, San Francisco U.S.A., 1990, Mater. Res. Soc. Symp. Proc. **192** (1990) 3.

[30] J. Perrin, I. Solomon, B. Bourdon, J. Fontenille and E. Ligeon: Thin Solid Films **62** (1979) 327.

[31] M. Vaněček, J. Kočka, J. Stuchlík, Z. Kožíšek, O. Štika and A. Tříska: Sol. Energy Mater. **8** (1983) 411.

[32] S. G. Tomlin: Brit. J. Appl. Phys. (J. Phys. D Ser.2) **1** (1968) 1667.

[33] M. H. Cohen, M. Y. Chou, E. N. Economou, S. John and C. M. Soukoulis: IBM J. Res. Develop. **32** (1988) 82.

[34] G. A. N. Connell: *Topics in Applied Physics 36, Amorphous Semiconductors* Ed. M. H. Brodscky (Springer-Verlag, Berlin 1979) p.98.

[35] J. Tauc: *Amorphous and Liquid Semiconductors* Ed. J. Tauc (Plenum Press, London, 1974) p.159.

[36] C. R. Wronski, S. Lee, M. Hicks and S. Kumar: Phys. Rev. Lett. **63** (1989) 1420.

[37] E. H. Rhoderick and R. H. Williams: *Metal-Semiconductor Contacts* (Clarendon Press, Oxford, 1978)

[38] R. J. Nemanich and M. J. Thompson: *Metal-Semiconductor Schottky Barrier Junctions and Their Applications* Ed. B. L. Scharma (Plenum Press, New York, 1984) p.335.

[39] K. Shepard, Z. E. Smith, S. Aljishi and S. Wagner: Amorphous Silicon Technol. 1988, Nevada, U.S.A, 1988, Mater. Res. Soc. Symp. Proc. **118** (1988) 147.

[40] H. Curtins, M. Favre, Y. Ziegler, N. Wyrsch and A. V. Shah, Amorphous Silicon Technol. 1988, U. S. A., 1988, Mater. Res. Soc. Symp. Proc. **118** (1988) 159.

[41] T. Shimizu, X. Xu, H. Kidoh, A. Morimoto and M. Kumeda: J. Appl. Phys. **64** (1988) 5034.

[42] A. M. Cowley and S. M. Sze: J. Appl. Phys. **36** (1965) 3212.

[43] D. A. Anderson and W. E. Spear: Philos. Mag. **36** (1977) 695.

[44] W. E. Spear and P. G. Le Comber: Phlos. Mag. **33** (1976) 935.

[45] H. Okushi: Philos. Mag. **33** (1985) 33. (Photon flux in this reference is 9.5×10^{14} cm^{-2} s^{-1})

[46] R. A. Street: Phys. Rev. Lett. **49** (1982) 1187.

[47] R. A. Street, D. K. Biegelsen, W. B. Jackson, N. M. Johnson and M. Stutzmann: Philos. Mag. **52** (1985) 235.

Chapter 3

Reaction kinetics in photochemical vapor deposition of a-Si:H

3.1 Introduction

a-Si:H films are mostly deposited with chemical vapor deposition methods, in which the films are generated from source gases through many chemical reactions and physical processes. In order to understand the CVD process, therefore, we must obtain the information concerning the reactions and processes. Only the information we can obtain, however, is the density of chemical species as an accumulated results of these reactions and processes. Proposed reactions themselves are mostly always speculative. The knowledge of the density is important for determining dominant deposition precursor, but is not enough for controlling the CVD process. In order to control the CVD process, we must clarify which chemical reaction or physical process is dominant for realizing the density of a given chemical species at measured density. Rate constant of a reaction is one index for predicting its contribution in whole reactions. However, reaction rate is determined not only by the rate constant but also the density of reactants which are determined by the other reactions. Therefore, we cannot predict the steady state because of these complex reaction loops. Only the way to predict the results is a numerical simulation technique.

The numerical simulation of plasma enhanced CVD (PE-CVD) systems is difficult to handle because it contains not only chemical reactions between neutral species but also those between charged particles such as electrons and ions which are affected by electric field. On the contrary, photo-CVD systems are rather easy to handle, because they are explained only by the kinetics of neutral radicals. The first attempt for simulation of photo-CVD was made by Perrin *et al.* [1], and they predicted that dominant species is SiH_3 in mercury

sensitized photo-CVD system using SiH_4. More sophisticated simulation on the same system was carried out by Matsui *et al.* [2]. Their gas-phase simulation results successfully explained time-dependence of the density of stable molecules such as SiH_4, H_2, Si_2H_6 and Si_3H_8, However, they did not treated surface reactions of radicals as they can predict film properties, and reported on only one combination of source gas and excitation method.

In this chapter, therefore, a simulation method similar to Matsui *et al.* has been applied to the photo-CVD system using Si_2H_6 and 147 nm, in which deposited films showed excellent properties. In addition, the other combinations of SiH_4 + 147 nm and Si_2H_6 + 185 nm are also investigated for comparison both experimentally and theoretically, and difference in the properties of the films deposited with different combinations of source gases and excitation wavelengths is explained in terms of difference in the composition of radical flux. In addition, hydrogen concentration and its bonding configuration are discussed by means of modeling surface reactions.

3.2 Experiments

3.2.1 Film deposition

Wavelengths used in this chapter are 185 and 147 nm. These are emitted from a disk-shaped vacuum ultraviolet light source using microwave (2.45 GHz) discharge in Hg and Xe, respectively, at an input-microwave power of 100 W. Pulsed operation is utilized for the purpose of increasing emission intensity [3], of which pulse width of 5 μs and frequency of 20 KHz is used as the optimized condition. Figure 3.1 shows schematic representation of experimental setup. Microwave power is fed through a tapered waveguide into dielectric material, 100 mm diameter and 4 mm thick, which works as a window of the light source with an effective aperture of 80 mm. With the microwave electric field perpendicular to the propagating direction and the window surface, the discharge is sustained in a disk-shaped volume filled with discharge gases. In the case of 147 nm emission, 1% Xe/He is used under pressure of 1 Torr, and gas flow of 10 sccm is necessary to prevent an intensity decrease caused by outgassing impurities. Sapphire is used as a window material because, at 1mm thickness, it transmits up to 20% of the 147 nm emission, and withstands the atmospheric pressure difference at the large diameter of 80 mm. In the case of 185 nm emission, 20 mg Hg filled in quartz capsule with Ar at the pressure

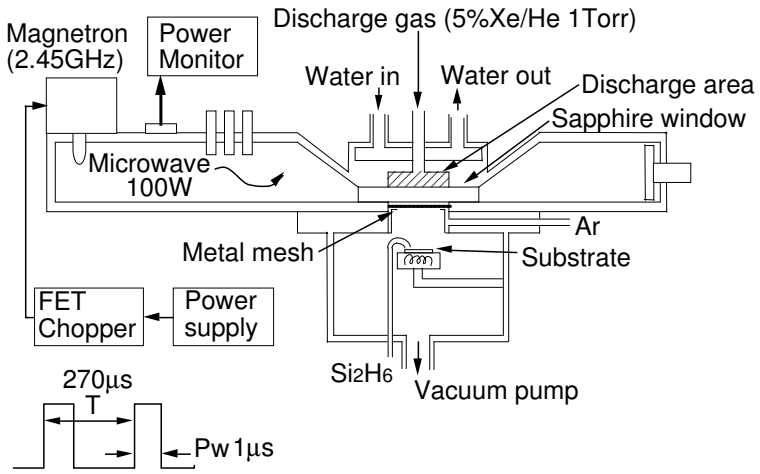

Fig. 3.1: Schematic representation of the photo-CVD system used in this chapter. The upper part is VUV light source driven by pulsed microwave. The lower part is deposition chamber. These are separated with a sapphire window (5 mm thick, 80 mm diameter).

of 0.1 Torr. Bottom side of the capsule becomes window for transmitting 185 nm emission in this case.

Source gases used in this work are SiH_4 and Si_2H_6. Possible combination of the wavelengths and source gases are Si_2H_6 + 147 nm, Si_2H_6 + 185nm and SiH_4 + 147nm for the deposition of a-Si:H. Flow rates of SiH_4 and Si_2H_6 are both 10 sccm. The distance between the substrate and the window of the light source is 5 cm. To prevent the deposition on the window, it is blown with Ar at a flow rate of 100 sccm. Total pressure is kept at 1 Torr unless otherwise noted.

3.2.2 Deposition rate

Figure 3.2 shows the measured deposition rate as a function of source-gas partial pressure with different combinations of excitation wavelengths and source gases. The partial pressure is controlled by changing the total pressure by adjusting pumping rate. The highest deposition rate of 4.6 nm/min is obtained with the combination of Si_2H_6 + 147 nm. The deposition rate is close to the typical rate of 6 nm/min for obtaining device quality films by a PE-CVD method [4].

For the combination of Si_2H_6 + 147nm, deposition rate decreases with increase in the partial pressure of Si_2H_6. This is due to the decrease in light

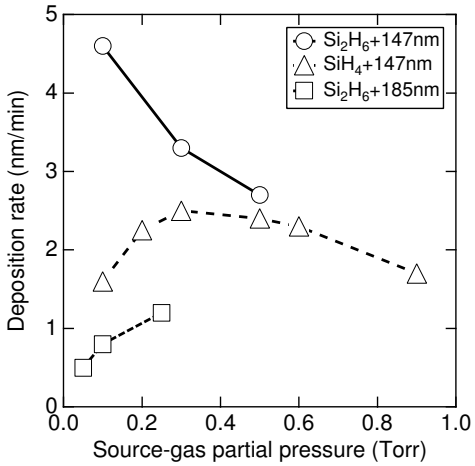

Fig. 3.2: Deposition rate as a function of source-gas partial pressure for different combination of excitation wavelengths and source gases.

intensity near the substrate surface, which is caused by the large attenuation due to the higher absorption cross section of Si_2H_6 at that wavelength [5]. For the combinations of Si_2H_6 + 185 nm and SiH_4 + 147 nm, deposition rate increases with the pressure in the region of low partial pressure. These results indicate that the source-gas density is not sufficient to attenuate the number of incident photons. On the other hand, deposition rate decreases in the region of high partial pressure as in the case of Si_2H_6 + 147 nm. From these results, it is found that there is an optimal source-gas partial pressure for obtaining the highest deposition rate for each combination of the source gas and the excitation wavelength.

3.2.3 Hydrogen incorporation scheme

Figure 3.3 and 3.4 show the hydrogen concentration C_H in atomic % (at.%) and the ratio $N(\text{Si-H}_2)/N(\text{Si-H})$, respectively, where $N(\text{Si-H})$ and $N(\text{Si-H}_2)$ are density of mono- (Si-H) and di-hydride (Si-H_2) bonds, respectively. These densities are calculated from integrated infrared absorption coefficients around 2000 and 2090 cm^{-1} [6], respectively, although there are ambiguities due to the possibility that the Si-H cluster may also contribute to the 2090 cm^{-1} band [7].

The dependence of C_H on the substrate temperature (T_{sub}) for each combination shows a similar tendency, that is, C_H decreases with increasing T_{sub}. This results is similar to the results reported for PE-CVD, and explained by the desorption of hydrogen from the growing film surface [8]. If we compare

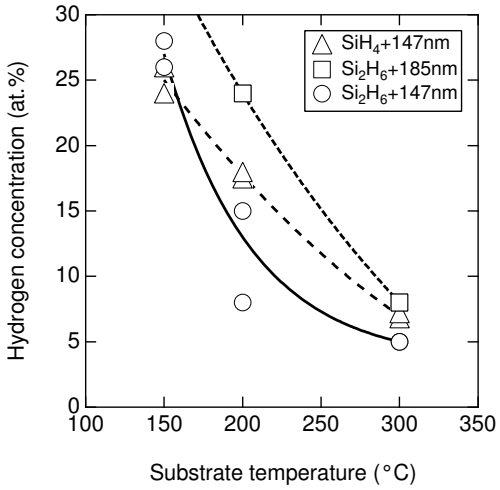

Fig. 3.3: Hydrogen concentration C_{H} in the films deposited with different combinations of excitation wavelengths and source gases.

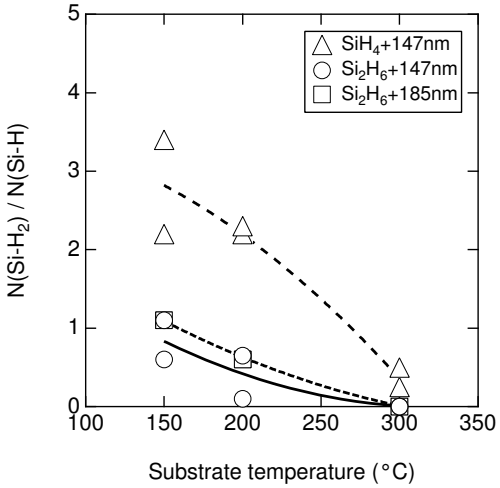

Fig. 3.4: Ratio of $N(\mathrm{Si\text{-}H_2})/N(\mathrm{Si\text{-}H})$ for the films deposited with different combinations of excitation wavelengths and source gases, where $N(\mathrm{Si\text{-}H})$ and $N(\mathrm{Si\text{-}H_2})$ are density of Si-H and Si-H_2 bonds in the films respectively.

C_H at the same T_{sub}, films deposited with Si_2H_6 + 147 nm show relatively lower values. The difference in C_H at the same T_{sub} suggests that there are other factors determining C_H in addition to T_{sub}. C_H is known to decrease with decreasing deposition rate [9]. However, this mechanism does not explain the experimental results that the films deposited with Si_2H_6 + 147 nm show lower C_H than those with the other combinations, since the deposition rate for Si_2H_6 + 147 nm is somewhat higher than those for the other combinations. Therefore, the difference in C_H should be attributed to the difference in components of impinging radical species, in addition to the difference in the total flux density corresponding to the deposition rate.

As can be seen in Fig.3.4, the difference in $N(\text{Si-H}_2)/N(\text{Si-H})$ is more marked than that in C_H. The hydrogen bonding configuration of the films deposited with SiH_4 + 147 nm is mainly composed of Si-H_2 bonds. On the other hand, the configuration in the films deposited with Si_2H_6 + 147 nm and Si_2H_6 + 185 nm consists mainly of Si-H bonds. However, the hydrogen bonding configuration becomes mainly Si-H bonds for all cases as T_{sub} increases. This indicates that film structure for low T_{sub} is controlled by the kind of impinging radical and its adsorption process. At higher T_{sub}, the process after adsorption of radicals, such as cross-linking between surface sites and buried sites, becomes dominant in controlling film structure, and effects of the difference in impinging radicals disappear.

If we compare the films deposited with Si_2H_6 + 147 nm and Si_2H_6 + 185 nm, the values of $N(\text{Si-H}_2)/N(\text{Si-H})$ for both cases are similar, although C_H shows a slight difference. Therefore, the structures of these films are considered to be similar. Similarity also appears in the defect-state density and the Urbach energy as described below. From these results, it is suggested that the same precursor impinges onto the growing surface in both cases.

3.2.4 Defect-state density

Figures 3.5 and 3.6 show the Urbach energy and the defect-state density, respectively. These are determined from below-gap absorption coefficients measured using a constant photocurrent method [10]. The Urbach energy indicates the spread of the exponential band tail at the valence-band edge, and the tail is attributed to the structural disorder. The defect-state density is correlated with the dangling bond density, although some slight differences are proposed to exist[11]. As can be seen in Figs.3.5 and 3.6, the films obtained

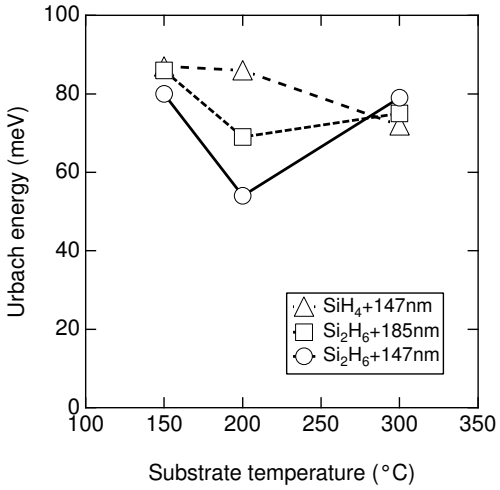

Fig. 3.5: Urbach energy of the films deposited with different combinations of excitation wavelengths and source gases.

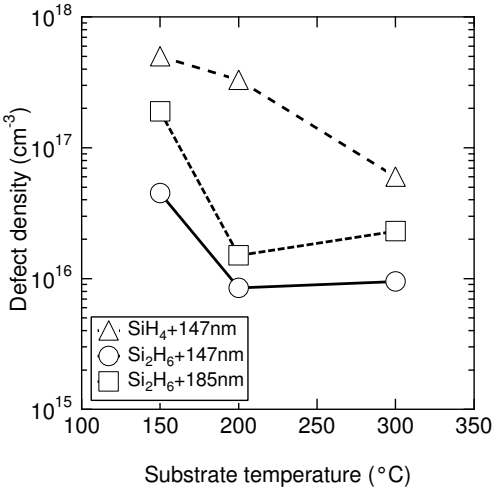

Fig. 3.6: Defect-state density of the films deposited with different combinations of excitation wavelengths and source gases.

with the combination of Si_2H_6 + 147 nm show the lowest Urbach energy and defect-state density in comparison to those obtained with the other combinations. This indicates that the structure of the films show less disorder and a smaller number of dangling bonds. Both the Urbach energy and the defect-state density decrease at first with increase in T_{sub}. This is explained in terms of a thermal annealing effect. However, they increase again passing through the minimum values at about 200°C. This is due to the fact that hydrogen desorption from the film becomes more frequent than the thermal annealing, and tends to leave dangling bonds [12]. Films deposited with Si_2H_6 + 185 nm also show a similar temperature dependence, which is probably due to the structural similarity estimated from C_H and $N(\text{Si-H}_2)/N(\text{Si-H})$.

Urbach energy and defect-state density in the films deposited with the combination of SiH_4 + 147 nm show the highest values in Figs.3.5 and 3.6, and their temperature dependence for this combination is different from those for the other combinations. This results may be due to the incorporation of Si-H_2 bonds at a much higher density, which possibly leads to structural disorders and vacancies in the films [13].

3.3 Gas-phase reaction simulation

As described in section 3.2, there is a difference in the structure of the films deposited under the three different conditions. That is, the hydrogen bonding configuration in the films deposited with the combination of SiH_4 + 147 nm is different from those with the other combinations. This must originate in the difference in radicals impinging onto the growing film surface. In order to discuss this difference, we have to take secondary reactions in the gas phase into account, because the pressure of our experiment is not low enough to allow us to ignore the secondary reactions. We estimate the number of main radicals arriving at the surface on the basis of a one-dimensional simulation of gas-phase reactions. The structure of deposited films is also discussed with the aid of a surface-reaction model using radical flux obtained by the gas-phase simulation.

3.3.1 Description of the model

Gas-phase reactions considered in our model are shown in Table 3.1. Reactions G_1–G_2 and G_3–G_5 are initial fragmentation processes for the combinations of

Tab. 3.1: Gas-phase reactions and their rate constants. Rate constants are given in cm^2 s^{-1} unless otherwise noted. () indicates quantum yield.

No.	Reactants		Products	Rate constant
	Photolysis			
G_1	$SiH_4 + 147nm$	$\rightarrow$	$SiH_3 + H$	1.10×10^{-7} (17%)
G_2		$\rightarrow$	$SiH_2 + H + H$	5.38×10^{-7} (83%)
G_3	$Si_2H_6 + 147nm$	$\rightarrow$	$SiH_3 + SiH_2 + H$	1.48×10^{-6} (61%)
G_4		$\rightarrow$	$Si_2H_4 + H + H$	5.10×10^{-7} (21%)
G_5		$\rightarrow$	$Si_2H_5 + H$	4.37×10^{-7} (18%)
G_6	$Si_2H_6 + 185nm$	$=$	G_3, G_4 or G_5	1.71×10^{-7}
	Secondary reactions			
G_7	$SiH_4 + H$	$\rightarrow$	$SiH_3 + H_2$	2.67×10^{-12}
G_8	$SiH_4 + SiH_2$	$\rightarrow$	$Si_2H_6^*$	1.00×10^{-11}
G_9	$SiH_4 + SiH_3$	$\rightarrow$	$Si_2H_5 + H_2$	1.78×10^{-15}
G_{10}	$SiH_4 + Si_2H_5$	$\rightarrow$	$Si_2H_6 + SiH_3$	5.00×10^{-13}
G_{11}	$Si_2H_6 + H$	$\rightarrow$	$SiH_3 + SiH_4$	1.11×10^{-12}
G_{12}	$Si_2H_6 + H$	$\rightarrow$	$Si_2H_5 + H_2$	2.16×10^{-12}
G_{13}	$Si_2H_6 + SiH_2$	$\rightarrow$	Si_3H_8	1.20×10^{-10}
G_{14}	$Si_2H_6 + SiH_3$	$\rightarrow$	$SiH_4 + Si_2H_5$	1.00×10^{-12}
G_{15}	$H_2 + Si_2H_4$	$\rightarrow$	$SiH_4 + SiH_2$	5.91×10^{-9}
G_{16}	$Si_2H_6^*$	$\rightarrow$	$Si_2H_4 + H_2$	5.00×10^6 s^{-1}
G_{17}	$Si_2H_6^* + Ar$	$\rightarrow$	$Si_2H_6 + Ar$	1.00×10^{-10}
G_{18}	$Si_2H_6^{**}$	$\rightarrow$	$Si_2H_4 + H_2$	2.30×10^7 s^{-1}
G_{19}	$Si_2H_6^{**}$	$\rightarrow$	$SiH_2 + SiH_4$	2.30×10^7 s^{-1}
G_{20}	$Si_2H_6^{**} + Ar$	$\rightarrow$	$Si_2H_6 + Ar$	1.99×10^{-10}
G_{21}	$SiH_2 + H$	$\rightarrow$	SiH_3	1.11×10^{-12}
G_{22}	$SiH_2 + SiH_3$	$\rightarrow$	Si_2H_5	3.77×10^{-13}
G_{23}	$SiH_3 + SiH_3$	$\rightarrow$	$SiH_2 + SiH_4$	6.99×10^{-12}
G_{24}	$SiH_3 + SiH_3$	$\rightarrow$	$Si_2H_6^{**}$	1.00×10^{-11}

SiH_4 + 147 nm and Si_2H_6 + 147 nm, respectively, which were taken from previous reports [14, 15]. On the other hand, there are no reports regarding initial processes for the combination of Si_2H_6 + 185 nm. Analogous to 147 nm photolysis of Si_2H_6, we have tried three kinds of simulations using reactions G_3, G_4 and G_5. The appropriateness of these three kinds of initial photolysis is investigated further by performing surface-reaction simulations, and by comparing their results with experimental ones.

Values of reaction rate constant k for the initial fragmentation processes are estimated from the photo absorption cross section σ of the source gases using the relationship $k = \sigma c$ (c is the velocity of light), where it is assumed that all the absorbed photons contribute to the fragmentation of the source gas molecules according to their quantum yields. The photo absorption cross sections used here are 5.71×10^{-18}, 8.10×10^{-17} and 2.16×10^{-17} cm^2 for the combinations of Si_2H_6 + 185 nm, Si_2H_6 + 147 nm and SiH_4 + 147 nm, respectively [5]. Attenuation of the light intensity in the propagation direction due to absorption by the source gas is also taken into account in the simulation. Light intensity for 185 nm at a window is 5.3 mW/cm^2, which has been estimated from the value measured at a distance of 2 cm from the window of the light source. Light intensity for 147 nm is 1.4 mW/cm^2, which has been estimated by measuring initial decomposition speed of Si_2H_6 in a closed reactor [3].

3.3.2 Density of radicals

Calculated results for the combinations of SiH_4 + 147 nm, Si_2H_6 + 147 nm and Si_2H_6 + 185 nm are shown in Figs.3.7(a), 3.7(b) and 3.7(c), respectively. In these figures, the density of monoradicals, such as SiH_3 and Si_2H_5, is higher than that of biradicals, such as SiH_2 and Si_2H_4, even though the quantum yields of monoradicals at initial photolysis are equal to or less than those of biradicals. This is due to the fact that reactivity of monoradicals is lower than that of biradicals as can be seen in Table 3.1. The features described above are common to the three combinations. However, there is a difference between the ratios of densities for the biradicals and monoradicals, where the main biradical is SiH_2 and the main monoradicals are SiH_3 and Si_2H_5. The ratio of biradical density against monoradical density in the case of SiH_4 + 147 nm is higher than those in the other cases. The use of monoradicals is said to result in good properties in deposited films, such as Si-H dominant structure and low defect-state density, whereas the use of biradicals is said to result in poor

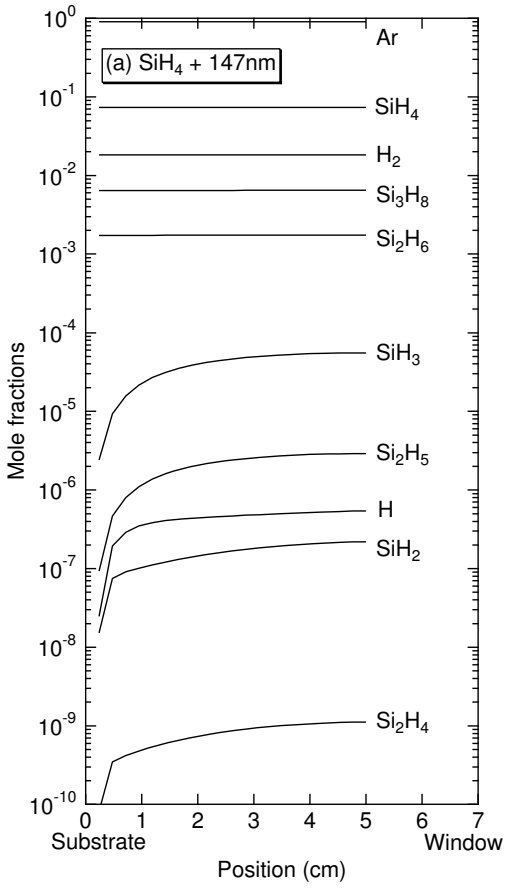

(a) SiH_4 + 147 nm

Fig. 3.7: Gas-phase composition profile between the substrate and the window of a light source for the combination of (a) SiH_4 + 147 nm.

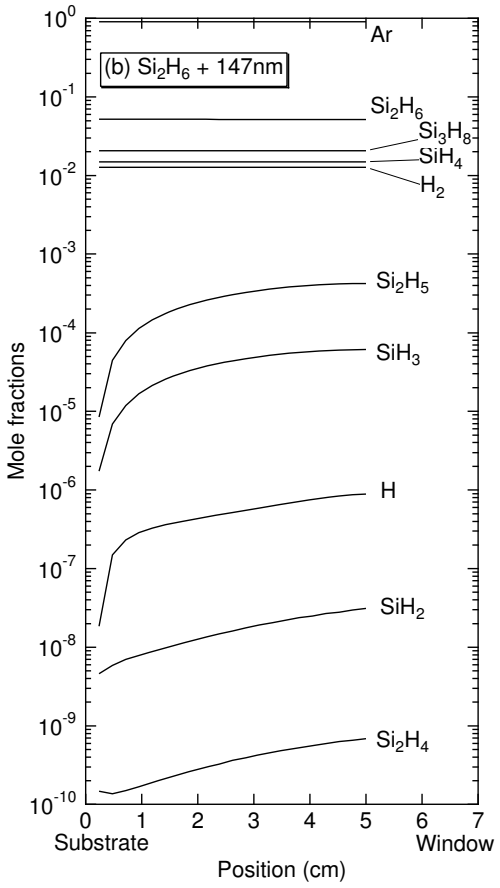

(b) Si_2H_6 + 147 nm

Fig. 3.7: Gas-phase composition profile between the substrate and the window of a light source for the combination of (b) Si_2H_6 + 147 nm.

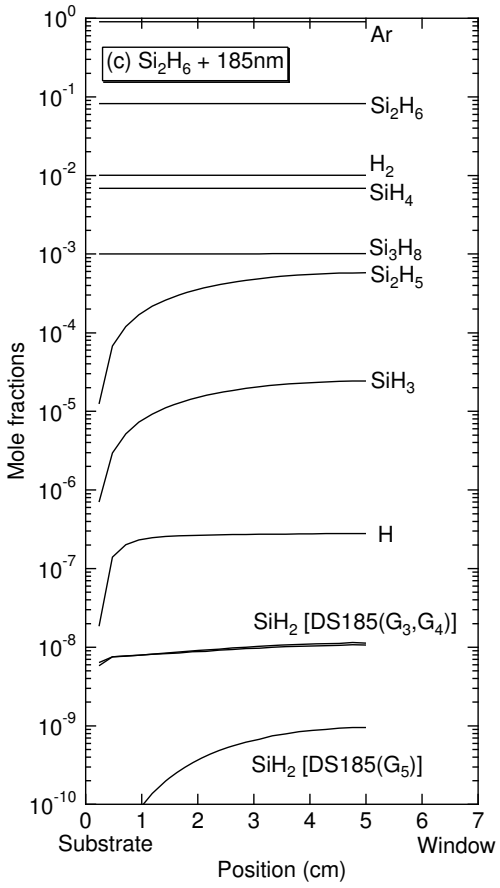

(c) Si_2H_6 + 185 nm

Fig. 3.7: Gas-phase composition profile between the substrate and the window of a light source for the combination of (c) Si_2H_6 + 185 nm.

properties. Therefore, poor properties of films deposited with SiH_4 + 147 nm are considered to be due to the larger contribution of the biradicals. There is also a difference in the density of monoradicals. The dominant monoradical in the case of SiH_4 + 147 nm is SiH_3, whereas that in the case of Si_2H_6 + 147 nm and 185 nm is Si_2H_5. In the next section, we discuss the causes of the differences in the gas-phase radical composition in detail.

3.3.3 Reaction kinetics

For the purpose of detailed analysis of gas-phase reactions, flow diagrams are drawn as shown in Fig.3.8 and 3.9, which represent diagrams of generation and consumption for monoradicals and biradicals, respectively.

Monoradicals

The flow diagram for monoradicals in the case of SiH_4 + 147 nm is shown in Fig.3.8(a). This figure shows that SiH_3 is mainly generated by the reactions G_7 (49%) and G_{10} (44%). G_7 is the reaction of parent gas SiH_4 with atomic hydrogen generated at initial photolysis. Although G_{10} is the reaction of SiH_4 with Si_2H_5, Si_2H_5 originates in SiH_3 generated by G_7. The contribution of initial photolysis G_1 is as small as 5%. Therefore, we can conclude that main monoradical SiH_3 in the case of SiH_4 + 147 nm is mainly generated by secondary reactions, especially by the reaction involving atomic hydrogen. The reason why the density of SiH_3 is higher than that of Si_2H_5 is explained using the same figure. As can be seen in this figure, SiH_3 is generated directly from parent gas SiH_4. In contrast, Si_2H_5 is generated through SiH_3, and the generation of one Si_2H_5 molecule needs three SiH_3 molecules, two for G_{24} to generate Si_2H_6 and one for G_{14} to generate Si_2H_5 from Si_2H_6. Therefore, the generation of Si_2H_5 is not very frequent compared with that of SiH_3 and it results in lower density of Si_2H_5 as can be seen in Fig.3.8(a).

For the combination of Si_2H_6 + 147 nm, the main monoradical is Si_2H_5 even though SiH_3 is generated with the highest quantum yield of 61% at initial photolysis. This result is explained using the flow diagram shown in Fig.3.8(b). As can be seen in this figure, generation and consumption of Si_2H_5 comprise a closed reaction loop, and the generation and consumption proceed through only two reactions G_{14} and G_{10}. Initial photolysis reactions, G_3, G_4 and G_5, work only as triggers for this reaction loop, which is indicated by ① and ② in

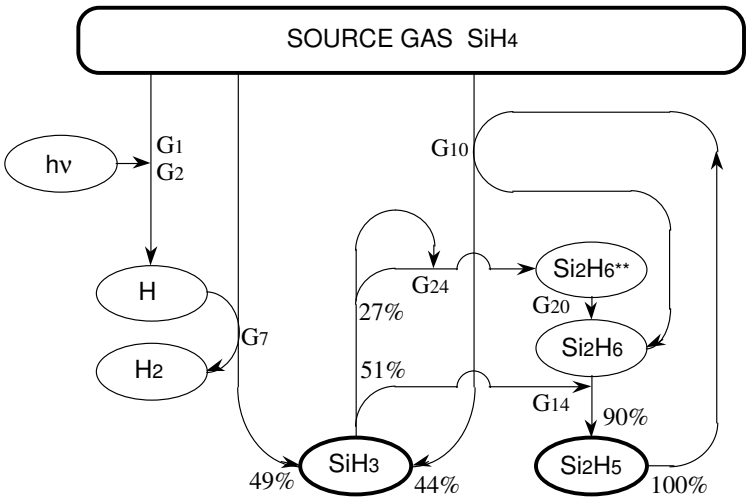

(a) SiH_4 + 147 nm

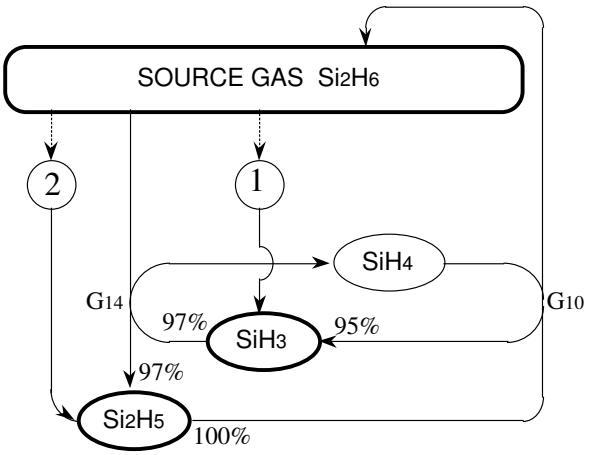

(b) Si_2H_6 + 147 nm

Fig. 3.8: Flow diagrams of generation and consumption pathways of monoradicals for the combinations of (a) SiH_4 + 147 nm and (b) Si_2H_6 + 147 nm. The reaction pathway whose probability is less than 10% is not drawn in these figures.

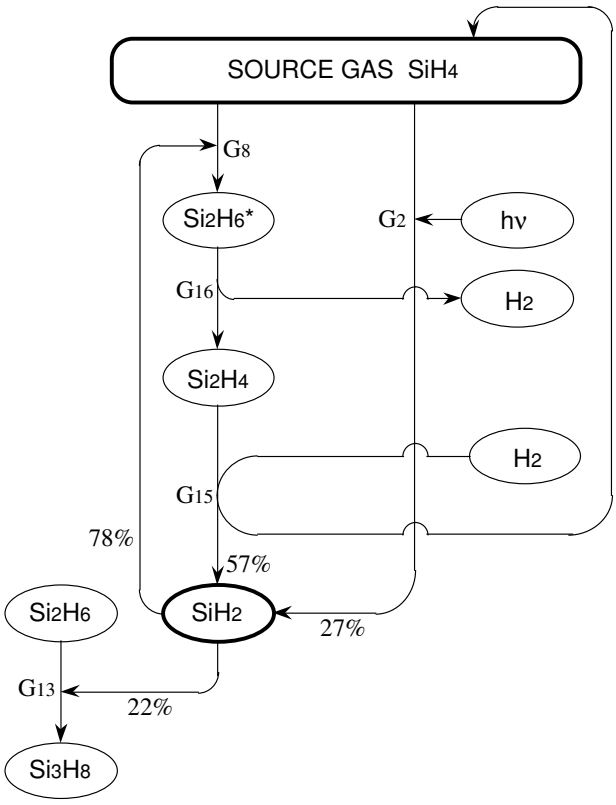

(a) SiH_4 + 147 nm

Fig. 3.9: Flow diagrams of generation and consumption pathway of SiH_2 for the combinations of (a) SiH_4 + 147 nm, (b) Si_2H_6 + 147 nm, and Si_2H_6 + 185 nm using (c) G_3, (d) G_4 and (e) G_5 as the initial photolysis reaction. The reaction pathways whose probability is less than 10% is not drawn in these figures.

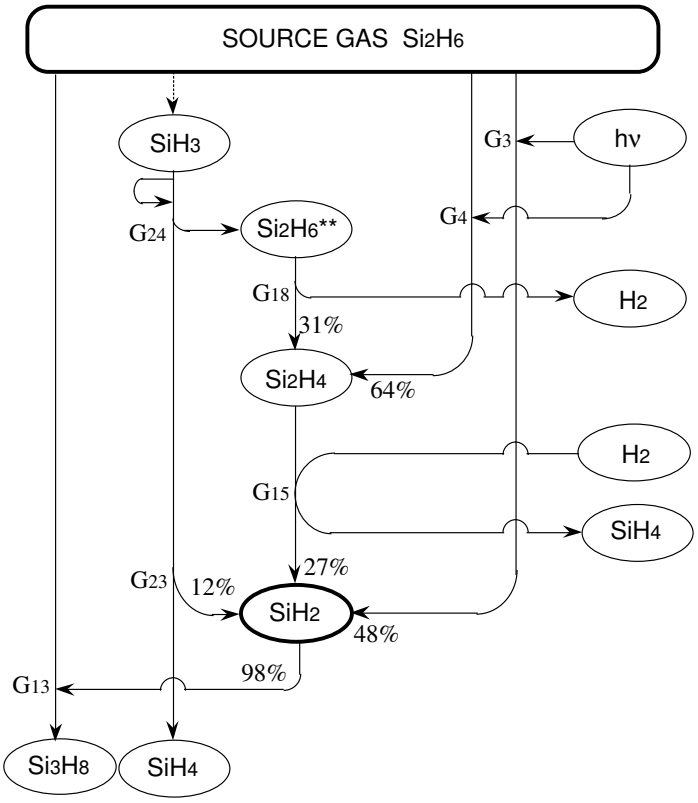

(b) Si_2H_6 + 147 nm

Fig. 3.9: Flow diagrams of generation and consumption pathway of SiH_2 for the combinations of (a) SiH_4 + 147 nm, (b) Si_2H_6 + 147 nm, and Si_2H_6 + 185 nm using (c) G_3, (d) G_4 and (e) G_5 as the initial photolysis reaction. The reaction pathways whose probability is less than 10% is not drawn in these figures.

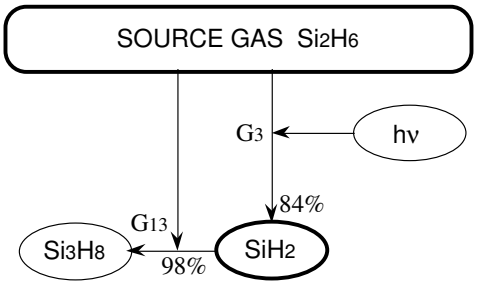

(c) Si_2H_6 + 185 nm with G_3

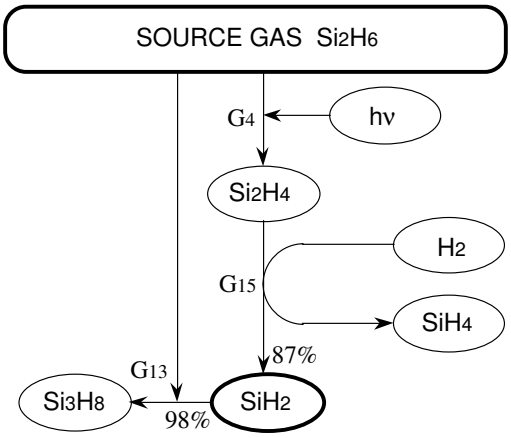

(d) Si_2H_6 + 185 nm with G_4

Fig. 3.9: Flow diagrams of generation and consumption pathway of SiH_2 for the combinations of (a) SiH_4 + 147 nm, (b) Si_2H_6 + 147 nm, and Si_2H_6 + 185 nm using (c) G_3, (d) G_4 and (e) G_5 as the initial photolysis reaction. The reaction pathways whose probability is less than 10% is not drawn in these figures.

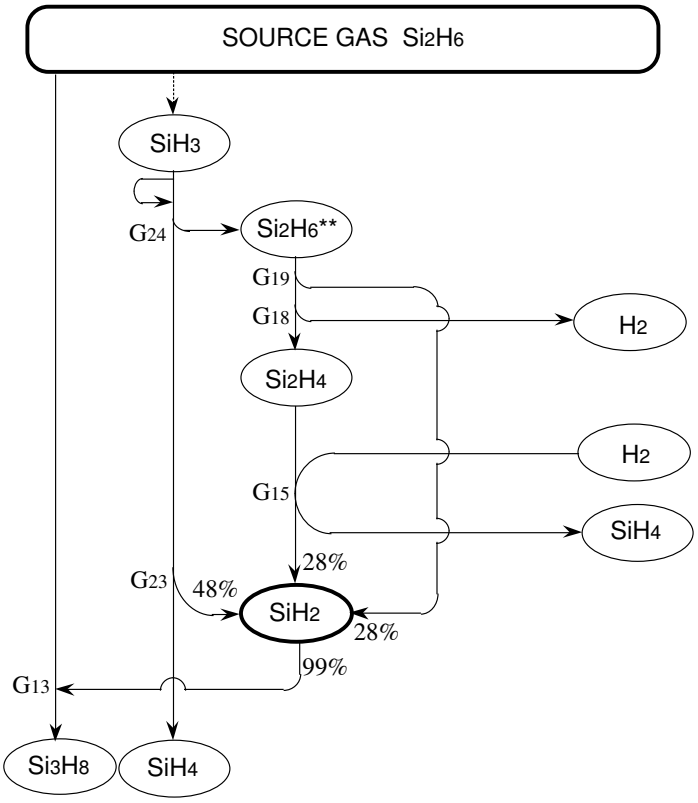

(e) Si_2H_6 + 185 nm with G_5

Fig. 3.9: Flow diagrams of generation and consumption pathway of SiH_2 for the combinations of (a) SiH_4 + 147 nm, (b) Si_2H_6 + 147 nm, and Si_2H_6 + 185 nm using (c) G_3, (d) G_4 and (e) G_5 as the initial photolysis reaction. The reaction pathways whose probability is less than 10% is not drawn in these figures.

Tab. 3.2: Reaction probability for the generation and consumption of monoradicals, in the case of Si_2H_6 + 185 nm.

	Reaction probability			
Products of initial	Si_2H_5		SiH_3	
photolysis	Generation	Consumption	Generation	Consumption
Si_2H_6+185nm	through G_{14}	through G_{10}	through G_{10}	through G_{14}
G_3: SiH_3+SiH_2+H	98%	100%	95%	99%
G_4: Si_2H_4+H+H	96%	100%	97%	98%
G_5: Si_2H_5+H	92%	100%	98%	99%

this figure. Therefore, the following equation is derived:

$$\frac{d[Si_2H_5]}{dt} = k_{14}[Si_2H_6][SiH_3] - k_{10}[SiH_4][Si_2H_5]. \tag{3.1}$$

At a steady state, the ratio between the density of Si_2H_5 and SiH_3 is given as follows:

$$\frac{[Si_2H_5]}{[SiH_3]} = \frac{k_{14}}{k_{10}}\frac{[Si_2H_6]}{[SiH_4]} = 2\frac{[Si_2H_6]}{[SiH_4]}. \tag{3.2}$$

In this equation, the density of Si_2H_6 is higher than that of SiH_4, since Si_2H_6 is the parent gas and the light intensity is not high enough to lead the drastic decrease in the density of Si_2H_6. Therefore, the density of Si_2H_5 becomes higher than that of SiH_3.

For the combination of Si_2H_6 + 185 nm, the results using G_3, G_4 and G_5 are similar to the results of Si_2H_6 + 147 nm for the density of monoradicals. Since the flow diagrams for these three cases are also similar, only the reaction probabilities are listed in Table 3.2. As in the case of Fig.3.8(b), SiH_3 and Si_2H_5 are mainly generated by the secondary reactions G_{10} and G_{14} for all cases. Therefore, when both SiH_3 and Si_2H_5 are generated at initial photolysis, the monoradical compositions in the steady state become almost the same, even if their quantum yield is different. The initial fragmentation of the parent gas assumed in this work always accompanies generation of atomic hydrogen, and the atomic hydrogen generates both SiH_3 and Si_2H_5 through reactions G_{11} and G_{12}. Therefore, it is concluded that the gas-phase composition of monoradicals does not show explicit differences from the case of Si_2H_6 + 147 nm, as long as atomic hydrogen is generated and the same source gas is used.

Biradicals

The flow diagram for the case of SiH_4 + 147 nm is shown in Fig.3.9(a). As shown in this figure, secondary reaction G_{15} generates SiH_2 with larger probability (57%) than photolysis G_2 (27%). However, reaction G_{15} is basically caused by initially generated SiH_2, because the reactant Si_2H_4 in G_{15} is produced from SiH_2 through reactions G_{16} and G_8. Therefore, it is concluded that SiH_2 is generated mainly by the initial photolysis in this case. Generation by other secondary reactions, G_{19} and G_{23}, is negligible because of their low probability, i.e., less than 10%. This is due to the fact that these reactions are caused by SiH_3 or species produced by SiH_3, and SiH_3 is mainly consumed by reaction G_9 with the parent gas. The consumption of SiH_2 is discussed later.

In the case of Si_2H_6 + 147 nm, generation of the main biradical, SiH_2, is caused by initial photolysis G_3 with a probability of 48% as shown in Fig.3.9(b). As in the case of SiH_4 + 147 nm, G_{15} also contributes to the generation of SiH_2 with a probability as high as 27%. However, G_{15} originates basically in initial photolysis G_4 as can be seen in this figure. Therefore, the generation of SiH_2 in this case is also concluded to be mainly due to the initial photolysis.

In the case of Si_2H_6 + 185 nm, the density of SiH_2 using G_3 and G_4 is similar to that for Si_2H_6 + 147 nm. As can be seen in Figs.3.9(c) and 3.9(d), this is due to the fact that SiH_2 is generated basically by the initial photolysis. Although Si_2H_4 is generated on the way to the production of SiH_2 when G_4 is adopted, it rapidly turns into SiH_2 through G_{15}. This indicates that the generation of Si_2H_4 is equivalent to the generation of SiH_2 in the first step. In contrast, the result obtained using G_5 shows a SiH_2 molar fraction much lower than those obtained using G_3 and G_4. This difference is due to the fact that there are no explicit reactions connected to the initial photolysis as can be seen in Fig.3.9(e).

As far as characterizing the generation mechanism of SiH_2 is concerned, only the combination of Si_2H_6 + 185 nm using G_5 showed an explicit difference. However, the density of SiH_2 in the case of Si_2H_6 + 147 nm is lower than that of SiH_4 + 147 nm. Therefore, we discuss this difference by investigating the mechanism of SiH_2 consumption.

In the case of SiH_4 + 147 nm, SiH_2 consumption mainly occurs by the association reaction G_8 (78%) with SiH_4 and G_{13} (22%) with Si_2H_6 as in Fig.3.9(a). As the parent gas is SiH_4, the probability of occurrence of G_8 is higher than that of G_{13}.

Tab. 3.3: Flux onto growing surface. The flux is given in cm^2s^{-1}.

Species	SiH_4+147nm	Si_2H_6+147nm	Si_2H_6+185nm (G_3)	Si_2H_6+185nm (G_4)	Si_2H_6+185nm (G_5)
H	2.77×10^{13}	2.09×10^{13}	1.78×10^{13}	3.43×10^{13}	2.10×10^{13}
SiH_2	4.42×10^{12}	1.36×10^{12}	1.87×10^{12}	1.71×10^{12}	2.41×10^{8}
SiH_3	1.38×10^{14}	1.01×10^{14}	7.28×10^{13}	7.17×10^{13}	4.09×10^{13}
Si_2H_5	3.80×10^{12}	3.51×10^{14}	2.99×10^{14}	2.52×10^{14}	5.15×10^{14}

In contrast, SiH_2 is mainly consumed through reaction G_{13} with Si_2H_6 in the case of Si_2H_6 + 147 nm as in Fig.3.9(b). The probability of occurrence of G_{13} in this case is almost 100%, because Si_2H_6 is a parent gas.

As shown in Table 3.1, the rate constant of G_{13} is greater than that of G_8 by ten times. This indicates that SiH_2 consumption in the case of Si_2H_6 + 147 nm is more frequent than that in the case of SiH_4 + 147 nm, which explains the fact that the density of SiH_2 in the case of Si_2H_6 + 147 nm is lower than that in the case of SiH_2 + 147 nm. In addition, the product, $Si_2H_6^*$, of G_8 generates SiH_2 again through G_{16} and G_{15}. In contrast, the product, Si_3H_8, of G_{13} is assumed to polymerize, and thus does not to contribute to further reactions in this work.

Therefore, it is concluded that the higher rate constant of SiH_2 consumption reaction and the lower contribution of G_8, which generates SiH_2 again, are the reasons why the density of SiH_2 in the case of Si_2H_6 + 147 nm is lower than that of SiH_4 + 147 nm.

From the analysis of gas-phase reactions, it is concluded that the mono-radical composition is not altered as long as atomic hydrogen is generated at initial photolysis and the same source gas is used. It is also concluded that higher SiH_2 density in the case of SiH_4 + 147 nm compared with that of Si_2H_6 + 147 nm is due to the fact that the rate constant of SiH_2 consumption reaction G_8 in the former case is lower than that of G_{13} in the latter case, and that the product of G_8 produces SiH_2 again while G_{13} does not contribute to production of SiH_2.

Radical flux onto surface

From the simulation of the gas-phase reactions, we can obtain the flux of

radicals arriving at the growing film surface. Results are shown in Table 3.3. As can be seen in the table, SiH_2 flux for the combination of SiH_4 + 147 nm is higher than that of Si_2H_6 + 147 nm and Si_2H_6 + 185 nm. This difference corresponds to the gas-phase density of SiH_2 for each case.

Although the flux density of SiH_2 is lower than that of primary monoradicals, the contribution of SiH_2 to the deposition is large enough to influence the film quality, since its sticking probability is approximately ten times greater than that of monoradicals. In actual fact, the hydrogen bonding configurations of the films deposited with Si_2H_6 + 147 nm and SiH_4 + 147 nm are different. To explain the difference in the structure of deposited films due to the difference in impinging radicals, we propose a model for surface reactions in the next section.

3.4 Surface reaction simulation

In this section, we discuss the behavior of radicals on the growing film surface to explain the film structure obtained for the three different combinations of source gases and excitation wavelengths.

3.4.1 Description of the model

Reactions considered in my model are listed in Tables 3.4, 3.5 and 3.6. In these tables, (G), (F), (M), (A), (S) and (B) denote gas-phase species, flux, mobile species, adsorbed species, surface site and buried site, respectively. The surface and buried sites are specified with their bonding configurations according to Kushner's expression [16]. For example, SDHH denotes a Si atom which is located at a site bonded to one silicon (S), two hydrogen (H) atoms and having one dangling bond (D). Hydrogen bonding configurations, such as Si-H and Si-H_2, are denoted as SSSH(B) and SSHH(B), respectively.

Reactions S_1–S_4 in Table 3.4 describe the sticking of radicals impinging on the surface, and reactions S_5–S_{10} stand for the pairing between mobile sites which produce volatile species. Some of monoradicals are desorbed out of the surface by these reactions, and the rest undergo reactions S_{11}–S_{42} in Table 3.5. Reactions S_{11}–S_{42} describe the interactions between the site and radicals on the surface. These are classified into three groups according to T_{sub}. Each group contains three types of reactions:

Tab. 3.4: Surface Reactions I. Sticking of radical species and their desorption through pairing reaction between them.

No.	Reactants		Products
	Sticking of radicals		
S_1	H(F)	→	H(M)
S_2	SiH_3(F)	→	SiH_3(M)
S_3	Si_2H_5(F)	→	Si_2H_5(M)
S_4	SiH_2(F)	→	SiH_2(A)
	Pairing and desorption of radicals		
S_5	H(M) + H(M)	→	H_2(G)
S_6	H(M) + SiH_3(M)	→	SiH_4(G)
S_7	H(M) + Si_2H_5(M)	→	Si_2H_6(G)
S_8	SiH_3(M) + SiH_3(M)	→	Si_2H_6(G)
S_9	SiH_3(M) + Si_2H_5(M)	→	Si_3H_8(G)
S_{10}	Si_2H_5(M) + Si_2H_5(M)	→	Si_4H_{10}(G)

1. hydrogen abstraction from hydrogen-saturated sites by monoradicals (creation of dangling bond site),

2. adsorption onto dangling bond sites (deposition), and

3. insertion of SiH_2 radicals into hydrogen-saturated sites (deposition).

In these reactions, the asterisk indicates that the sites originate in SiH_2, and these sites are distinguished from the sites with other origins. Reactions S_{43}–S_{54} in Table 3.6 are cross-linking reactions between surface sites. As the cross-linking between two sites on the same plane is not likely, I have considered that the interconnection occurs between a surface site X(S) and a buried site Y(B) which is located on the layer beneath the top surface. Cross-linking between SSSH(S) and Y(B) is also not likely due to their geometrical configuration. Therefore, this reaction has also been omitted from the table. In the next section, I describe the flow of these reactions at three different $T_{\rm sub}$ regions using the flow diagram shown in Fig.3.10.

Tab. 3.5: Surface Reactions II. Reactions between a surface site and a mobile or adsorptive radicals impinged on the surface.

No.	Reactants		Products
	Reactions at low temperature		
S_{11}	SHHH(S) + H(M)	→	SDHH(S) + H_2(G)
S_{12}	SHHH(S) + SiH_3(M)	→	SDHH(S) + SiH_4(G)
S_{13}	SHHH(S) + Si_2H_5(M)	→	SDHH(S) + Si_2H_6(G)
S_{14}	SHHH(S) + SiH_2(A)	→	SHHH(S)* + SSHH(B)
S_{15}	SDHH(S) + H(M)	→	SHHH(S)
S_{16}	SDHH(S) + SiH_3(M)	→	SHHH(S) + SSHH(B)
S_{17}	SDHH(S) + Si_2H_5(M)	→	SHHH(S) + SSHH(S) + SSHH(B)
S_{18}	SDHH(S) + SiH_2(A)	→	SDHH(S)* + SSHH(B)
S_{19}	SHHH(S)* + H(M)	→	SDHH(S)* + H_2(G)
S_{20}	SHHH(S)* + SiH_3(M)	→	SDHH(S)* + SiH_4(G)
S_{21}	SHHH(S)* + Si_2H_5(M)	→	SDHH(S)* + Si_2H_6(G)
S_{22}	SHHH(S)* + SiH_2(A)	→	SHHH(S)* + SSHH(B)
S_{23}	SDHH(S)* + H(M)	→	SHHH(S)∗
S_{24}	SDHH(S)* + SiH_3(M)	→	SHHH(S) + SSHH(B)
S_{25}	SDHH(S)* + Si_2H_5(M)	→	SHHH(S)* + SSHH(S)* + SSHH(B)
S_{26}	SDHH(S)* + SiH_2(A)	→	SDHH(S)* + SSHH(B)
	Reactions at moderate temperature		
S_{27}	SSHH(S) + H(M)	→	SSDH(S) + H_2(G)
S_{28}	SSHH(S) + SiH_3(M)	→	SSDH(S) + SiH_4(G)
S_{29}	SSHH(S) + Si_2H_5(M)	→	SSDH(S) + Si_2H_6(G)
S_{30}	SSHH(S) + SiH_2(A)	→	SHHH(S)* + SSSH(B)
S_{31}	SSDH(S) + H(M)	→	SSHH(S)
S_{32}	SSDH(S) + SiH_3(M)	→	SHHH(S) + SSSH(B)
S_{33}	SSDH(S) + Si_2H_5(M)	→	SHHH(S) + SSHH(S) + SSSH(B)
S_{34}	SSDH(S) + SiH_2(A)	→	SDHH(S)* + SSSH(B)
	Reactions at high temperature		
S_{35}	SSSH(S) + H(M)	→	SSSD(S) + H_2(G)
S_{36}	SSSH(S) + SiH_3(M)	→	SSSD(S) + SiH_4(G)
S_{37}	SSSH(S) + Si_2H_5(M)	→	SSSD(S) + Si_2H_6(G)
S_{38}	SSSH(S) + SiH_2(A)	→	SHHH(S)* + SSSS(B)
S_{39}	SSSD(S) + H(M)	→	SSSH(S)
S_{40}	SSSD(S) + SiH_3(M)	→	SHHH(S) + SSSS(B)
S_{41}	SSSD(S) + Si_2H_5(M)	→	SHHH(S) + SSHH(S) + SSSS(B)
S_{42}	SSSD(S) + SiH_2(A)	→	SDHH(S)* + SSSS(B)

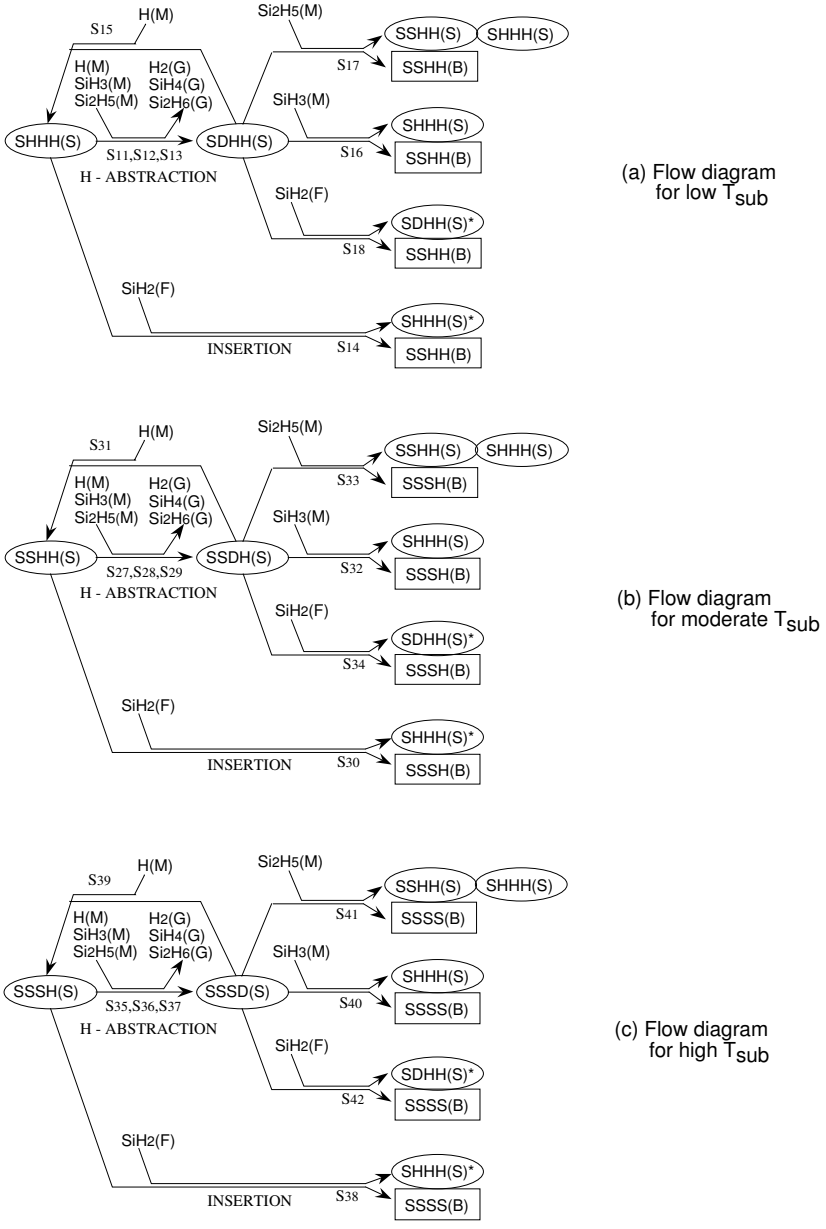

Fig. 3.10: Flow diagrams of surface reactions starting from (a) SHHH(S), (b) SSHH(S) and (c) SSSH(S). The starting site shifts from SHHH(S) to SSSH(S) by interconnection reactions listed in Table VI with increasing $T_{\rm sub}$. Reaction schemes involving SHHH(S)* and SDHH(S)* are the same as those involving SHHH(S) and SDHH(S), and only their rate constant are different as shown in Table 3.4–3.6.

Tab. 3.6: Surface Reactions III. Cross-linking reactions between a surface site and a buried site. Rate constants are given in the form of$k = A\exp(-E/RT)$.

No.	Reactants		Products	A (cm^2s^{-1})	E/R (K)
S_{43}	SSHH(B)+SHHH(S)	→	SSSH(B)+SSHH(S)+H_2(G)	1.0×10^{-10}	6000
S_{44}	SSHH(B)+SDHH(S)	→	SSSH(B)+SSDH(S)+H_2(G)	1.0×10^{-10}	6000
S_{45}	SSHH(B)+SSHH(S)	→	SSSH(B)+SSSH(S)+H_2(G)	1.0×10^{-10}	6000
S_{46}	SSHH(B)+SSDH(S)	→	SSSH(B)+SSSD(S)+H_2(G)	1.0×10^{-10}	6000
S_{47}	SSHH(B)+SHHH(S)*	→	SSSH(B)+SSSD(S)+H_2(G)	1.0×10^{-11}	6000
S_{48}	SSHH(B)+SDHH(S)*	→	SSSH(B)+SSDH(S)+H_2(G)	1.0×10^{-11}	6000
S_{49}	SSSH(B)+SHHH(S)	→	SSSS(B)+SSHH(S)+H_2(G)	5.0×10^{-16}	800
S_{50}	SSSH(B)+SDHH(S)	→	SSSS(B)+SSDH(S)+H_2(G)	5.0×10^{-16}	800
S_{51}	SSSH(B)+SSHH(S)	→	SSSS(B)+SSSH(S)+H_2(G)	5.0×10^{-16}	800
S_{52}	SSSH(B)+SSDH(S)	→	SSSS(B)+SSSD(S)+H_2(G)	5.0×10^{-16}	800
S_{53}	SSSH(B)+SHHH(S)*	→	SSSS(B)+SSHH(S)+H_2(G)	5.0×10^{-17}	800
S_{54}	SSSH(B)+SDHH(S)*	→	SSSS(B)+SSDH(S)+H_2(G)	5.0×10^{-17}	800

3.4.2 Reactions at low temperature

At low T_{sub}, the probability of occurrence of hydrogen desorption reactions listed in Table 3.6 is small due to their finite activation energies. Therefore, if Si_2H_5 does not contribute to deposition, the surface sites are SHHH(S), SDHH(S), SHHH(S)* and SDHH(S)*, because any site can become one of these sites by deposition of radicals as shown in Figs.3.10(a), 3.10(b) and 3.10(c). Reaction schemes involving SHHH(S)* and SDHH(S)* are the same as those involving SHHH(S) and SDHH(S) although the schemes are not shown in these figures.

Deposition of SiH_3 proceeds through the well-known two-step mechanism [17] as shown in Fig.3.10(a); that is, SiH_3 deposits through hydrogen abstraction S_{12} from hydrogen saturated site SHHH(S) and adsorption S_{16} on SDHH(S) created by the former process. The resulting bulk site is SSHH(B), namely Si-H_2 bonds. Therefore, even if the main radical is SiH_3, Si-H_2 bonds tend to be created at low T_{sub} where the cross-linking rate is lower than the adsorption rate. This is consistent with the experimental results, because the density of Si-H_2 bonds increases as T_{sub} decreases even in SiH_3-rich conditions

such as in Hg-sensitized photo-CVD [18].

On the other hand, deposition of SiH_2 proceeds through a one-step mechanism, because SiH_2 deposits even on hydrogen saturated site SHHH(S) by an insertion reaction S_{14} as in Fig.3.10(a). This radical also creates Si-H_2 bonds. As for deposition of Si_2H_5, SSHH(S) is created by S_{17} in my model in addition to SHHH(S). The site SSHH(S) turns into Si-H bonds in the films through reactions S_{27}–S_{34} as in Fig.3.10(b), which appear at higher $T_{\rm sub}$ through cross-linking reactions S_{43} and S_{49} in the case of SiH_3-rich conditions. This indicates that a site for creating a Si-H bond is formed when Si_2H_5 is adsorbed on a dangling-bond site, and the site does not need thermally activated cross-linking to form Si-H bonds. Low values of N(Si-H_2)/N(Si-H) in the case of Si_2H_6 + 147 nm and 185 nm shown in Fig.3.4 can be understood by considering this reaction scheme, since the flux of Si_2H_5 which creates Si-H bonds is dominant for these cases. Another reaction scheme, which produce SSHH(B) instead of SSHH(S), can also be considered; that is,

$$\mathrm{SDHH(S)} + \mathrm{Si_2H_5} \rightarrow \mathrm{SHHH(S)} + \mathrm{SSHH(B)} + \mathrm{SSHH(B)} \tag{3.3}$$

However, if we assume that this reaction occurs, hydrogen concentration in the films becomes higher than that in SiH_3-rich conditions by approximately two times, since two sites with hydrogen are buried at the same time. This scheme cannot explain the experimental results for Si_2H_6 + 147 nm and 185 nm.

3.4.3 Reactions at moderate temperature

Cross-linking reactions involving SHHH(S), such as S_{43} and S_{49}, begin to take place with increasing $T_{\rm sub}$, and the surface coverage ratio of SSHH(S) increases with desorption of hydrogen. At this temperature, therefore, Si-H bonds can be created by reactions S_{27}–S_{34} shown in Fig.3.10(b). Although SHHH(S) is also formed at the same sequence, this site turns into SSHH(S) at this temperature by cross-linking reactions S_{43} and S_{49} as mentioned above.

Cross-linking reactions S_{47} and S_{48} involving SHHH(S)* and SDHH(S)* which are created from SiH_2 also begin to take place. However, if I introduce them with the same rate constant as the reactions involving SHHH(S) and SDHH(S) (which is referred to as model 1), $C_{\rm H}$ and N(Si-H_2)/N(Si-H) do not increase very much with increasing SiH_2 radical flux as shown in Figs.3.11(a) and 3.11(b). This is not consistent with present experimental results, since

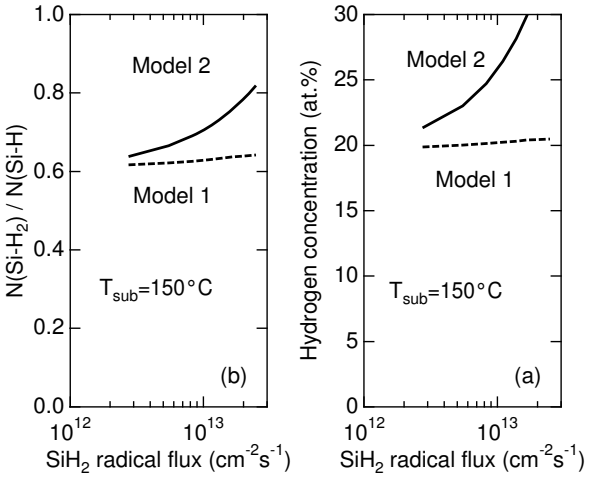

Fig. 3.11: (a) Hydrogen concentration C_{H} and (b) its bonding configuration N(Si-H_2)/N(Si-H) as a function of flux density of SiH_2 for two models. In model 1, the interconnection rates for SHHH(S)* and SDHH(S)* are equal to those for SHHH(S) and SDHH(S). In model 2, these rates are distinguished from each other.

films deposited with SiH_4 + 147 nm, in which the contribution of SiH_2 is larger than in the other cases, show higher C_{H} and N(Si-H_2)/N(Si-H) values than that with Si_2H_6 + 147 nm. In addition, recent study on PE-CVD of a-Si:H, in which SiH_2 radical density has been measured, shows that the Si-H_2 bond density increases with increasing SiH_2 radical density by dilution with rare gases [19]. To increase Si-H_2 bond density with increasing SiH_2 radical density as in the experimental results, I must propose a decrease in the cross-linking rate of SHHH(S)* and SDHH(S)* as shown in Fig.3.11 (model 2).

Therefore, it is concluded that cross-linking reactions of SHHH(S)* and SDHH(S)* created from SiH_2 is not very frequent compared with that of SHHH(S) and SDHH(S) created from monoradicals. This difference may be explained as follows. The SiH_2 radicals can be adsorbed on any site due to their high reactivity and tend to exist on the same plane, where the cross-linking is difficult due to geometrical factors which results in roughness on the film surface. In contrast, the monoradicals are mobile and tend to be adsorbed on the site adjoining surface irregularities, where the interconnection proceeds more easily, and the surface can become smooth. This consideration is consistent with experimental result [20] and more advanced simulation results [21].

3.4.4 Reactions at high temperature

At high T_{sub}, all of the cross-linking rates become higher than the adsorption rates. Therefore, most of the surface sites are dominated by SSSH(S). This site eventually turns into silicon network SSSS(B) through reactions S_{35}–S_{42}, and the difference in the structure of films deposited under different conditions vanishes. This consideration describes the experimental results shown in Fig.3.4 successfully.

3.4.5 Rate constants

The rate constant for reactions S_1, S_2 and S_3 is 0.1, and that for S_4 is 1.0, which corresponds to the sticking probability of impinging radicals. The rate constant for pairing reactions S_5–S_{10} is selected to be 3.00×10^{-10} cm^2/s so that the probability of pairing of SiH_3 becomes approximately 1% [22]. The rate constant for the reactions between adsorbed species and dangling bond sites is selected to be 1.50×10^{-12} cm^2/s according to Kushner's model [16]. Regarding the reactions between monoradicals and hydrogen-saturated sites, the reaction probability of 0.1 is multiplied by the rate constant so that the probability of occurrence of the hydrogen abstraction reaction becomes approximately 6% [22]. These fittings have been investigated using the flux for 100% SiH_4 plasma; that is, H(F), SiH_2(F), SiH_3(F) and Si_2H_5(F) are 8.03×10^{14}, 2.75×10^{12}, 9.62×10^{14} and 6.03×10^{13} cm^2/s, respectively. As for the cross-linking reactions, their rate constants have been obtained by parametrically comparing the results of this model to the experimental results of N(Si-H_2)/N(Si-H) and C_{H}. The values for S_{43}–S_{54} used in my model are listed in Table 3.6. As mentioned above, the rate constant for cross-linking involving SDHH(S)* and SHHH(S)* is low compared with the value for SDHH(S) and SHHH(S).

3.4.6 Surface composition

With the use of flux listed in Table 3.3 and the surface reaction model given above, the surface coverage ratio, C_{H} and N(Si-H_2)/N(Si-H) are calculated. Calculated coverage ratios of surface sites at the steady state are listed in Table 3.7. In the case of SiH_4 + 147 nm, the density of SDHH(S)*, which is the direct source of Si-H_2 bonds, is approximately two times larger than those in the other cases. This is due to the sticking of the SiH_2 radical onto the dangling bond site XD(S). The site SHHH(S)*, which is the indirect source

Tab. 3.7: Surface coverage at T_{sub}=150°C.

Site	SiH_4 +147nm	Si_2H_6 +147nm	Si_2H_6 +185nm(G_3)	Si_2H_6 +185nm(G_4)	Si_2H_6 +185nm(G_5)
SSSD(S)	0.05	0.03	0.03	0.03	0.05
SSSH(S)	0.42	0.29	0.30	0.31	0.23
SSDH(S)	0.01	0.03	0.03	0.03	0.03
SSHH(S)	0.09	0.33	0.31	0.30	0.38
SDHH(S)*	0.02	0.02	0.02	0.02	0.02
SHHH(S)*	0.18	0.02	0.04	0.04	0.00
SDHH(S)	0.02	0.00	0 00	0.01	0.00
SHHH(S)	0.21	0.28	0.26	0.26	0.31

of Si-H_2 bonds, also shows a larger value than those in the other cases. This is due to insertion of SiH_2 radicals into the Si-H bonds of hydrogen-saturated sites. SSHH(S), which is the indirect source of Si-H bonds, shows a lower value in the case of SiH_4 + 147 nm compared with those in the cases of Si_2H_6 + 147 nm or 185 nm. This is due to the small contribution of Si_2H_5 which forms SSHH(S). A similar tendency is found for the value for SSDH(S) which is created from SSHH(S).

3.4.7 Film structure

Figures 3.12 and 3.13 show the calculated results of C_H and N(Si-H_2)/N(Si-H), respectively. As can be seen in these figures, the results for Si_2H_6 + 185 nm using G_3, G_4 and G_5 do not show notable differences, although the flux of SiH_2 for the case of G_5 is quite low compared with the other cases. Therefore, the appropriateness of the choice of G_3, G_4 or G_5 is not determined by a comparison of the calculated film structure to the experimental results. However, this indicates that SiH_2 density is adequately suppressed in the cases of G_3 and G_4 so that further suppression of SiH_2 density no longer changes the film structure and the film structure obtained in this case is mainly determined by the nature of Si_2H_5. As for the results of the combinations of SiH_4 + 147 nm and Si_2H_6 + 147 nm, the calculated results explain qualitatively the difference in the experimental results. Therefore, it is considered that the model reported in this work is appropriate for prediction of the phenomena

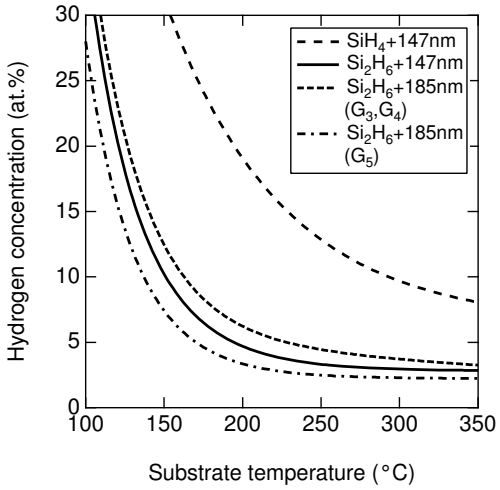

Fig. 3.12: Hydrogen concentration C_{H} obtained by surface reaction simulation for different combinations of excitation wavelengths and source gases.

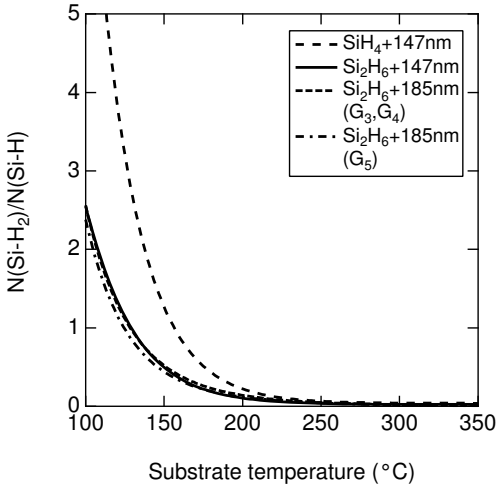

Fig. 3.13: Ratio of $N(\mathrm{Si\text{-}H_2})/N(\mathrm{Si\text{-}H})$ obtained by surface reaction simulation for different combinations of excitation wavelengths and source gases.

on the surface. However, its quantitative agreement with the experimental results is not satisfactory. In a situation where closer quantitative agreement is necessary, a more sophisticated model in three dimensions is required [21].

3.5 Summary

In summary, a-Si:H films have been prepared by a direct photo-CVD method using different excitation wavelengths and source gases. The films deposited with the combination of Si_2H_6 + 147 nm and Si_2H_6 + 185 nm show better properties indicated by low values of Si-H_2 bond density, Urbach energy and defect-state density compared with the films deposited with SiH_4 + 147 nm.

From a simulation of gas-phase and surface reactions, it has been concluded that the good properties are caused by the smaller contribution of biradicals such as SiH_2 and Si_2H_4 and larger contribution of monoradicals such as SiH_3 and Si_2H_5 to deposition of the films.

From the detailed analysis of gas-phase reactions in the VUV photo-CVD using Si_2H_6 gas, it is concluded that the monoradical composition is not altered as long as atomic hydrogen is generated at initial photolysis and the same source gas is used. It is also concluded that the density of SiH_2 is controlled mostly by the reaction scheme of SiH_2 with a parent gas. From the modeling of surface reactions, it is found that cross-linking reactions involving the surface sites created from SiH_2 should be slower than those for the sites created from monoradicals. The cause of this difference is discussed in the next chapter with the aid of a Monte-Carlo simulation.

References

[1] J. Perrin and T. Broekhuizen: Appl. Phys. Lett. **50** (1987) 433.

[2] Y. Matsui, A. Yuuki, N. Morita and K. Tachibana: Jpn. J. Appl. Phys. **26** (1987) 1575.

[3] K. Yoshizawa, M. Taki, K. Tachibana and S. Moriyama: Appl. Phys. Lett. **59** (1991) 1678.

[4] Y. Hishikawa, M. Ohnishi and Y. Kuwano: Mater. Res. Soc. Symp. Proc. **192** (1990) 3.

[5] U. Ito, Y. Toyoshima, H. Onuki, N. Washida and T. Ibuki: J. Chem. Phys. **85** (1986) 4867.

[6] M. Cardona: Phys. Status Solidi B **118** (1983) 463.

[7] H. Wagner and W. Beyer: Solid State Commun. **48** (1983) 585.

[8] J. Perrin, Y. Takeda, N. Hirano, Y. Takeuchi and A. Matsuda: Surf. Sci. **210** (1988) 115.

[9] J. Perrin, I. Solomon, B. Bourdon, J. Fontenielle and E. Ligeon: Thin Solid Films **62** (1979) 327.

[10] M. Vanececk, J. Kocka, J. Stuchlik, Z. Kozisek, O Stika and A. Triska: Sol. Energy Mater. **8** (1983) 411.

[11] T. Shimizu, X. Xu, H. Kidoh, A. Morimoto and M. Kumeda: J. Appl. Phys. **64** (1988) 5045.

[12] K. Winer: Phys. Rev. B **41** (1990) 12150.

[13] A. H. Mahan, A. Mascarenhas, D. L. Williamson and R. S. Crandall: Mater. Res. Soc. Symp. Proc. **118** (1988) 641.

[14] G. G. A. Perkins and F. W. Lampe: J. Am. Chem. Soc. **102** (1980) 3764.

[15] G. G. A. Perkins, E. R. Austin and F. W. Lampe: J. Am. Chem. Soc. **101** (1979) 1109.

[16] M. J. Kushner: J. Appl. Phys. **63** (1988) 2532.

[17] A. Matsuda, K. Nomoto, Y. Takeuchi, A. Suzuki, A. Yuuki and J. Perrin: Surf. Sci. **227** (1990) 50.

[18] S. Kawasaki, K. Sato, K. Suzuki, H. Takeuchi, K. Kuroiwa and Y. Tarui: Jpn. J. Appl. Phys. **26** (1987) 1400.

[19] K. Tachibana, A. Yuuki and Y. Matsui: *Gaseous Electronics and Its Applications*, Ed. R. W. Crompton, M. Hayashi, D. E. Boy and T. Makabe (Kluwer Academic Publishers, Dordrecht, 1991) p.273.

[20] R. W. Collins and J. M. Cavese: J. Appl. Phys. **62** (1987) 4146.

[21] M. J. McCaughy and M. J. Kushner: J. Appl. Phys. **65** (1989) 186.

[22] J. P. M. Schmitt: Thin Solid Films **174** (1989) 193.

Chapter 4

Reaction kinetics in plasma-enhanced chemical vapor deposition of a-Si:H

4.1 Introduction

The model involving only neutral radicals and molecules has been presented in the previous chapter, and applied to corresponding system, namely photo-chemical vapor deposition (photo-CVD). In the realistic and practical plasma-enhanced CVD (PE-CVD) system, however, electrons, ions and electric field must be considered. These parameters do not affect film deposition directly but play important roles such as initial decomposition of source gases, sustenance of plasma and so on, which affect film properties indirectly through radical composition and its spatial profile in gas phase.

In this chapter, therefore, the model is improved to be able to handle these parameters. The deduced radical density is compared to measured one for Si [1], SiH [1], SiH_2 [2] and SiH_3 [3]. Regarding SiH_2, its density variation has been measured under various conditions by using an intracavity laser absorption spectroscopy (ICLAS).

Regarding the surface reactions, the model presented in the previous chapter is described in the way of kinetic method, in which one can not handle the effect of surface migration as demonstrated in the previous chapter. In this chapter, therefore, the model has been improved to be able to handle surface diffusion of the adsorbed species by using a Monte Carlo Method. Predicted surface microstructure is compared to *in situ* monitoring results performed by means of ellipsometry.

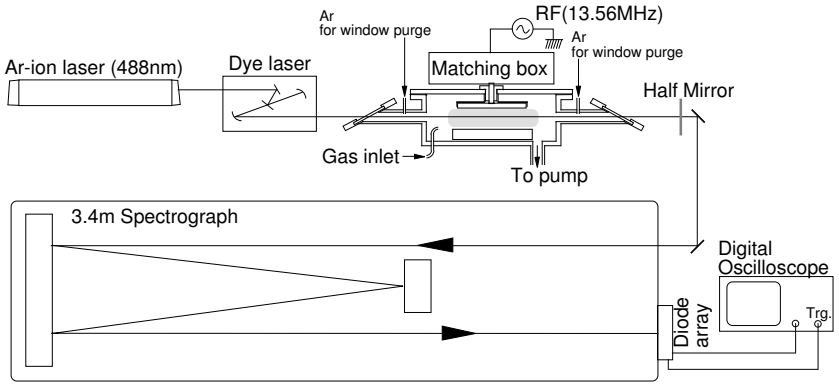

Fig. 4.1: Experimental setup for intracavity laser absorption spectroscopy (ICLAS).

4.2 Measurement of SiH_2 radical density

4.2.1 Experimental procedure

Experimental setup is shown schematically in Fig.4.1. A capacitively coupled RF (13.56 MHz) PE-CVD chamber equipped with Brewster windows at both ends is mounted in the cavity of a cw dye-laser pumped by an argon-ion laser. Powered electrode is in the shape of rectangular (18×5 cm^2) unless otherwise noted, and which is placed above a substrate holder. They are apart 2.5 cm. Detection of SiH_2 radicals is carried out at the center between the powered electrode and substrate holder. Source gases are SiH_4 and Si_2H_6. The dilution gases of He, Ar and Xe are used for modifying plasma condition. The flow rates of the source gases and dilution gases are changed by mass flow controllers. The total pressure in the chamber is monitored by a capacitance manometer. The RF power is monitored by a conventional power meter in front of the matching circuit and changed between 2 and 50 W. Substrate temperature is kept at 150°C.

The dye laser is operated in a wide-band mode with a typical spectral width of about 0.5 nm and the wavelength is controlled by the angle of an intracavity pellicle over the tuning range of rhodamine-6G dye. The output laser beam is fed into a spectrometer of 3.4 m focal length with a grating of 600 lines/mm, of which the reciprocal line dispersion is 0.125 nm/mm at the fourth order. The dispersed spectrum is detected by a linear image sensor with 512 elements at 28 mm pitch, and the signal is averaged by a digitizing oscilloscope over 100 to 1000 times. The wavelength-resolved output signal shows noticeable absorption peaks, other than those from Ar, and impurities

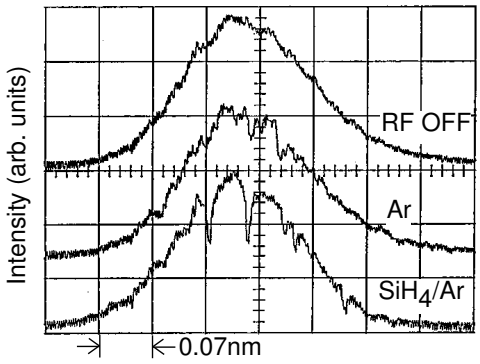

Fig. 4.2: Example of absorption signals of SiH_2 at a wavelength region around 579.5 nm.

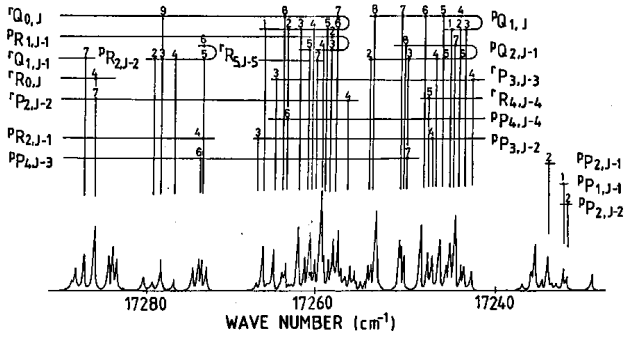

Fig. 4.3: Assigned rotational components of the $(020)' - (000)''$ band in the $\tilde{A}^1B_1$–$\tilde{X}^1A_1$ transition of SiH_2.

when SiH_4 is introduced into the Ar plasma, as shown in Fig.4.2. Parts of the difference spectra obtained with and without SiH_4 are connected together over a range from 17230 to 17290 cm^{-1} and converted into the absorption coefficients. The result thus obtained is shown in Fig.4.3, where most of the peaks can be assigned to the rotational components of the $(020)'$–$(000)''$ band of the $\tilde{A}^1B_1$–$\tilde{X}^1A_1$ transition of SiH_2 [4–6], although there remain a few unassigned components probably due to impurities such as H_2O and H_2.

4.2.2 Absolute density of SiH_2 radicals

Absolute density of SiH_2 radicals measured by Tachibana *et al.* [2] are shown in Fig.4.4. The density of SiH_2 radicals have been measured at the center of the electrode gap as a function of the mixing ratio of SiH_4 in Ar and H_2. In this case, the electrode is disk-shaped, and its diameter and the spacing of

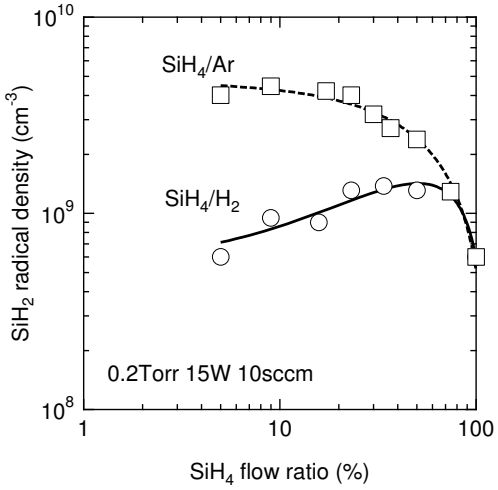

Fig. 4.4: SiH_2 density measured as a function of the SiH_4 mixing ratio in Ar and H_2 at a total pressure of 0.2 Torr, a total flow rate of 10 sccm and an RF power of 15 W. Dashed curves show the dissociation degree of SiH_4 molecules.

the electrode is 8 and 2 cm, respectively. Total pressure, RF power and flow rate is 0.2 Torr, 15 W and 10 sccm, respectively. As can be seen in the figure, absolute density of SiH_2 radicals is in the order of 10^8–10^9 cm^{-3}. Variation in the density of SiH_2 radicals under various conditions is shown in the following sections.

4.2.3 Effects of He, Ar and Xe dilution

Figures 4.5(a), 4.5(b) and 4.5(c) show SiH_2 radical density as a function of source-gas flow ratio in SiH_4 plasma for the RF power ranging from 2 to 50 W. There is a common tendency in these results, that is, the density of SiH_2 radicals increases with the dilution. One possible cause of this tendency is increase of SiH_2 production rate, in other words, increase of dissociation rate of the parent SiH_4 molecules. The dissociation of SiH_4 occurs by impacts of electrons and dilution-gas atoms excited to metastable states. Another possible cause is the decrease of SiH_2 loss rate, since the frequency of attachment reaction of SiH_2 radicals with parent SiH_4 molecules decreases with dilution. Variation in diffusion loss by changing dominant gas with dilution also affects the density of SiH_2 radicals. I will discuss which process is dominant with the aid of simulation.

Figures 4.5(d), 4.5(e) and 4.5(f) show SiH_2 radical density as a function

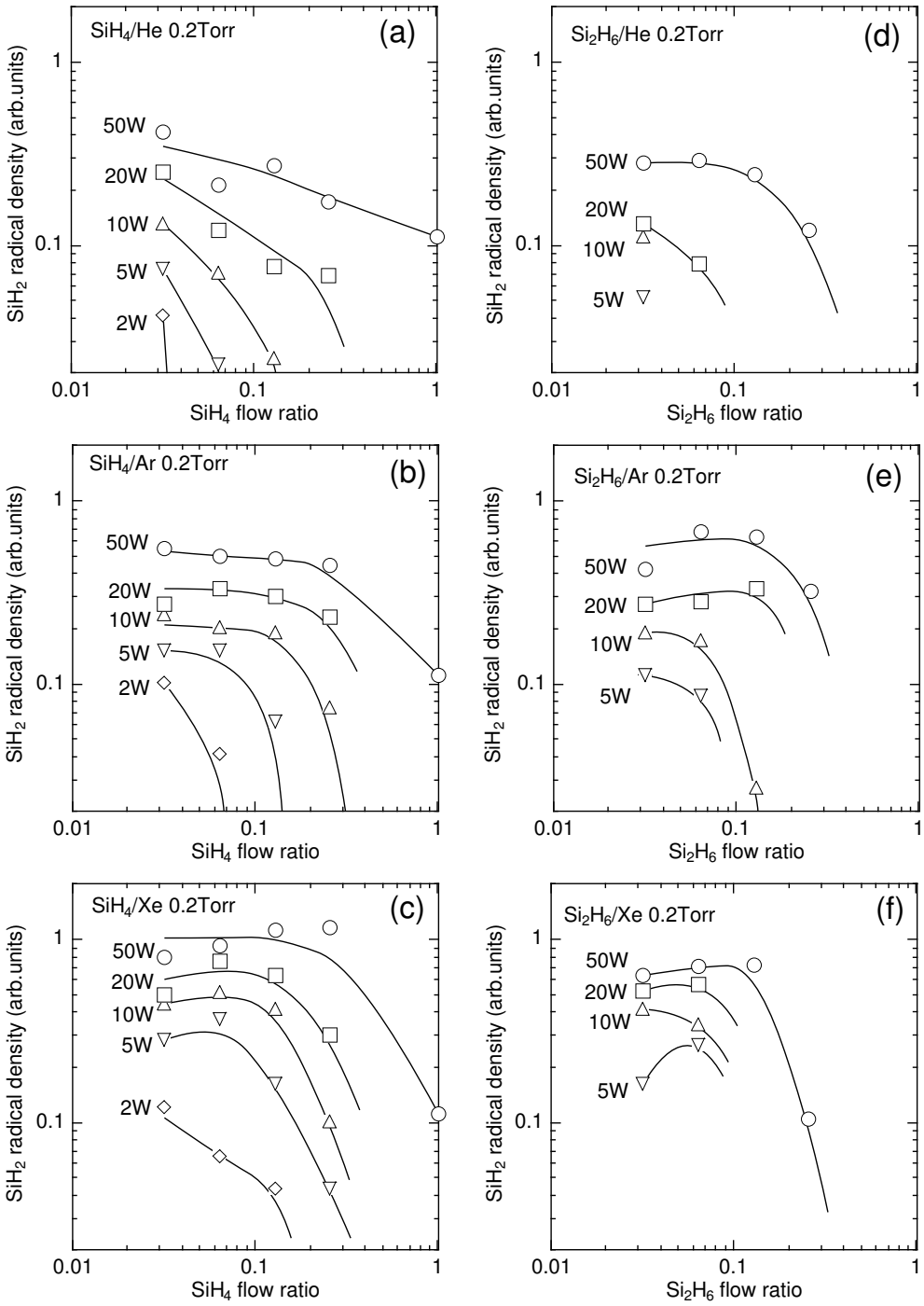

Fig. 4.5: Measured SiH_2 radical density in SiH_4 and Si_2H_6 plasmas diluted with (a,d) He, (b,e) Ar and (c,f) Xe as a function of SiH_4 and Si_2H_6 flow ratio with changing RF power.

of source-gas flow ratio in Si_2H_6 plasma for the RF power ranging from 5 to 50 W. The tendency in the variation of SiH_2 radical density as a function of the parent-gas flow ratio is almost the same with the case of SiH_4. However, the density of SiH_2 radicals for higher parent-gas flow ratio is lower than that in the case of SiH_4. In addition, at higher parent-gas flow ratio, intra-cavity laser oscillation could not be maintained due to scattering of the laser beam by a large amount of particles in the plasma. This suggests that attachment reaction of reactive species to parent Si_2H_6 correlates to particle formation, since this phenomenon appears at higher parent-gas flow ratio. Although the attachment reaction is also regarded to occurs for SiH_4, the laser oscillation are maintained in SiH_4 plasma. This may be due to lower rate constant of the attachment reaction for SiH_4 (1.0×10^{-11} cm^2/s) compared with that for Si_2H_6 (1.2×10^{-10} cm^2/s) [7]. Details are discussed with the aid of simulation.

4.3 Gas-phase reaction simulation

4.3.1 Description of the model

Simulation of gas-phase reactions is based on a numerical solution of the continuity equations for electrons, ions and neutrals coupled with Poisson's equation and reaction rate equations using reported rate constants. Input RF power is set to be 50 mW cm^{-1}, which corresponds to 5 W in the experiments described in the previous section.

As for SiH_4 plasma diluted with He, Ar and Xe (referred to as SiH_4 plasma hereafter), the rates of electron impact ionization, excitation and dissociation of SiH_4 molecules and dilution gas atoms are calculated from swarm parameters with a local field approximation (LFA) [8]. The swarm parameters are obtained by solving the Boltzmann equation with a set of cross section data of SiH_4 [9, 10], He [11], Ar [12], Xe [11], and also H_2 [13], because the density of H_2 increases with the decomposition of SiH_4. Reaction paths and their branching ratios for dissociative reactions have been determined according to Kushner [7] and Yuuki [14]. Diffusion coefficients for the species in the diluted gases are calculated on the basis of Chapman-Enskog theory [15], the value of Lenuard-Jones parameters [7,15] and Blanc's law [16]. The boundary conditions applied in the simulation are set according to Gallagher's formulation [17], where sticking probabilities of monoradicals and other radicals is assumed to be 0.1 and 1.0, respectively.

Tab. 4.1: Electron-impact reactions. α, v_e and n_e is electron impact coefficient, electron drift velocity and electron density, respectively. α and v_e are calculated by solving Boltzmann equation for a given electric field.

No.	Reactants		Products	Rate	Reference(s)
	Ionization, attachment and excitation				
R_1	$SiH_4 + e$	$\rightarrow$	$SiH_3^+ + H + 2e$	$0.4\alpha_i v_e n_e$	[7, 9]
R_2		$\rightarrow$	$SiH_2^+ + H_2 + 2e$	$0.5\alpha_i v_e n_e$	[7, 9]
R_3		$\rightarrow$	$SiH^+H_2 + H + 2e$	$0.1\alpha_i v_e n_e$	[7, 9]
R_4		$\rightarrow$	$SiH_3^- + H$	$0.6\alpha_a v_e n_e$	[7, 9]
R_5		$\rightarrow$	$SiH_2^- + H_2$	$0.4\alpha_a v_e n_e$	[7, 9]
R_6	$H_2 + e$	$\rightarrow$	$H_2^+ + 2e$	$\alpha_i v_e n_e$	[13]
R_7	$He + e$	$\rightarrow$	$He^+ + 2e$	$\alpha_i v_e n_e$	[11]
R_8		$\rightarrow$	$He^* + e$	$\alpha_{ex} v_e n_e$	[11]
R_7	$Ar + e$	$\rightarrow$	$Ar^+ + 2e$	$\alpha_i v_e n_e$	[12]
R_8		$\rightarrow$	$Ar^* + e$	$\alpha_{ex} v_e n_e$	[12]
R_7	$Xe + e$	$\rightarrow$	$Xe^+ + 2e$	$\alpha_i v_e n_e$	[11]
R_8		$\rightarrow$	$Xe^* + e$	$\alpha_{ex} v_e n_e$	[11]
	Cumulative ionization			Rate coefficient	
R_9	$Ar^* + e$	$\rightarrow$	$Ar^+ + 2e$	2.4×10^{-9}	[7]
R_{10}	$Xe^* + e$	$\rightarrow$	$Xe^+ + 2e$	3.0×10^{-7}	[11]

Tab. 4.2: Atom-impact reactions.

No.	Reactants		Products	Rate coefficient	Reference(s)
	Penning ionization				
R_{11}	$He^* + He^*$	$\rightarrow$	$He^+ + He + e$	2.4×10^{-9}	[26]
R_{12}	$Ar^* + Ar^*$	$\rightarrow$	$Ar^+ + Ar + e$	5.0×10^{-10}	[27]
R_{13}	$Xe^* + Xe^*$	$\rightarrow$	$Xe^+ + Xe + e$	5.0×10^{-10}	[28]
	Charge transfer				
R_{14}	$SiH_4 + He^+$	$\rightarrow$	$SiH_2^+ + H_2 + He$	5.0×10^{-10}	[22]
R_{15}		$\rightarrow$	$SiH^+ + H_2 + H + He$	2.4×10^{-9}	[22]
R_{16}		$\rightarrow$	$Si^+ + 2H_2 + He$	1.0×10^{-9}	[22]
R_{17}	$SiH_4 + Ar^+$	$\rightarrow$	$SiH_3^+ + H + Ar$	2.4×10^{-12}	[7, 22]
R_{18}		$\rightarrow$	$SiH_2^+ + H_2 + Ar$	1.7×10^{-12}	[7, 22]
R_{19}		$\rightarrow$	$SiH^+ + H_2 + H + Ar$	4.2×10^{-10}	[7, 22]
R_{20}	$SiH_4 + Xe^+$	$\rightarrow$	$SiH_3^+ + H + Xe$	2.4×10^{-12}	[7, 22]
R_{21}		$\rightarrow$	$SiH_2^+ + H_2 + Xe$	1.7×10^{-12}	[7, 22]
R_{22}		$\rightarrow$	$SiH^+ + H_2 + H + Xe$	4.2×10^{-10}	[7, 22]
	Energy transfer				
R_{23}	$SiH_4 + He^*$	$\rightarrow$	$SiH + H_2 + H + He$	5.9×10^{-14}	[19, 22]
R_{24}		$\rightarrow$	$SiH_n^+ + He + e$	8.0×10^{-13}	[19, 22]
R_{25}	$SiH_4 + Ar^*$	$\rightarrow$	$SiH_3 + H + Ar$	1.4×10^{-10}	[7, 24]
R_{26}		$\rightarrow$	$SiH_2 + 2H_2 + Ar$	2.6×10^{-10}	[7, 24]
R_{27}		$\rightarrow$	$SiH + H_2 + H + Ar$	1.0×10^{-10}	[7, 23]
R_{28}		$\rightarrow$	$Si + 2H_2 + Ar$	1.0×10^{-10}	[7, 23]
R_{29}	$SiH_4 + Xe^*$	$\rightarrow$	$SiH_3 + H + Xe$	1.4×10^{-10}	[7, 21]
R_{30}		$\rightarrow$	$SiH_2 + 2H_2 + Xe$	2.6×10^{-10}	[7, 21]
R_{31}		$\rightarrow$	$SiH + H_2 + H + Xe$	1.0×10^{-10}	[7, 21]
R_{32}		$\rightarrow$	$Si + 2H_2 + Xe$	1.0×10^{-10}	[7, 21]

Tab. 4.3: Reactions including charged and excited species. α, v_e and n_e is electron impact coefficient, electron drift velocity and electron density, respectively. α and v_e are calculated by solving Boltzmann equation for a given electric field.

No.	Reactants		Products	Rate	Reference(s)
	Primary reactions				
R_{33}	$SiH_4 + e$	$\rightarrow$	$SiH_3 + H + e$	$0.830\alpha_{dn}v_e n_e$	[7]
R_{34}		$\rightarrow$	$SiH_2 + H_2 + e$	$0.097\alpha_{dn}v_e n_e$	[7,14]
R_{35}		$\rightarrow$	$SiH + H_2 + H + e$	$0.047\alpha_{dn}v_e n_e$	[7,14]
R_{36}		$\rightarrow$	$Si + 2H_2 + e$	$0.026\alpha_{dn}v_e n_e$	[7,14]
R_{37}	$Si_2H_6 + e$	$\rightarrow$	$SiH_2 + SiH_4 + e$	$1.67\alpha_{dn}v_e n_e$	[14]
R_{38}		$\rightarrow$	$Si_2H_5 + H + e$	$0.71\alpha_{dn}v_e n_e$	[14]
R_{39}	$Si_3H_8 + e$	$\rightarrow$	$SiH_2 + Si_2H_6 + e$	$2.22\alpha_{dn}v_e n_e$	[14]
R_{40}		$\rightarrow$	$SiH_3 + Si_2H_5 + e$	$0.95\alpha_{dn}v_e n_e$	[14]
R_{41}	$Si_4H_{10} + e$	$\rightarrow$	$SiH_2 + Si_3H_8 + e$	$2.22\alpha_{dn}v_e n_e$	[14]
R_{42}		$\rightarrow$	$SiH_3 + Si_3H_7 + e$	$0.95\alpha_{dn}v_e n_e$	[14]
	Secondary reactions			Rate coefficient	
R_{43}	$SiH_4 + H$	$\rightarrow$	$SiH_3 + H_2$	2.67×10^{-12}	[7,14]
R_{44}	$SiH_4 + Si$	$\rightarrow$	$SiH_2 + SiH_2$	5.33×10^{-13}	[7,14]
R_{45}	$SiH_4 + SiH$	$\rightarrow$	Si_2H_5	2.51×10^{-12}	[7,14]
R_{46}	$SiH_4 + SiH_2$	$\rightarrow$	Si_2H_6	1.00×10^{-11}	[7,14]
R_{47}	$SiH_4 + SiH_3$	$\rightarrow$	$Si_2H_5 + H_2$	1.78×10^{-15}	[7,14]
R_{48}	$SiH_4 + Si_2H_5$	$\rightarrow$	$Si_2H_6 + SiH_3$	5.00×10^{-13}	[7,14]
R_{49}	$Si_2H_6 + H$	$\rightarrow$	$SiH_3 + SiH_4$	1.11×10^{-12}	[7,14]
R_{50}	$Si_2H_6 + H$	$\rightarrow$	$Si_2H_5 + H_2$	1.20×10^{-10}	[7,14]
R_{51}	$Si_2H_6 + SiH_2$	$\rightarrow$	Si_3H_8	1.20×10^{-10}	[7,14]
R_{52}	$Si_2H_6 + SiH_3$	$\rightarrow$	$SiH_4 + Si_2H_5$	1.00×10^{-12}	[7,14]
R_{53}	$Si_3H_8 + H$	$\rightarrow$	$SiH_3 + Si_2H_6$	2.16×10^{-12}	[7,14]
R_{54}	$Si_3H_8 + H$	$\rightarrow$	$Si_3H_7 + H_2$	2.16×10^{-12}	[7,14]
R_{55}	$Si_3H_8 + SiH_2$	$\rightarrow$	Si_4H_{10}	1.20×10^{-10}	[7,14]
R_{56}	$Si_3H_8 + SiH_3$	$\rightarrow$	$SiH_4 + Si_3H_7$	2.49×10^{-12}	[7,14]
R_{57}	$Si_3H_8 + Si_2H_5$	$\rightarrow$	$Si_2H_6 + Si_3H_7$	2.49×10^{-12}	[7,14]
R_{58}	$H_2 + Si$	$\rightarrow$	SiH_2	6.58×10^{-12}	[7,14]
R_{59}	$H_2 + SiH$	$\rightarrow$	SiH_3	6.99×10^{-13}	[7,14]
R_{60}	$H_2 + SiH_2$	$\rightarrow$	SiH_4	1.99×10^{-12}	[7,14]
R_{61}	$SiH_3 + SiH_3$	$\rightarrow$	$SiH_2 + SiH_4$	6.99×10^{-12}	[7,14]
R_{62}	$SiH_3 + SiH_3$	$\rightarrow$	Si_2H_6	1.00×10^{-11}	[7,14]
R_{63}	$Si_2H_5 + SiH_3$	$\rightarrow$	Si_3H_8	5.50×10^{-11}	[7,14]
R_{64}	$Si_2H_5 + Si_2H_5$	$\rightarrow$	Si_4H_{10}	1.00×10^{-11}	[7,14]

Ar atoms excited to the metastable states (Ar^*; $^3P_{0,2}$) is known to decompose SiH_4 to produce SiH_2 [2, 7, 18]. Metastable He atoms (He^*; 2^3S) are also known to decompose SiH_4, although they produce ionized species instead of SiH_2 due to high energy of He^* [19, 20]. Metastable Xe atoms (Xe^*; $^3P_2$) are also expected to decompose the silane species [21]. However, the rate coefficients of the reactions between SiH_4 and Xe^* are not reported. Therefore, it is assumed that the rate coefficients and products for the SiH_4-Xe^* reactions are same to those for SiH_4-Ar^* reactions as in Table 4.1 [7, 9–13, 19, 21–28].

For Si_2H_6 plasma diluted with He, Ar and Xe (referred to as Si_2H_6 plasma hereafter), the density of higher silanes Si_nH_{2n+2} ($n \geq 3$) can not be neglected due to frequent attachment of SiH_2 to Si_2H_6 and the higher silanes. The cross-section data of the higher silanes are unknown in my knowledge. In this work, therefore, reactions in Si_2H_6 plasma are calculated using the dissociation rates for Si_2H_6 and higher silanes with the same spatial profile to SiH_4 dissociation rate. Their absolute values are modified according to the relative branching ratios listed in Table 4.3 [14]. Reactions between Si_2H_6 and metastable He^*, Ar^* and Xe^* are not considered in the present simulation because their reaction paths and rate coefficients are unknown. Although precise comparison cannot be performed between SiH_4 and Si_2H_6 plasma due to this ambiguity, the difference in the tendency can be investigated for the two cases.

4.3.2 Density of radicals

Figures 4.6(a) and 4.6(b) show calculated density of SiH_2 in SiH_4 and Si_2H_6 plasma as a function of source-gas flow ratio. Density of SiH_3, Si_2H_5 and Si_3H_7 is also shown in the same figures for comparison. As can be seen in these figures, SiH_2 radical density increases with dilution, which is consistent with our experimental results. To investigate the cause of the increase in SiH_2 radical density with dilution, I have calculated the electron impact dissociation rate of the parent gases and metastables-assisted dissociation rate, which corresponds to SiH_2 production rate. I have calculated also SiH_2 loss rate caused by reactions and diffusion.

In the steady state, the following equation holds for SiH_2 radical density $[SiH_2]$ in SiH_4 plasma;

$$\alpha_{\mathrm{dn}} v_{\mathrm{e}} n_{\mathrm{e}} + k^*[\mathrm{M}^*][\mathrm{SiH_4}] - \sum k_{\mathrm{i}}[\mathrm{SiH_2}][\mathrm{X}] - D\frac{\partial^2[\mathrm{SiH_2}]}{\partial x^2} = 0. \qquad (4.1)$$

The first two terms are SiH_2 production rates for electron impact dissociation

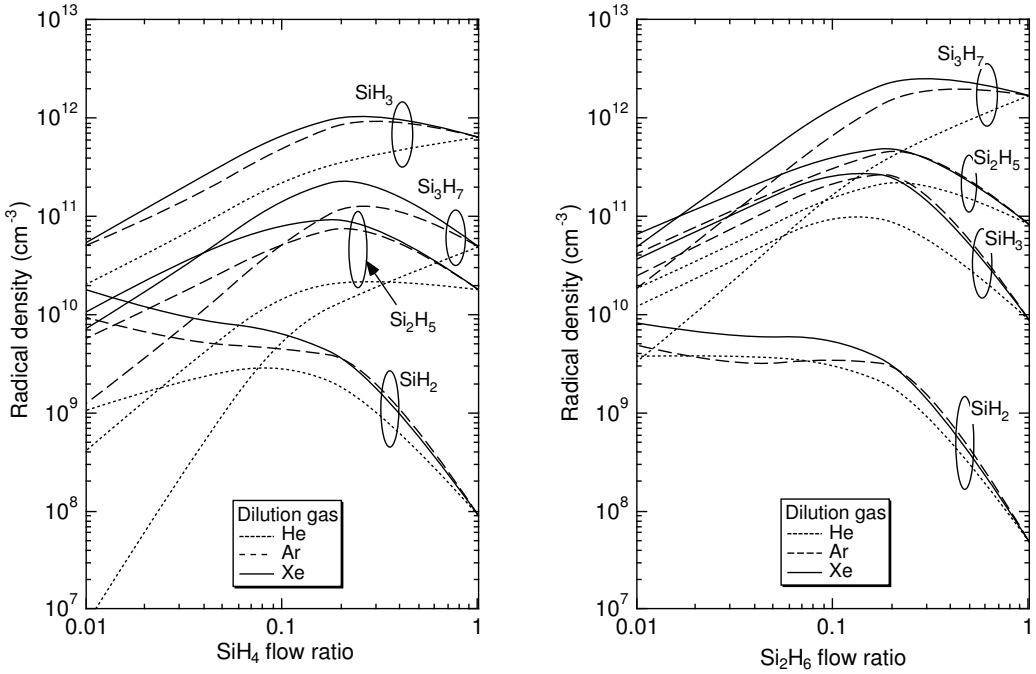

(a) SiH_4 plasmas (b) Si_2H_6 plasmas

Fig. 4.6: Calculated radical density in (a) SiH_4 plasmas and (b) Si_2H_6 plasmas diluted with He, Ar and Xe as a function of source-gas flow ratio at RF power density of 50 mW/cm^2.

and metastables-assisted dissociation for parent-gas molecules, where $\alpha_{\rm dn}$ is the dissociation coefficient, $v_{\rm e}$ is electron drift velocity, $n_{\rm e}$ is electron density, k^* is rate coefficient and M^* means metastable species of He^*, Ar^* and Xe^*. Since the value of $\alpha_{\rm dn}$ changes with the parent-gas density, normalized dissociation rate coefficient;

$$K_{\rm G} = \frac{\alpha_{\rm dn} v_{\rm e} n_{\rm e}}{[{\rm SiH_4}]}, \tag{4.2}$$

is characterized. In order to investigate the contribution of M^*, $K^* = k^*[M^*]$ is calculated. The third and fourth terms are the reaction and diffusion loss rates, where $k_{\rm i}$ and X is rate constant and reactant of the i-th SiH_2 loss reaction, and D is the diffusion coefficient of SiH_2 radical in SiH_4 plasma. Major SiH_2 loss reactions for SiH_4 and Si_2H_6 plasma are

$$\begin{aligned} {\rm SiH_2 + SiH_4} &\rightarrow {\rm Si_2H_6}, & (4.3)\\ {\rm SiH_2 + Si_2H_6} &\rightarrow {\rm Si_3H_8}, & (4.4) \end{aligned}$$

respectively, which account for 70% or more part of total loss reaction rate. Since these terms also change with SiH_2 radical density, normalized ones, i.e.,

$$K_{\rm R} = \sum k_{\rm i}[{\rm X}] \tag{4.5}$$

and

$$K_{\rm D} = \frac{1}{[{\rm SiH_2}]} D \frac{\partial^2 [{\rm SiH_2}]}{\partial x^2} \tag{4.6}$$

are characterized. That is, $K_{\rm G}$, K^*, $K_{\rm R}$ and $K_{\rm D}$ are analyzed in the following equation derived from eq.4.1;

$$[{\rm SiH_2}] = \frac{K_{\rm G} + K*}{K_{\rm R} + K_{\rm D}} [{\rm SiH_4}]. \tag{4.7}$$

Figure 4.7(a) shows the SiH_2 production rate coefficients $K_{\rm G}$ and K^* for SiH_4 plasma. As can be seen in the figure, contribution of electron impact dissociation increases with decrease of SiH_4 flow ratio, in other words, with increase of dilution. The effect of dissociation by metastable species also increases, but its rate coefficient is less than that for electron impact dissociation for SiH_4 flow ratio larger than 0.1. It surpasses the electron impact dissociation for SiH_4 flow ratio less than 0.1. For loss rate coefficients $K_{\rm R}$ and $K_{\rm D}$ in Fig.4.7(b), major loss process is the reaction loss, except for low parent gas flow ratio, and its rate decreases with dilution. Since the major loss reaction of SiH_2 radical is the attachment reaction of

$$\begin{aligned} {\rm SiH_2 + SiH_4} &\rightarrow {\rm Si_2H_6}, & (4.8) \end{aligned}$$

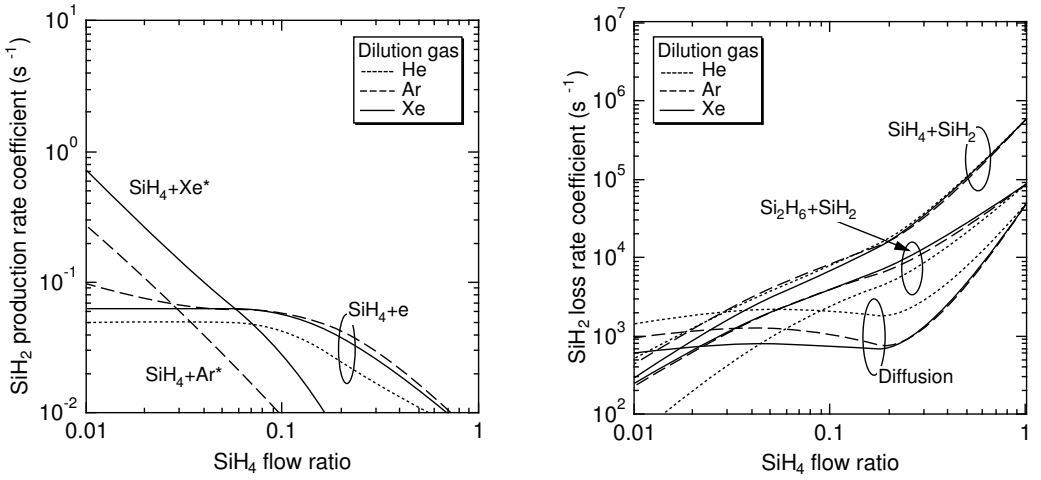

(a) Production rate coefficient (b) Loss rate coefficient

Fig. 4.7: (a) SiH_2 production rate coefficient and (b) SiH_2 loss rate coefficient in SiH_4 plasmas diluted with He, Ar and Xe, calculated as a function of SiH_4 flow ratio at RF power density of 50 mW/cm^2.

the decrease in K_R is mainly due to decrease of $[SiH_4]$ in

$$K_R \sim k[SiH_4]. \tag{4.9}$$

These results mean that the density of SiH_2 radical is mostly determined by K_G/k as can be understood from eq.(4.7). Therefore, the increase of SiH_2 radical density in SiH_4 plasma with dilution is mainly due to increase of dissociation rate of parent SiH_4 molecules, and not due to decrease of SiH_2 loss rates, which is consistent with the results obtained by Kono [18].

Figures 4.8(a) and 4.8(b) shows K_G and $K*$, and K_R and K_D for Si_2H_6 plasma, respectively. The tendency of these parameters obtained for Si_2H_6 plasma is almost same as that for SiH_4 plasma. Therefore, similar arguments to those for SiH_4 plasma hold for Si_2H_6. The higher value of electron impact dissociation rate coefficient for Si_2H_6 is due to its higher branching ratio as shown in Table 4.1, which originates in the higher value of its cross section [29]. Effect of metastable species considered only for the reaction with SiH_4 in Si_2H_6 plasma is almost same to the result for SiH_4 plasma, even though SiH_4 is a relatively minor species in this case. This is due to higher density of metastable species, since I do not consider their major loss processes of the reaction with the parent Si_2H_6 molecules. Although SiH_2 production rate for Si_2H_6 plasma is higher than that for SiH_4 plasma, measured and calculated densities of SiH_2

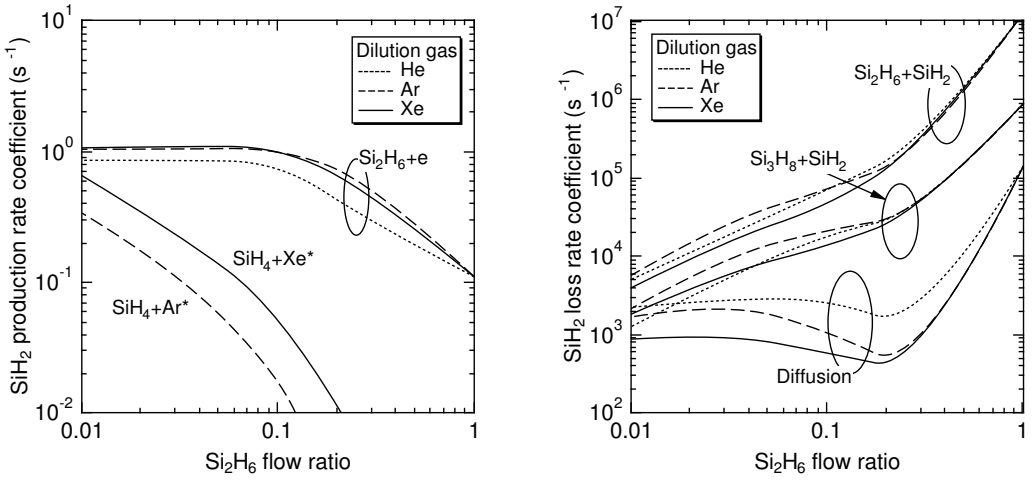

(a) Production rate coefficient (b) Loss rate coefficient

Fig. 4.8: (a) SiH_2 production rate coefficient and (b) SiH_2 loss rate coefficient in Si_2H_6 plasmas diluted with He, Ar and Xe, calculated as a function of Si_2H_6 flow ratio at RF power density of 50 mW/cm^2.

do not show marked difference. This is due to higher reaction loss rate of SiH_2 as shown in Fig.4.8(b), which is due to higher rate coefficient for the major loss reaction SiH_2 + Si_2H_6 in comparison to SiH_2 + SiH_4 in SiH_4 plasma as listed in Table 4.1. For this reason, the diffusion loss process in this case does not contribute as in the case of SiH_4 plasma.

4.3.3 Plasma parameters

From the results obtained in the previous section, the increase in SiH_2 is concluded to be due to increase in dissociation rate coefficient of parent molecules for both SiH_4 and Si_2H_6 plasma. As I could not perform *ab initio* calculation for Si_2H_6 plasma to obtain swarm parameters, I investigated only SiH_4 plasma in detail. The increase in the dissociation rate is attributed to the increase in all of $\alpha_{\rm dn}/[SiH_4]$, $v_{\rm e}$ and $n_{\rm e}$. The values of these parameters at the position where the rate is maximum are shown in Fig.4.9 as a function of SiH_4 flow ratio.

In the case of He dilution, $n_{\rm e}$ shows the lowest value due to small ionization cross section of He [11], and does not change very much from the value for pure SiH_4 plasma, in which $n_{\rm e}$ is suppressed to a low value due to negative ion formation by electron attachment to SiH_4 [30]. On the other hand, $\alpha_{\rm dn}$ and

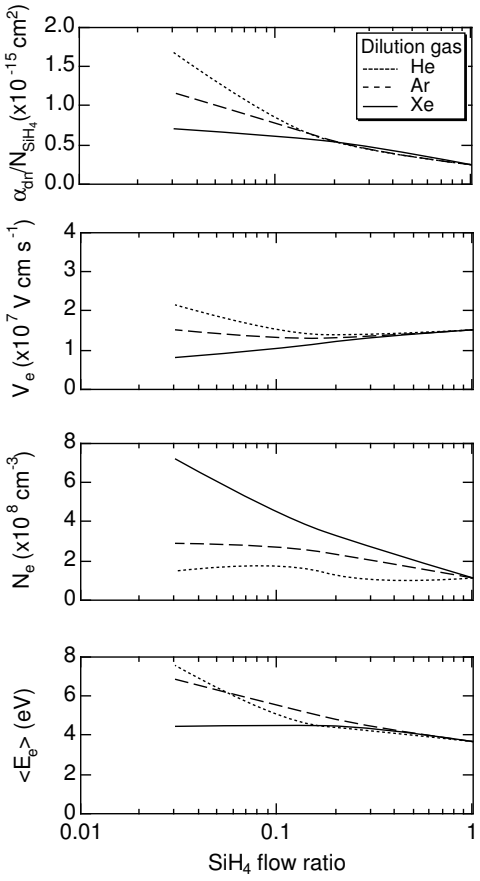

Fig. 4.9: Dissociation rate coefficient $\alpha_{\rm dn}/[SiH_4]$, electron drift velocity $v_{\rm e}$, electron density $n_{\rm e}$ and mean electron energy $< E_{\rm e} >$ calculated in He-, Ar- and Xe-diluted SiH_4 plasmas as a function of SiH_4 flow ratio.

v_e increase due to increase of electron energy because of the lowest total cross section at high energy (>10 eV) and the highest threshold energy (∼20 eV) of the cross section [11]. Therefore, we can conclude that the increase of SiH_2 radical density with He dilution is caused by the increase of electron impact dissociation rate due to increase of electron energy.

In the case of Xe dilution, on the other hand, v_e decreases due to decrease of electron energy caused by higher total cross section and the lowest threshold energy (∼10 eV) of the cross section [11], and α_{dn} also does not increase as in the case of He dilution. Instead, n_e increases due to the highest ionization cross section and the lowest threshold energy of ionization of Xe [11]. Therefore, we can conclude that the increase of SiH_2 radical density with Xe dilution is caused by the increase of electron impact dissociation rate due to increase of electron density.

In the case of Ar dilution, n_e, α_{dn} and v_e show moderate values between those for the case of He and Xe dilution. This is because the cross-section value and its threshold energy of Ar show corresponding moderate values [12]. Therefore, the increase in both of the electron energy and density contributes to the increase of SiH_2 radical density in the case of Ar dilution.

4.3.4 Deposition rate

To investigate the correlation between the film deposition and radical composition, a-Si:H films has been deposited on c-Si(111) substrates with different source-gas flow ratio at RF power of 5 W.

First, quantitative contribution of SiH_2 radicals to the film deposition is investigated. Figure 4.10(a) shows the measured deposition rate as a function of source-gas flow ratio. As can be seen in the figure, the deposition rate basically increases with increase of source-gas concentration even though SiH_2 radical density rapidly decreases as shown in Fig.4.5. This result suggests that SiH_2 does not contribute to the film deposition. To investigate the composition of deposited radicals, deposition rates for SiH_4 and Si_2H_6 plasma are calculated from radical flux onto the surface.

Figure 4.10(b) shows the deposition rate calculated from deposition radical flux, which show good agreement with the experimental results. Contribution ratio of radicals in the deposition rate for SiH_4 and Si_2H_6 plasma is shown in Figs.4.11(a) and 4.11(b), respectively. The main deposition precursor in SiH_4 plasma is SiH_3, while those in Si_2H_6 plasma are Si_3H_7 and Si_2H_5. The

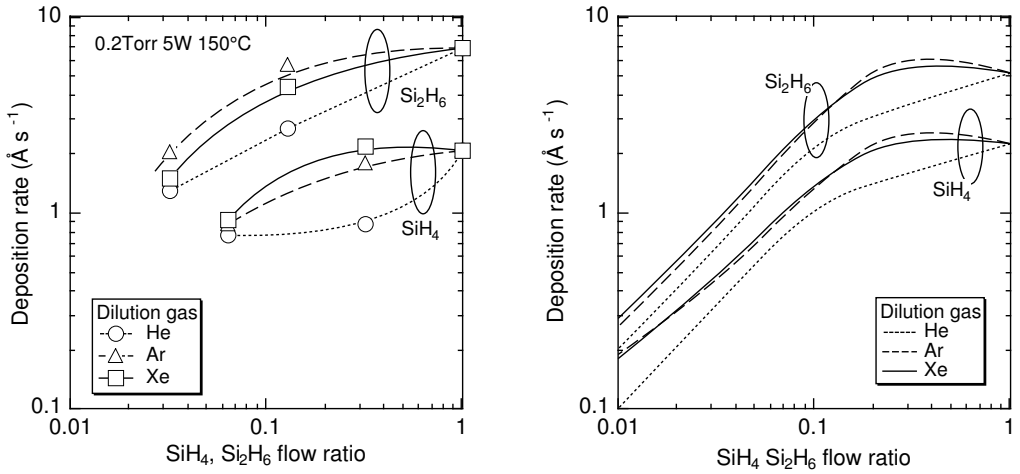

(a) Measured (b) Calculated

Fig. 4.10: (a) Measured and (b) calculated deposition rate of a-Si:H thin films deposited with SiH_4 and Si_2H_6 plasmas diluted with He, Ar and Xe as a function of SiH_4 and Si_2H_6 flow ratios.

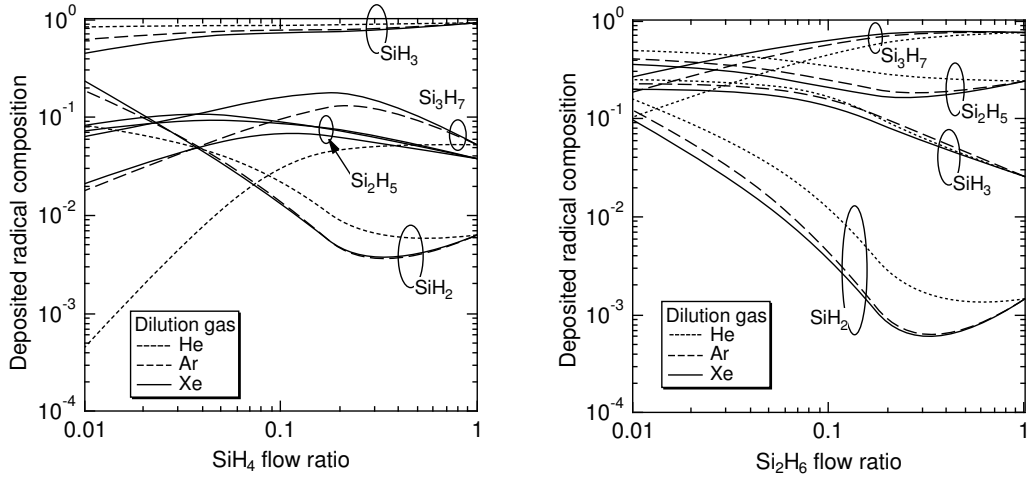

(a) SiH_4 plasmas (b) Si_2H_6 plasmas

Fig. 4.11: Calculated deposited radical composition in (a) SiH_4 and (b) Si_2H_6 plasmas diluted with He, Ar and Xe as a function of SiH_4 and Si_2H_6 flow ratios.

contribution of Si_3H_7 in Si_2H_6 plasma is due to electron impact dissociation of Si_4H_{10} produced by frequent attachment reaction of SiH_2 with Si_2H_6 and Si_3H_8. For both SiH_4 and Si_2H_6 plasma, contribution of SiH_2 is smaller than those of these main precursors, although it increases with dilution. From these results, it is concluded that contribution of SiH_2 radicals to the film deposition is fairly low compared with the major radicals. However, SiH_2 radicals are considered to affect the quality of deposited films, because it has high reactivity both on the surface and in the gas phase, which modifies surface reactions directly and/or indirectly through changing the gas phase radical composition as indicated by production of higher radicals. Effects of SiH_2 radicals on deposited films are investigated in the following section.

4.4 Surface reaction simulation

In the previous section, contribution of SiH_2 to film deposition has been predicted to be low from the view point of only the quantity of deposition precursors. Since the film deposition proceeds through chemical reactions on growing film surface, we must take chemical reactivity of the precursors into account. In this section, therefore, surface reaction simulation is performed in order to investigate effects of SiH_2 radicals on film growth. For the purpose of taking surface migration into account, three-dimensional particle model has been newly developed using a Monte-Carlo method, which is similar to the model proposed by McCaughey *et al.* [27].

4.4.1 Description of the model

In my particle model using a Monte-Carlo method, the surface area of 75×75 Å square is considered, where one side of the square is divided into 30 lattice points. The site density of 1.6×10^{15} cm^2 is close to the atomic density of a crystal silicon (100) surface (1.35×10^{15} cm^2). The total number of deposited radicals is 40000. Radical species considered are SiH_3, SiH_2 and H, and surface reactions used are the same as those in chapter 3.

SiH_3 deposits only on a site with a dangling bond, while SiH_2 deposits even on a H-saturated site. The dangling bond is created through H-abstraction from a H-saturated site by SiH_3 or H, and also through the deposition of SiH_2. The excess hydrogen is eliminated through cross-linking between the sites.

Surface migration of SiH_3 is considered in my new model, which occurs

Tab. 4.4: Radical flux density (cm^{-2} s^{-1}) and the ratio $\Phi(SiH_2)/\Phi(SiH_2)$.

	$\Phi(SiH_2)$	$\Phi(SiH_3)$	$\Phi(H)$	$\Phi(SiH_2)/\Phi(SiH_3)$
(a)	2.8×10^{12}	9.6×10^{14}	8.0×10^{14}	0.003
(b)	2.6×10^{12}	1.0×10^{13}	2.3×10^{13}	0.3

toward the valley site nearby, while that of SiH_2 is not allowed because of its high sticking probability of 1.0 as generally assumed [31]. The migration frequency is given by

$$f_{\mathrm{m}} = f_0 \exp\left(-\frac{E_{\mathrm{act}}}{kT_{\mathrm{sub}}}\right), \tag{4.10}$$

where E_{act} is the activation energy for migration, k is the Boltzmann constant and T_{s} is the substrate temperature (373K). The value of the pre-exponential factor f_0 is taken as 10^5 s^{-1} and E_{act} as 0.2 eV [32]. The radical fluxes Φ(X) are listed in Table 4.4 as (a) and (b) which have been obtained from the gas-phase simulation of 100% SiH_4 plasma and 1% SiH_4 plasma diluted with Ar, respectively. $\Phi(SiH_2)/\Phi(SiH_3)$ tends to increase with Ar dilution, which is consistent with reported experimental results [1, 33].

4.4.2 Simulation results

Figures 4.12(a) and 4.12(b) show the simulation results on the surface microstructure of deposited films. The thickness of the deposited films is about 100Å. C_{H}, N(Si-H_2)/N(Si-H) and average roughness R_{av} are also shown in these figures. R_{av} is defined as a mean value of the absolute deviation of the height of each site from the average thickness. The results show that surface roughness increases with increase of $\Phi(SiH_2)/\Phi(SiH_3)$. C_{H} and N(Si-H_2)/N(Si-H) also increase at the same time, which is consistent with the results presented in chapter 3 by using a qualitative model and experimental results. These are explained by the following mechanisms. SiH_3 migrates and fills the vacant valley site, which enhances smoothing. On the other hand, SiH_2 sticks on any site without migration, which results in the growth of a rough surface. The sites in the smooth surface stand side by side and interconnect easily, while those on the rough surface do not, due to lack of neighboring sites in contact.

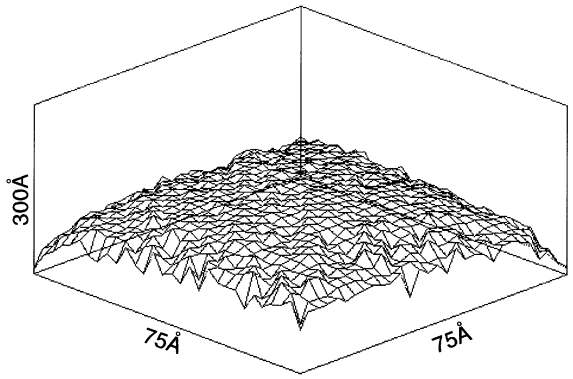

(a) $\Phi(SiH_2)/\Phi(SiH_3)$=0.003,
R_{av}=21Å, C_H=5.6at.%, N(Si-H_2)/N(Si-H)=0.003.

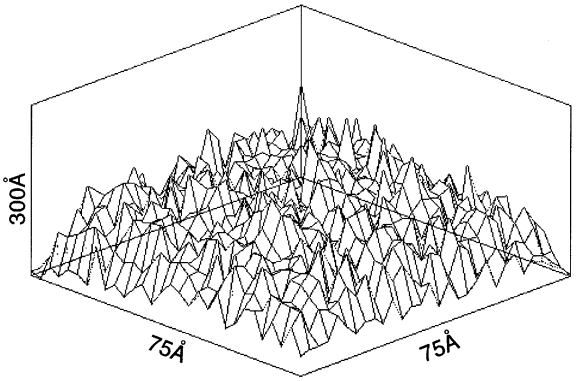

(b) $\Phi(SiH_2)/\Phi(SiH_3)$=0.3,
R_{av}=34Å, C_H=21at.%, N(Si-H_2)/N(Si-H)=0.85.

Fig. 4.12: Surface morphology, hydrogen concentration C_H, hydrogen bonding configuration N(Si-H_2)/N(Si-H) and averaged roughness R_{av} for two radical flux ratios $\Phi(SiH_2)/\Phi(SiH_3)$ of (a) 0.003 and (b) 0.3.

4.5 In situ surface observation

4.5.1 Ellipsometry

In order to check the validity of the model, the microstructure of the growing film surface has been observed by *in situ* ellipsometry. The measurements have been carried out under the two different conditions of low and high values of $\Phi(SiH_2)/\Phi(SiH_3)$, by using the plasma of 100% SiH_4 and that of 2% SiH_4 diluted with Ar, respectively. Values of $\Phi(SiH_2)/\Phi(SiH_3)$ expected from the gas-phase simulation under these conditions are 0.003 and 0.3, respectively. Although the Ar-dilution rate (2%) in this experiment is slightly different from that (1%) in the simulation, the tendency of higher $\Phi(SiH_2)/\Phi(SiH_3)$ is maintained. The substrate is Corning 7059 glass (refractive index $1.53-i0.00$), of which the back surface is roughened to prevent reflection, and T_{sub} has been kept at 100°C (373K). Ellipsometric monitoring has been performed at an incidence angle of 71.8° and at a wavelength of 380 nm.

4.5.2 Experimental results

Results of the trajectories of $\tan\Psi$ and $\cos\Delta$ are shown in Figs.4.13(a) and 4.13(b) as open circles, where $\tan\Psi$ and $\cos\Delta$ are ellipsometric parameters corresponding to the amplitude reflectance ratio and phase difference of p and s polarizing components, respectively [34]. First, I have applied the model of single-layer uniform growth to explain these results. The complex refractive indices of the film are determined from the converged point of the trajectory to be $4.31-i2.48$ and $3.09-i1.98$ for the cases of 100% and 2% SiH_4, respectively. However, the model is not applicable as shown in Figs.4.13(a) and 4.13(b) by dotted lines. This means that the film properties change with the increase of thickness. Then, to take the surface roughness into account, I have applied the two-layer model in which the top layer of the film includes voids. The proportion of the top-layer thickness to the total thickness and volumetric fraction of the voids in the top layer have been parametrically changed. The trajectories calculated with various combinations of these parameters have been compared with the experimental results. For the complex refractive index of the dense a-Si component, I have used the data of Aspnes *et al.* [35]. Film growth models which explain the experimental results successfully are shown in Figs.4.13(c) and 4.13(d), and the trajectories calculated from these models

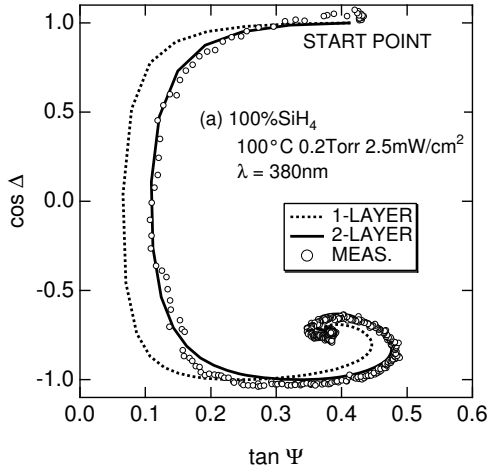

(a) 100% SiH_4

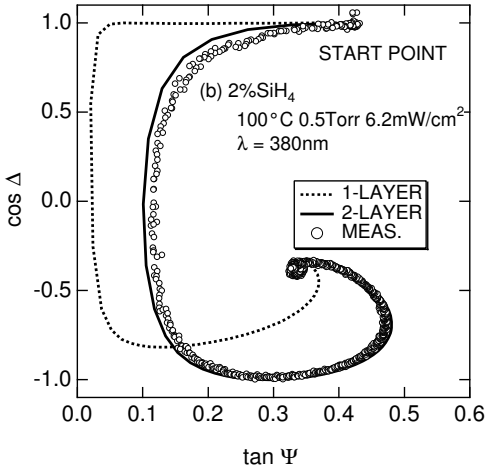

(b) 2% SiH_4/Ar

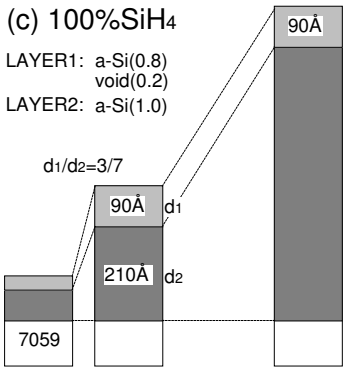

(c) Growth with thin roughness

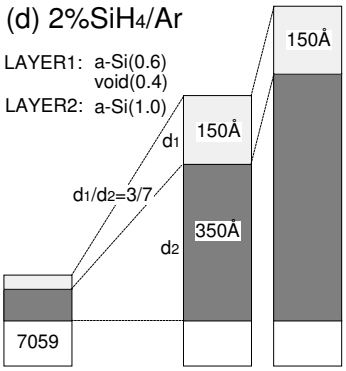

(d) Growth with thick roughness

Fig. 4.13: Trajectories of $\tan\Psi$ and $\cos\Delta$ for the films deposited on Corning 7059 glass ($n = 1.53$) using (a) 100% SiH_4 and (b) 2% SiH_4/Ar plasma. Open circles indicate the experimental results. Dotted lines represent the trajectories calculated using uniform-growth model using the refractive indices obtained from the converged points. Solid line represent those calculated with the growth model shown in (c) and (d), in which d_1 and d_2 denote thickness of the top layer with voids and that of the dense layer beneath the top layer.

are shown in Figs.4.13(a) and 4.13(b) by solid lines. As seen in Figs.4.13(c) and 4.13(d), there exists a top layer with voids which occupies 30% of the total thickness in the initial stage of growth, and a denser region exists under the top layer. The growth of the top layer stops at a certain thickness, and only the dense region grows after that. The maximum thickness and the volumetric fraction of the voids in the top layer are 90 and 0.2, and 150 and 0.4 for the cases of 100% and 2% SiH_4 concentrations, respectively. The greater thickness and void concentration of the top layer for the latter case suggest that the growing film surface is roughened. This result supports the simulated results shown already in Fig.4.12.

4.6 Summary

In conclusion, SiH_2 radical density has been measured in SiH_4 and Si_2H_6 plasma diluted with rare gases of He, Ar and Xe. The density of SiH_2 radical increases with dilution. This is explained by increase in dissociation rate of parent-gas molecules. Its main cause is increase of electron energy as for He dilution, while that is increase of electron density as for Xe dilution. In case of Ar dilution, both of them contribute to the increase in the dissociation rate.

The deposition rate of a-Si:H films decreases with dilution, even though the density of SiH_2 increases. This means that SiH_2 radical does not contribute so much to the film deposition as long as concerning its quantitative contribution, which has been confirmed by low SiH_2 flux compared with main precursors shown in simulation.

However, there is a fact that density of Si-H_2 bonds relative to Si-H bonds increases with the dilution. This means that the contribution of SiH_2 radical brings about Si-H_2 bonds in the films. The cause of this phenomenon has been revealed by performing a Monte-Carlo surface simulation and *in situ* ellipsometric surface monitoring. The results of the simulation have predicted that SiH_2 radicals with higher sticking probability than SiH_3 radicals results in rough surface, and that the roughness causes a lower rate of the cross-linking reactions which eliminate Si-H_2 bonds. The surface roughness formation has been verified using *in situ* ellipsometric monitoring of the growth of the growing film surface.

References

[1] K. Tachibana: Mater. Sci. Eng. **B17** (1993) 68.

[2] K. Tachibana, T. Shirafuji and Y. Matsui: Jpn. J. Appl. Phys. **31** (1992) 2588.

[3] N. Itabashi, K. Kato, N. Nishiwaki, T. Goto, C. Yamada and E. Hirota: Jpn. J. Appl. Phys. **27** (1988) L1565.

[4] I. Dubios: Can. J. Phys. **46** (1968) 2485.

[5] J. W. Thoman, Jr. and J. I. Steinfeld: J. Chem. Phys. **86** (1987) 5909.

[6] J. J. O'Brien and G. H. Atkinson: J. Chem. Phys. **92** (1988) 5782.

[7] M. J. Kushner: J. Appl. Phys. **63** (1988) 2532.

[8] J. -P. Boeuf: Phys. Rev. A **36** (1987) 2782.

[9] M. Kurachi and Y. Nakamura: J. Phys. D **22** (1989) 107.

[10] M. Kurachi and Y. Nakamura: IEEE Trans. Plasma Sci. **19** (1991) 262.

[11] K. Takahashi and K. Tachibana: Trans. IEE Jpn. **111-A** (1991) 3 [in Japanese].

[12] K. Tachibana: Phys. Rev. A **34** (1986) 1007.

[13] S. J. Buckman and A. V. Phelps: *Tabulations of Collision Cross Sections and Calculated Transport and Reaction Coefficients for Electrons in H_2 and D_2* (Univ. of Colorado, Boulder, Colorado, 1985) JILA Data Center Report No.27.

[14] A. Yuuki, T. Kawahara, Y. Matsui and K. Tachibana: Kagaku Kogaku Ronbunshu **17** (1991) 758 [in Japanese].

[15] J. O. Hirschfelder, C. F. Curtiss and R. B. Bird: *Molecular Theory of Gases and Liquids* (Wiley, New York, 1967).

[16] D. R. Bates: *Atomic and Molecular Processes* (Academic Press, New York, 1962).

[17] A. Gallagher: J. Appl. Phys. **63** (1988) 2406.

[18] A. Kono, N. Koike, H. Nomura and T. Goto: Jpn. J. Appl. Phys. **34** (1995) 307.

[19] M. Tsuji, K. Kobarai, S. Yamaguchi and Y. Nishimura: Chem. Phys. Lett. **158** (1989) 470.

[20] H. Yoshida, Y. Morishima, M. Ukai, K. Shinsaka and Y. Hatano: Chem. Phys. Lett. **176** (1991) 173.

[21] J. Balamuta, M. F. Golde and Y. -S. Ho: J. Chem. Phys. **79** (1983) 2822.

[22] H. Catham, D. Hils, R. Robertson and A. C. Gallagher: J. Chem. Phys. **79** (1983) 1301.

[23] M. Tsuji, K. Kobarai, S. Yamaguchi, H. Obase, K. Yamaguchi and Y. Nishimura: Chem. Phys. Lett. **155** (1989) 481.

[24] Y. Toyoshima, K. Kumata, U. Itoh, K. Arai, A. Matsuda, N. Washida, G. Inoue and K. Katsuumi: Appl. Phys. Lett. **46** (1985) 584.

[25] D. J. Eckstrom, H. H. Nakano, D. C. Lorents, T. Rothem, J. A. Betts, M. E. Lainhard, D. A. Dakin and J. E. Maenchen: J. Appl. Phys. **64** (1988) 15.

[26] A. W. Johnson and J. B. Gerardo: Phys. Rev. A **7** (1973) 925.

[27] M. J. McCaughey and M. J. Kushner: J. Appl. Phys. **69** (1991) 6952.

[28] J. A. Levin, S. E. Moody, E. L. Klosterman, R. E. Center and J. J. Ewing: IEEE J. Quantum Electron. **17** (1981) 2282.

[29] Y. Nakamura: *Proc. 10th Symp. Plasma Processing*, Osaka, 1992 (Japan Society of Applied Physics, Tokyo, 1992) p.325.

[30] T. Makabe, F. Tochikubo and M. Nishimura: Phys. Rev. A **42** (1990) 3674.

[31] A. Yuuki, Y. Matsui and K. Tachibana: Jpn. J. Appl. Phys. **28** (1989) 212.

[32] M. J. Kushner: J. Appl. Phys. **62** (1987) 4763.

[33] K. Tachibana, A. Yuuki and Y. Matsui: *Gaseous Electronics and Its Applications,* Ed. R. W. Crompton, M. Hayashi, D. E. Boy and T. Makabe (Kluwer Academic, Dordrecht, 1991) p.273.

[34] R. M. A. Azzam and N. W Bashara: *Ellipsometry and Polarized Light* (Elsevier Science, Amsterdam, 1989).

[35] D. E. Aspnes, A. A. Studna and E. Kinsbron: Phys. Rev. B **29** (1984) 768.

Chapter 5

Reaction kinetics in plasma-enhanced chemical vapor deposition of poly-Si

5.1 Introduction

SiH_4 plasmas with a certain condition prepare silicon thin films containing crystalline part at low temperature less than 300°C. Highly H_2-diluted SiH_4 plasma can deposit microcrystalline silicon thin films with grain size of a few nm, and its deposition rate is as low as 0.2 nm/s [1,2]. Crystalline orientation is mostly <110>. Addition of SiF_4 to the SiH_4 or SiH_4/H_2 system improves the crystallinity from microcrystalline to polycrystalline with grain size of 100–300 nm [3,4]. Crystalline orientation is mostly <110>, and its deposition rate is as high as 1.0 nm/s. Single crystalline silicon thin films also can be epitaxially grown on c-Si substrate at temperature of 400°C by a novel methods using atomic hydrogen [5]. These deposition techniques have attracted much attention because of their low substrate temperature of about 300°C in comparison to conventional solid-phase crystallization of a-Si films at 500–600°C [6]. This can realize the preparation of poly-Si thin-film transistors, for liquid crystalline display panels, on cheap glass substrates instead of expensive quartz ones [4].

In spite of this attractive features, however, their deposition mechanisms have not been fully understood as yet. This is due to the fact that there are no explicit model for explaining deposition process supported by *in situ* diagnostics and simulation as in the deposition of a-Si:H with SiH_4 plasma. In this chapter, *in situ* diagnostics and simulation techniques, as demonstrated in the previous chapters, are applied to $SiF_4/SiH_4/H_2$ system in order to investigate the roles of radicals generated from SiH_4, SiF_4 and H_2 for the first step of

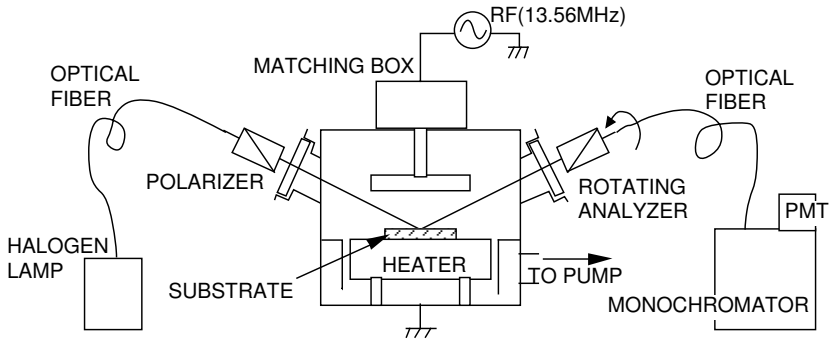

Fig. 5.1: Schematic diagram of plasma CVD reactor with ellipsometric monitoring system.

development of the model.

5.2 Film deposition with $SiF_4/SiH_4/H_2$

5.2.1 Experimental

The deposition of films and *in situ* monitoring of the film growth are carried out using a capacitively coupled radio frequency (RF,13.56 MHz) plasma chemical vapor deposition (CVD) reactor equipped with a built-in ellipsometric monitoring system, as shown in Fig.5.1. The diameter of parallel-plate electrodes is 16 cm and the electrode gap is 3 cm. Corning 7059 glass plates (refractive index of 1.53) are used as the substrates, the back-surface of which is roughened to prevent reflection.

The monitoring of the film growth has been carried out with both monochromatic ellipsometry (ME) and spectroscopic ellipsometry (SE) by using a rotating analyzer method [7]. The ME monitoring is done at the wavelength of 380 nm. The SE monitoring is done in the wavelength range of 350–650 nm with a step of 3 nm. Data over 5 rotating cycles (1.7 Hz) are averaged at each step. The incidence angle is set at 73.6°, the precise value of which is determined from the results of an SE measurement on a crystalline silicon wafer with native oxide. Time-resolved ME trajectory are obtained by performing monitoring during film growth. Time-resolved SE spectra are obtained by repeating the deposition and the SE measurement sequentially. The deposition period is varied in the range from 50 to 500 s according to the change in SE spectra. During the SE measurement period of 5 min, the discharge is turned off to avoid background emission from the plasma and progression of the deposition.

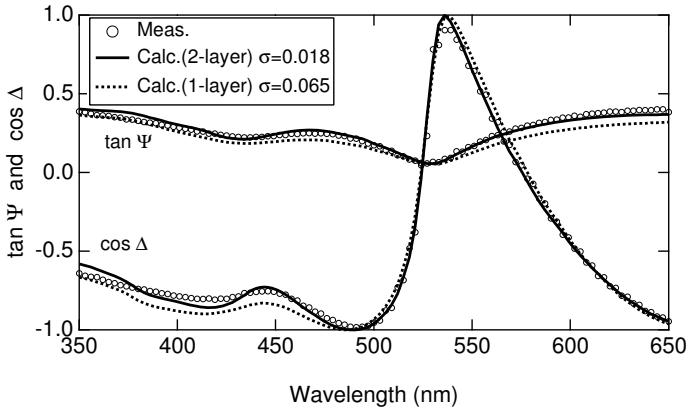

Fig. 5.2: An example of $\tan\Psi$ and $\cos\Delta$ spectra measured for the films deposited with SiF_4 flow ratio of 0.5 (open circles). Solid lines and dotted lines are calculated values with two-layer and one-layer models, respectively. σ denotes the value of mean square deviation between measured and calculated spectra.

The measured trajectory is analyzed by comparing to theoretical one calculated on the basis of a film growth model. A measured spectrum is converted to film composition and thickness with the aid of linear regression analysis [8] and Bruggeman's effective medium approximation [9]. Films are assumed to be composed of a-Si, c-Si and voids. The complex dielectric function for c-Si at 300°C used here is taken from the report of Jellison and Modine [11]. That for a-Si is determined from an SE measurement of a-Si film at 300°C, which has been prepared by a low pressure CVD (LP-CVD) method from the thermal decomposition of Si_2H_6 at 480°C. Actually, the dielectric function of the LP-CVD film measured at room temperature shows good agreement with a reported one [12]. Roughened top layer including a large amount of voids (50% unless otherwise noted) is also assumed to be over a bulk layer. The surface roughness, which may be caused by etching presumably by F atoms, is effectively taken into the void composition. The rest of the top layer may be composed of a-Si or c-Si. Whichever it might be, however, the analyzed result does not change markedly because of the large fraction of voids and small thickness of the layer. Validity of this two-layer model is confirmed by the reduction in the mean square deviation of a calculated spectrum from a measured one. Figure 5.2 shows an example of the spectra of $\cos\Delta$ and $\tan\Psi$. It can be seen that the deviation increases if the presence of the top layer is not assumed. It is also understood that surface roughness increases $\cos\Delta$ value in shorter wavelength region.

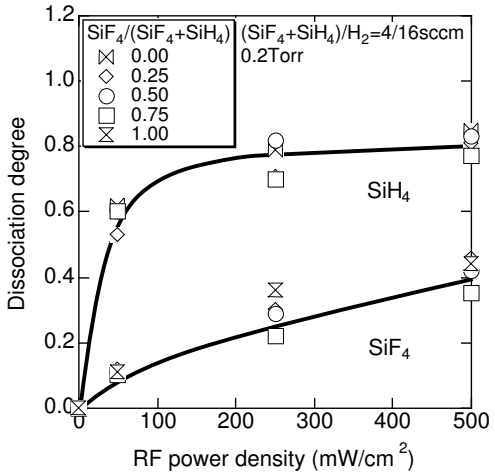

Fig. 5.3: RF power dependence of dissociation degree of SiH_4 and SiF_4 measured under various SiF_4 flow ratio (SiF_4/(SiF_4+SiH_4)).

5.2.2 RF power and substrate temperature dependence

Prior to film deposition, dissociation degree of source gases has been measured by using a mass analysis to investigate the effective contribution of SiF_4 in $SiF_4/SiH_4/H_2$ plasma with various SiF_4/(SiF_4+SiH_4) flow ratios. Although the dissociation degree of SiF_4 is lower than SiH_4, it increases monotonously up to 40% with increasing RF power density while that of SiH_4 saturates at 80% as shown in Fig.5.3. This result means that contribution of $SiF_n (n \leq 3)$ and F relative to $SiH_n (n \leq 3)$ and H increases with increasing RF power density.

Figure 5.4(a) shows measured trajectories of $\tan\Psi$ and $\cos\Delta$ during the film growth with SiF_4 flow ratio of 0.5, and Fig.5.4(b) shows calculated one. The initial stage of the trajectory does not change at low substrate temperature (T_{sub}) of 250°C even if RF power density increases from 50 to 500 mW/cm^2, and is almost the same as the calculated trajectory of a-Si growth shown in Fig.5.4(b). However, the trajectory rotates with a larger diameter circle around the converging point for higher RF power density, which is caused by the multiple reflection interference due to higher transparency of the film. As the absorption coefficient of c-Si is smaller than a-Si at the measurement wavelength of 380 nm, this result implies increase of c-Si fraction during the growth. This can be simulated by the dashed curve in Fig.5.4(b) as calculated assuming gradual increase of c-Si fraction up to 50%. Therefore, it can be concluded that c-Si fraction increases by addition of SiF_4, but its effects is

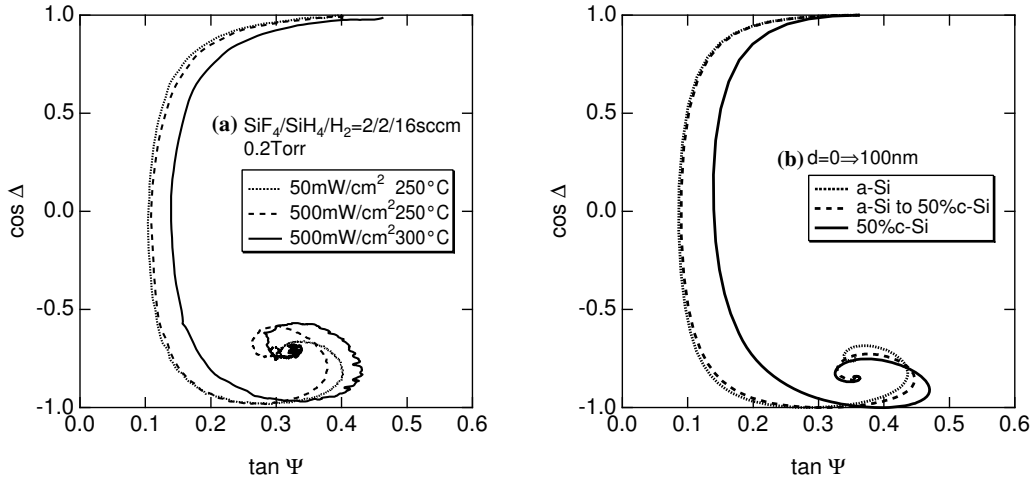

Fig. 5.4: (a) Measured and (b) calculated trajectories of $\tan\Psi$ and $\cos\Delta$.

smaller at lower $T_{\rm sub}$. The higher $\cos\Delta$ value around the converged point in the experimental results is attributed to the surface roughness as mentioned in the previous section. The trajectory shifts to higher $\tan\Psi$ values by increasing $T_{\rm sub}$ to 300°C. This means inclusion of higher fraction of c-Si from the initial stage as seen in the solid curve in Fig.5.4(b). Larger c-Si fraction at higher $T_{\rm sub}$ is due to enhancement of the migration of depositing precursors, which in turn stimulates nucleation [2]. In the following, therefore, the deposition are carried out at $T_{\rm sub}$ of 300°C and RF power density of 500 mW/cm^2 expecting the enhancement of nucleation and the larger effect of SiF_4 addition.

5.2.3 SiF_4/SiH_4 flow ratio dependence

Figures 5.5(a) and 5.5(b) show the time dependence of the growth of the top layer and the bulk layer thickness for different SiF_4 flow ratios, respectively. The thickness of the roughened top layer increases with the deposition time at the beginning, and it becomes almost constant later. The saturated thickness of the top layer becomes larger with increase of the SiF_4 flow ratio. This result suggests that etching of the growing surface occurs by radicals generated from SiF_4, which tends to roughen the surface. The growth rate of the bulk layer decreases from 0.096 to 0.033 nm/s with increase of the SiF_4 flow ratio from 0 to 0.75. In the case of the highest SiF_4 flow ratio, the film starts to grow with a delay time of about 300 s. These results also suggest that deposited precursors are etched out, and nucleation for the film growth is delayed. To confirm the

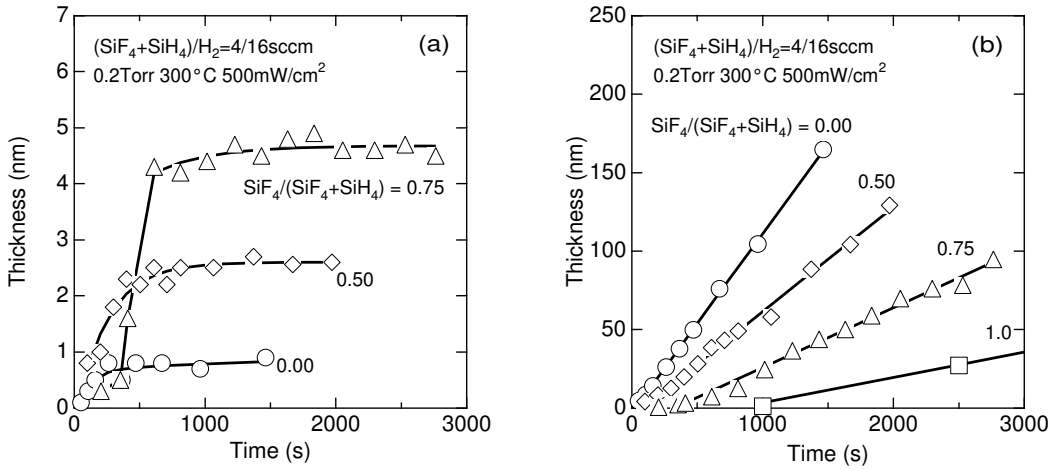

Fig. 5.5: Deposition time dependence of the thickness of surface roughness layer(a) and bulk layer(b) beneath it for different conditions of SiF_4 flow ratio.

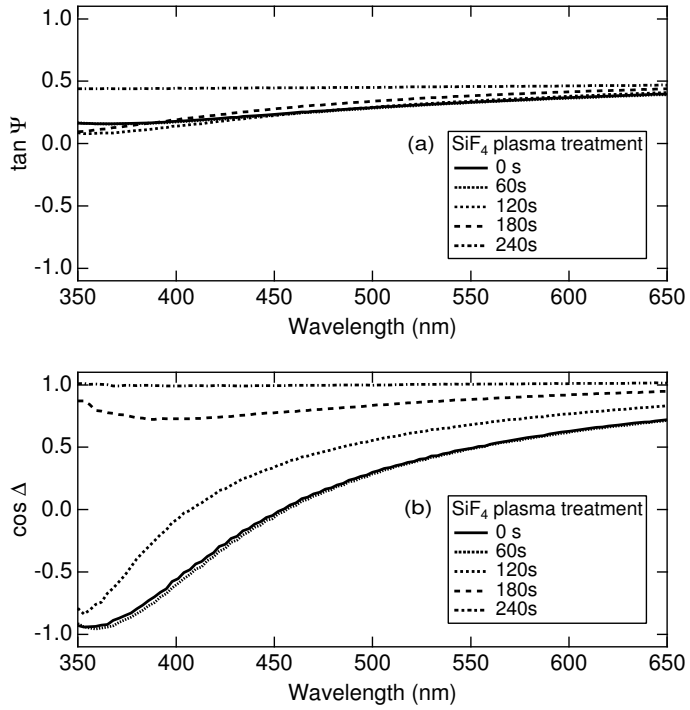

Fig. 5.6: Change in $\tan\Psi$ and $\cos\Delta$ spectra of a deposited film in the treatment with SiF_4 plasma.

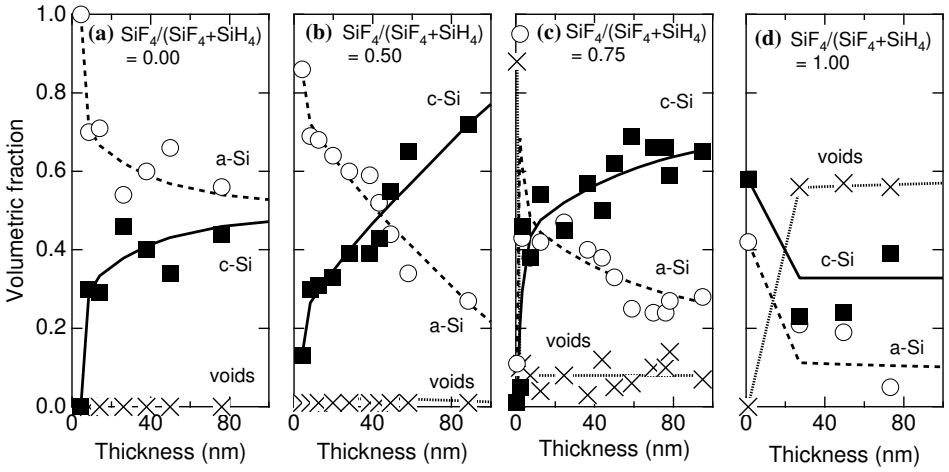

Fig. 5.7: Film compositions estimated from spectroscopic ellipsometry spectra as a function of film thickness for SiF_4 flow ratios of (a) 0.00, (b) 0.50 and (c) 0.75.

mechanism, a deposited film has been treated with pure SiF_4 plasma and measured the changes in $\cos\Delta$ spectra as shown in Fig.5.6. The film has been prepared at the SiF_4 flow ratio of 0.5, and the treatment has been carried out under pure SiF_4 flow of 4 sccm, where the pressure and the RF power density have been set at 0.04 Torr and 500 mW/cm^2, respectively. As seen in this figure, the $\cos\Delta$ spectra return to the original value of the substrate, which means that the film has been etched. Although in the deposition conditions the etching rate will be reduced by the dilution with H_2 due to quenching of F atoms through a reaction:

$$H_2 + F \rightarrow HF + H, \tag{5.1}$$

residual fluorine atoms and/or F-containing radicals can still affect the growing surface as suggested from the increase of surface roughness.

Figures 5.7(a)–5.7(d) show the change of the composition in the bulk layer according to the growth under different SiF_4 flow ratios $SiF_4/(SiH_4+SiF_4)$ of 0, 0.5, 0.75 and 1, respectively. The crystalline fraction increases and the amorphous fraction decreases with increase of the thickness. As the solid-phase crystallization does not proceed at 300°C, this result means that the a-Si layer grows initially, and the crystalline fraction deposited on it increases by layer. The first data point in Fig.5.7(c) shows a peculiar behavior. In this case the film tends to grow after some initial delay time due to the etching effect of F-containing radicals as can be seen in Figs.5.5(a) and 5.5(b). The

data point has been taken in this delay period. Therefore, the apparent high density of voids only shows the island-like growth of a-Si nuclei. The same behavior could also be seen for lower concentration of SiF_4. However, the delay time become shorter and the nuclei coalesce already to form a film at the time when the first data point in Fig.5.7(b) has been taken.

As seen in Fig.5.7(a), the crystalline fraction increases even under the condition without SiF_4, but its value saturates to about 0.5 in a short time. This means that the nucleation of the c-Si fraction can occur without the etching effect. However, the nuclei may be covered with amorphous tissue in this condition, which suppresses further growth of the crystalline grains.

By supplying SiF_4 at a flow ratio of 0.5, the crystalline fraction does not saturate so quickly and increases up to 0.8 as shown in Fig.5.7(b). At the same time, the amorphous fraction decreases. These results suggest that the amorphous tissue is etched out, and further increase of the crystalline fraction may proceed. A larger roughened thickness in Fig.5.5(a) is regarded as a result of the etching. A certain amount of voids in the bulk layer shown in Fig.5.7(b) may be taken in by burial of unfilled small wells on the roughened surface.

At the highest SiF_4 flow ratios of 0.75, however, the crystalline fraction does not reach the 0.8 attained for SiF_4 flow ratio of 0.5. As the roughened thickness and the void fraction in this case show larger values, the crystalline part may also be etched due to higher flux of the etchants. Although the absolute value of the crystalline fraction becomes lower due to the void inclusion at a higher SiF_4 flow ratio, the crystalline fraction relative to the amorphous fraction becomes higher. In addition, the critical thickness at which the crystalline fraction exceeds the amorphous one becomes thinner with increase of the SiF_4 flow ratio.

Figure 5.8 shows the diffraction pattern in a transmission electron microscopy (TEM) observation together with the bright field image of a film deposited at the SiF_4 flow ratio of 0.5. As can be seen in the figure, some sharp rings are observed, which means that the film has a certain amount of crystalline fraction.

Figures 5.9(a) and 5.9(b) show the IR-absorption spectra of the film and the hydrogen content derived from the area of the spectra, respectively. The peak centered at 2000 cm^{-1} arises due to Si-H bonds, and that at 2090cm^{-1} does due to Si-H_2 bonds. Integrated absorption intensity for both peaks are proportional to the density of these bonds in the film. As can be seen in

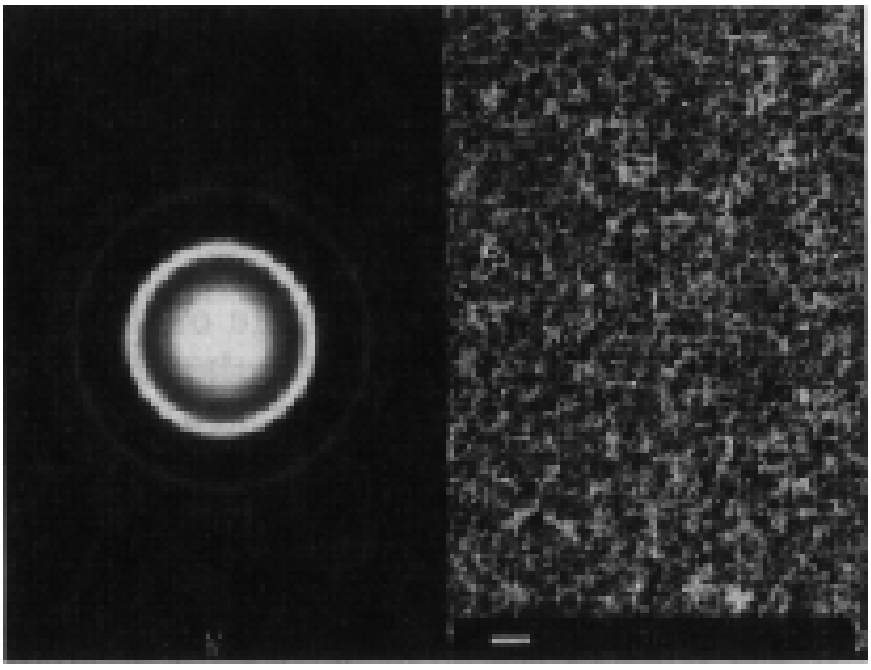

Fig. 5.8: Diffraction pattern and bright field image observed by transmission electron microscopy for the film deposited with SiF_4 flow ratio of 0.5.

Fig.5.9(a), the peak at 2000 cm^{-1} decreases with increase of SiF_4 flow ratio, and only the 2090 cm^{-1} peak remains for the highest SiF_4 flow ratio. The grain boundary in poly-Si is reported to be covered with Si-H_2 bonds rather than Si-H bonds [13]. Therefore, this result suggests that crystalline grains are formed in the films, and the grain boundary is covered mainly with Si-H_2. In addition, the total hydrogen content decreases drastically down to 8 at.%. This result also supports the increase of crystalline fraction in the deposited films by addition of SiF_4. Slight increase of the hydrogen content at the highest SiF_4 flow ratio of 0.75 is due to a relatively larger void fraction of 10% in the film shown in Fig.5.7(c).

5.2.4 H_2-dilution rate dependence

Figures 5.10(a)-5.10(c) show the thickness dependence of the volumetric fraction of c-Si in films deposited with and without SiF_4 for H_2 dilution rates of 80, 96 and 99%. The RF power, pressure, and total flow rate are 100 W, 0.1 Torr and 100 sccm, respectively. The SiF_4/SiH_4 flow ratio is 1/1. As can be seen in the figures, the initial increase in the volumetric fraction of c-Si is improved by SiF_4 addition, and with increasing H_2 dilution rate. These results indicate that

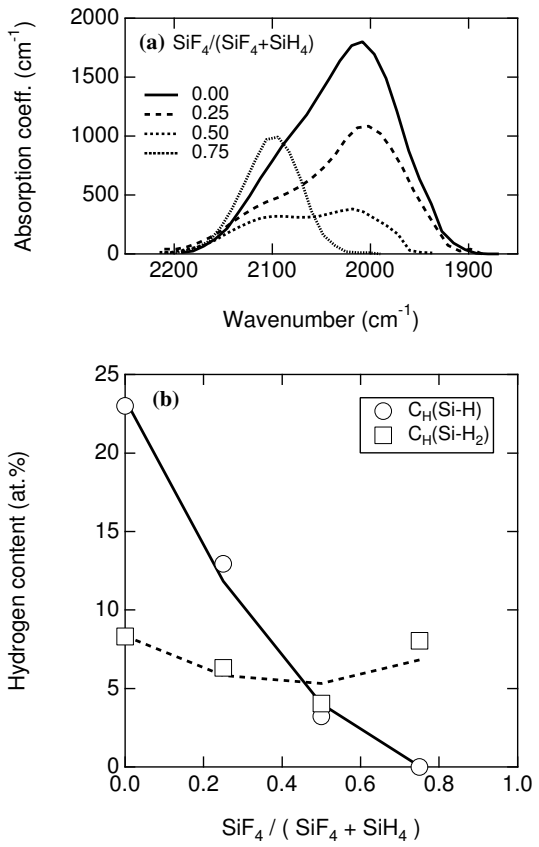

Fig. 5.9: (a) Infrared spectra of absorption coefficient around 2000 cm^{-1} for the films deposited at different SiF_4 flow ratios, and (b) hydrogen concentration in mono- and di-hydride bonds deduced from the integrated absorption coefficient of the spectra shown in (a).

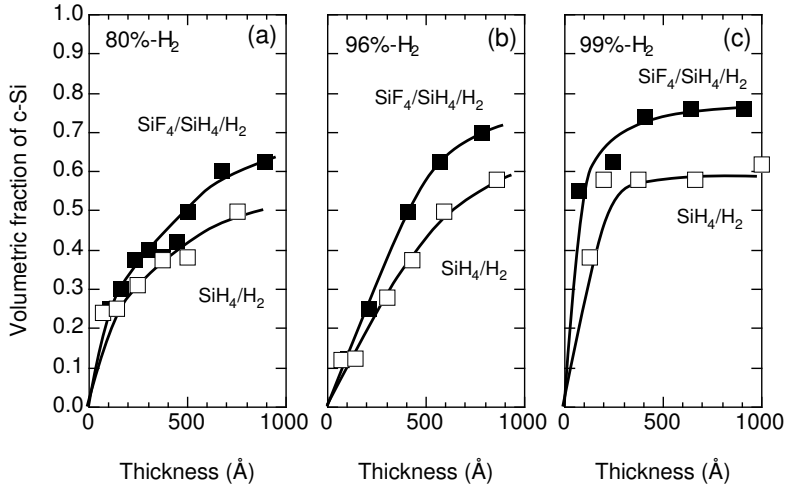

Fig. 5.10: Volumetric Fraction of c-Si as a function of the thickness of films deposited at H_2 dilution ratio of (a) 80%, (b) 96% and (c) 99%.

H_2 molecules and/or H radicals should promote an increase in the crystalline part in the growing film surface. H_2 molecules are considered to act mainly as terminators of reactive species, such as Si, SiH, SiH_2 in the gas phase, and not to affect the growing film surface directly. In this thesis, therefore, effects of H radicals impinging onto the growing films are investigated, and its details are described in the section 5.5.

5.3 Gas-phase reaction simulation

5.3.1 Description of the model

A preliminary simulation of gas-phase reactions has been performed in order to estimate the gas phase compositions in the condition where the highest c-Si fraction has been obtained. Spatially dependent electron impact dissociation rates of the source gases are determined from a one dimensional plasma fluid model under the local field approximation [14]. Then reaction kinetics are simulated using the obtained dissociation rates [15]. In addition to the dominant reactions given by Kushner [16], some reactions are considered as shown in Table 5.1 [17–19]. The reactions taken into account are only the reactions between stable species and radicals, since radical-radical reaction is negligible due to their low density. The reaction rate constants denoted by '*' are estimated from similar reactions including halogen and/or halogenated silicon or carbon.

5.3.2 Simulation results

As seen in the results shown in Figs.5.11(a) and 5.11(b), the dominant radicals are SiH_3, H, SiF_3 and SiF_2. This is in accordance with the magnitude of dissociation rate and its branching ratio listed in Table 5.1. Although F radicals are generated in the initial decomposition with the same rate for SiF_3, its density is fairly reduced due to quenching by H_2 in the bulk plasma region and by higher reaction loss at the surface. However, since the production of F radical is larger at the sheath edge near the electrode, its flux onto the film surface becomes fairly large. As the sticking probability of SiH_3 and $SiF_n (n \leq 3)$ is reported to be small as about 0.1–0.15 [20, 21], this result means that the etching effect by F radicals is not negligible even in H_2 diluted condition in this work.

Tab. 5.1: Reactions considered in gas-phase simulation and their rate constants in cm^3 mol^{-1} s^{-1}. () indicates quantum yield. "*" estimated from similar reactions including halogen and/or halogenated silicon or carbon.

No.	Reactants		Products	Rate constant
	Electron Impact Dissociation			
R_1	$SiF_4 + e$	$\rightarrow$	$SiF_3 + F + e$	(78.0%)
R_2		$\rightarrow$	$SiF_2 + F_2 + e$	(19.2%)
R_3		$\rightarrow$	$SiF + F_2 + F + e$	(1.8%)
R_4		$\rightarrow$	$Si + F_2 + F_2 + e$	(1.0%)
	Secondary reactions			
R_5	$H + F_2$	$\rightarrow$	$F + HF$	8.97×10^{11}
R_6	$H + SiH_2F_2$	$\rightarrow$	$SiH_2F + HF$	6.68×10^{10}
R_7	$F + H_2$	$\rightarrow$	$H + HF$	1.49×10^{13}
R_8	$F + SiH_4$	$\rightarrow$	$SiH_3 + HF$	2.59×10^{14}
R_9	$F + SiH_2F_2$	$\rightarrow$	$SiHF_2 + HF$	3.43×10^{12}*
R_{10}	$Si + F_2$	$\rightarrow$	$F + SiF$	1.74×10^{13}
R_{11}	$Si + SiF_4$	$\rightarrow$	$SiF_2 + SiF_2$	1.44×10^{13}
R_{12}	$SiH + F_2$	$\rightarrow$	$SiHF_2$	9.03×10^{13}*
R_{13}	$SiH_2 + F_2$	$\rightarrow$	SiH_2F_2	8.43×10^{13}*
R_{14}	$SiH_3 + F_2$	$\rightarrow$	$F + SiH_3F$	1.23×10^{12}*
R_{15}	$SiH_3 + SiHF_3$	$\rightarrow$	$SiF_3 + SiH_4$	1.31×10^{11}*
R_{16}	$SiF + F_2$	$\rightarrow$	$F + SiF_2$	1.68×10^{13}
R_{17}	$SiF + SiF_4$	$\rightarrow$	$SiF_3 + SiF_2$	1.44×10^{13}
R_{18}	$SiF_2 + F_2$	$\rightarrow$	$F + SiF_3$	2.83×10^{11}
R_{19}	$SiF_2 + SiF_4$	$\rightarrow$	Si_2F_6	3.30×10^{11}*
R_{20}	$SiF_3 + F_2$	$\rightarrow$	$F + SiF_4$	9.03×10^{11}*
R_{21}	$SiF_3 + SiH_4$	$\rightarrow$	$SiH_3 + SiHF_3$	1.92×10^{8}*
R_{22}	$SiHF_2 + SiHF_3$	$\rightarrow$	$SiF_3 + SiH_2F_2$	3.92×10^{14}*

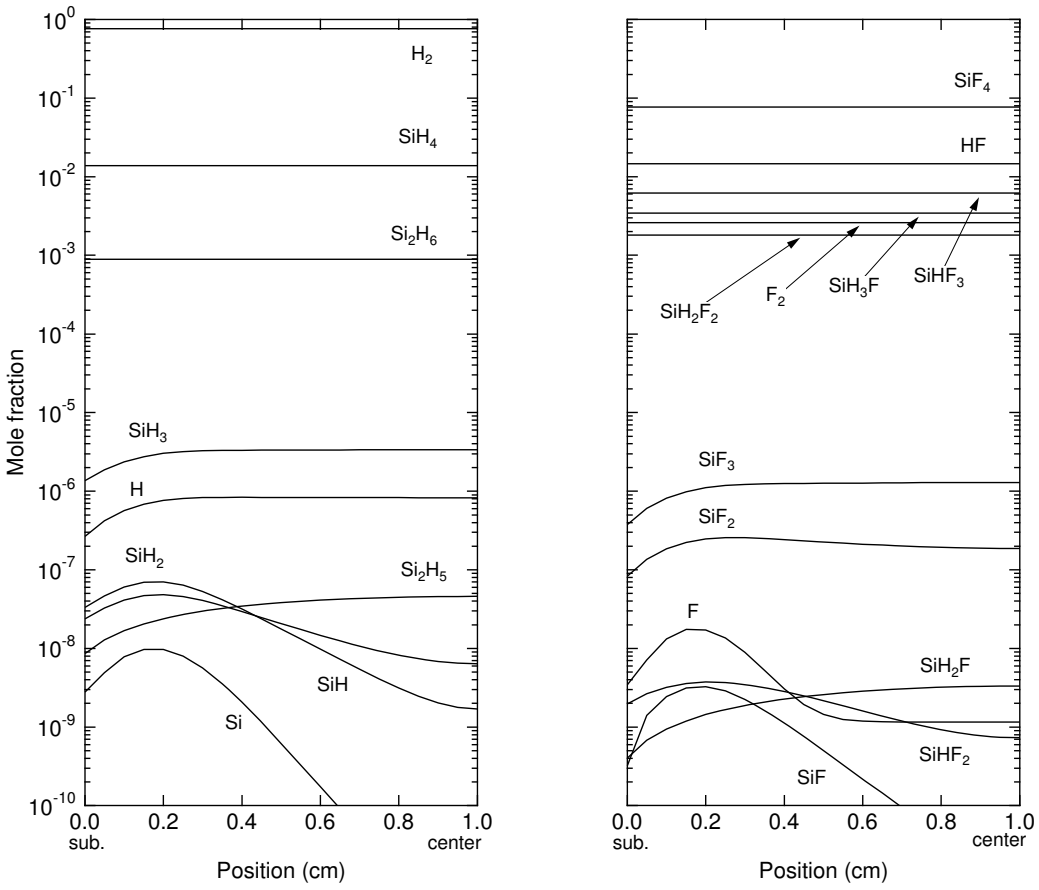

Fig. 5.11: Gas-phase composition of $SiF_4/SiH_4/H_2$ plasma calculated by simulation under the condition of $SiF_4/SiH_4/H_2$=2/2/16 sccm, total pressure 0.2 Torr and RF power density 500 mW/cm^2.

5.3.3 Deposition precursors

The density of SiH_2F and $SiHF_2$ radicals, which have been suggested to be deposition precursors in poly-Si growth using hydrogen radical enhanced CVD [22], is fairly smaller than the dominant radicals. As we have not considered the decomposition of SiH_nF_{4-n}(n=1–3) in the present simulation because cross sections and branching ratios are unknown, SiH_2F and $SiHF_2$ may be generated from SiH_nF_{4-n}. However, from the mass spectrometry analysis shown in Figs.5.12(a) and 5.12(b), intensities of SiH_2F^+ and $SiHF_2^+$ which are expected to originate from SiH_nF_{4-n} does not show positive correlation between the deposition rate. As the dissociation degrees of SiH_4 and SiF_4 are almost constant for any SiF_4 flow ratio as shown in Fig.5.12(c), the decrease of the deposition rate with increasing SiF_4 flow ratio is due to decrease of SiH_4 supply. This means that the dominant deposition precursor is supplied from SiH_4 and presumably SiH_3 radicals. As the deposition rate does not become zero even without SiH_4, contribution of SiF_3 and SiF_2 is not negligible. However, deposition rate in SiF_4/H_2 plasma is 1/3 of that in SiH_4/H_2 plasma. Therefore, SiF_3 and SiF_2 do not contribute so much to the deposition as SiH_3 does.

From these results, the dominant deposition precursor is concluded to be SiH_3 radicals in the condition where the higher c-Si fraction has been obtained, and the degree of preferential etching by F radicals determines the film compositions.

5.4 Roles of fluorinated radicals

As suggested in the previous section, fluorinated radicals are considered to work in preferential etching of amorphous tissue preventing crystalline growth. In order to investigate the etching selectivity, SE measurements have been performed on 100% a-Si and 100% poly-Si films under pure SiF_4 plasma treatment. The a-Si film has been prepared on a quartz substrate at 480°C by a low pressure CVD, and the poly-Si film has been prepared by annealing the a-Si at 600°C for 24 hours. During the treatment, flow rate of SiF_4, pressure, RF power density and $T_{\rm sub}$ are 4 sccm, 0.2 Torr, 500 mW/cm^2 and 300°C, respectively. Figure 5.13 shows film thickness as a function of the treatment time. From this figure, one can see that etching rate of a-Si is 0.075 nm/s which are three times as large as the value of c-Si. This means that c-Si is also

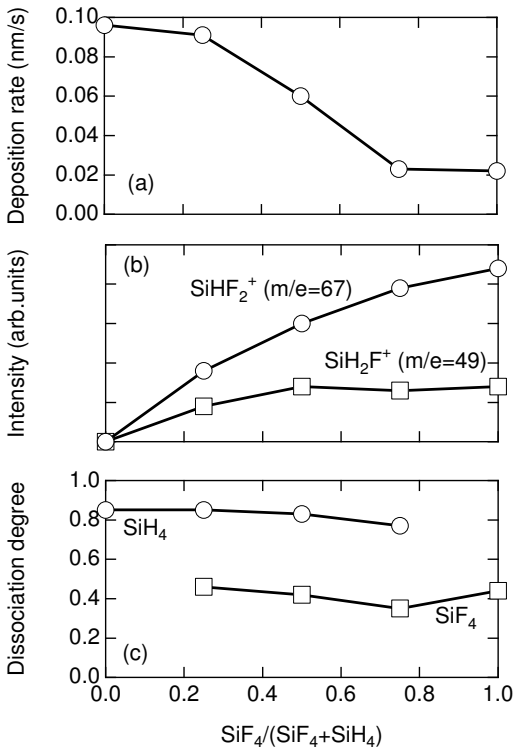

Fig. 5.12: Correlation between (a) deposition rate, (b) mass intensity of SiH_2F^+ and $SiHF_2^+$ which arise from stable molecules SiH_nF_{4-n}, and (c) dissociation degree of SiH_4 and SiF_4.

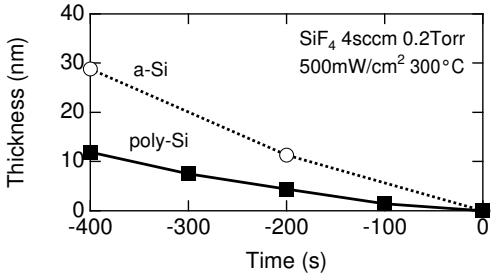

Fig. 5.13: Thickness of a-Si and poly-Si thin films as a function of SiF_4 plasma treatment time, where RF power density, SiF_4 flow rate, pressure and substrate temperature is 500 mW/cm^2, 4 sccm, 0.2 Torr, 300°C, respectively.

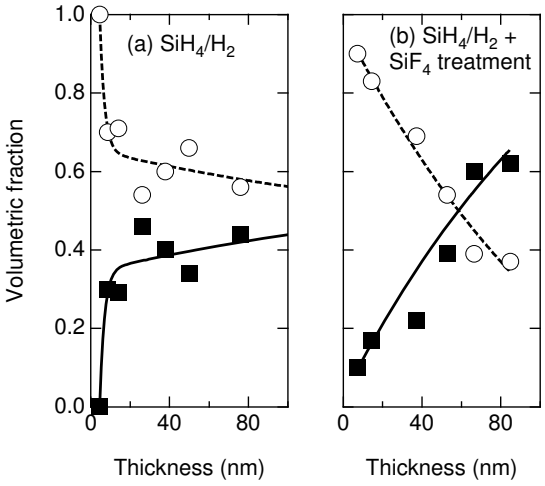

Fig. 5.14: Composition of the films deposited (a) without SiF_4 and (b) with SiF_4 treatment.

etched out, and the surface roughness and the void fraction increase if SiF_4 flow ratio becomes too large as can be seen in Fig.5.7

In the film deposition conditions, etching rate should be fairly lower than in the SiF_4 plasma operated at 0.2 Torr, because SiF_4 is highly diluted with H_2 and etchant F atoms are quenched by H_2 molecules. For the purpose of realizing a moderate etching condition, a film has been prepared by repeating SiH_4/H_2 plasma deposition and SiF_4 plasma treatment at lower pressure (0.04 Torr) sequentially. Both the deposition and the treatment have been done for a 100–200 s period. The difference before and after the SiF_4 treatment in each sequence appears only slightly in roughened top layer thickness. However, accumulated result in Fig.5.14 shows marked difference. Fraction of c-Si does not saturates but increases up to 63%.

From these results, a role of fluorinated radicals is concluded to be semi-preferential etching of a-Si part which prohibits growth of c-Si fraction under the condition where both a-Si growth and c-Si nucleation occur.

5.5 Roles of hydrogen radicals

In order to clarify the effects of hydrogen dilution, several methods have been examined, such as sequential repetition of deposition with SiH_4 plasma and treatment with H_2 plasma or remote H_2 plasma [23–28]. In these studies, H radicals are believed to promote the appearance of the crystalline phase. These are two possible explanations for this phenomenon. One is that H

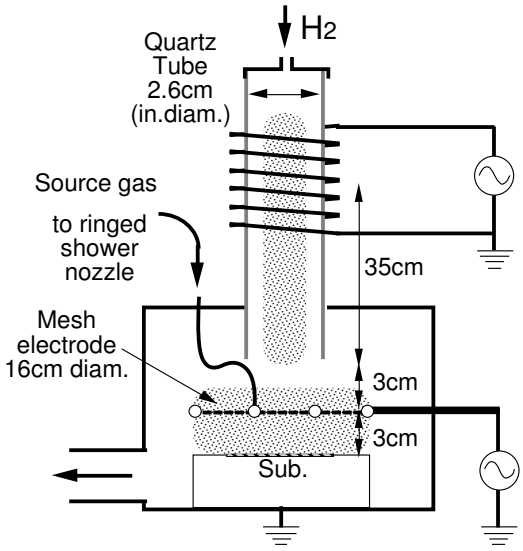

Fig. 5.15: Experimental Setup for film deposition and H radical treatment.

radicals result in a surface condition in which deposited SiH_3 radicals form crystalline bonds. Matsuda proposed that formation of crystalline bonds is due to sufficient hydrogen coverage on the growing surface which promotes surface migration of SiH_3 to lead more stable sites [2]. Another explanation is that H radicals impinging on the growing surface promote the formation of crystal Si-Si bonds in the surface. Shirai proposed that it was the mechanism of Si-Si bond formation involves the creation of free volume due to inhomogeneous etching which promotes cross-linking and rearrangement of the Si network [29]. The effect of H radicals, however, is considered to change with thickness, because the structures of the layers deposited on glass substrates and those deposited on a film deposited previously are different. In this section, therefore, the thickness dependence in the effects of H radicals is investigated by using *in situ* ellipsometric monitoring of film surface during H radical treatment.

5.5.1 Experimental procedures

Figure 5.15 shows the experimental setup for film deposition and H radical treatment. The films are deposited on Corning 7059 glass substrates using a capacitively coupled RF PE-CVD method and $SiF_4/SiH_4/H_2$ gas mixtures. The H radical treatment is carried out using an inductively coupled RF plasma generator as the H radical source [30]. Density of H radicals is in the order of 10^{12} cm^{-3} at input RF power of 100 W and H_2 pressure ranging from 0.001

to 1 Torr. In order to lead H radicals onto the substrate through a powered electrode, a mesh electrode is used as shown in the figure. The substrate temperature is 300°C.

Monitoring of surfaces has been carried out by using an ME method at a wavelength of 380 nm during film deposition and H radical treatment, and by using an SE method at wavelengths in the range of 350–680 nm before and after the deposition. The angle of incidence is 73.8°.

The trajectories of $\tan\Psi$ and $\cos\Delta$ obtained by ME measurements during deposition and H radical treatment are analyzed by comparison to theoretical trajectories calculated using the three-layer model and newly developed multi-layer model. Amorphous silicon, crystalline silicon and voids are considered to be the components of the layers. The dielectric functions of these components at 300°C have been determined as described in the previous section. It has been assumed that the thickness and volumetric fractions of the components of each layer change linearly along with increase (or decrease) in film thickness during deposition and H radical treatment.

5.5.2 Roles of hydrogen radicals on hydrogenated films

Figures 5.16(a), 5.16(b) and 5.17(a) show the trajectories during film deposition and the H radical treatment for films with thickness of 36, 60 and 628Å, respectively.

As can be seen in Figs.5.16(a) and 5.16(b), the trajectory obtained during the H radical treatment is almost the reverse of that obtained during the deposition sequence. This means that the effect of the H radical treatment is mostly etching for films less than 60Å thick.

In contrast, the trajectory obtained during the H radical treatment of the film 628Å thick shown in Fig.5.17(a) is different from that obtained during deposition. The difference is particularly obvious at the initial stage of the H radical treatment. Therefore, another model is required to describe the initial stage. After passing through the region of $\cos\Delta$=0, the trajectory becomes almost the same as that of thin films, because the thickness of the film is similar to those of the films in Figs.5.16(a) and 5.16(b).

Since the value of $\cos\Delta$ at the convergence point in the trajectory increases with surface roughness, theoretical trajectories are calculated using a model which takes surface roughness formation into account. Figure 5.17(b) shows trajectories calculated using two models which include

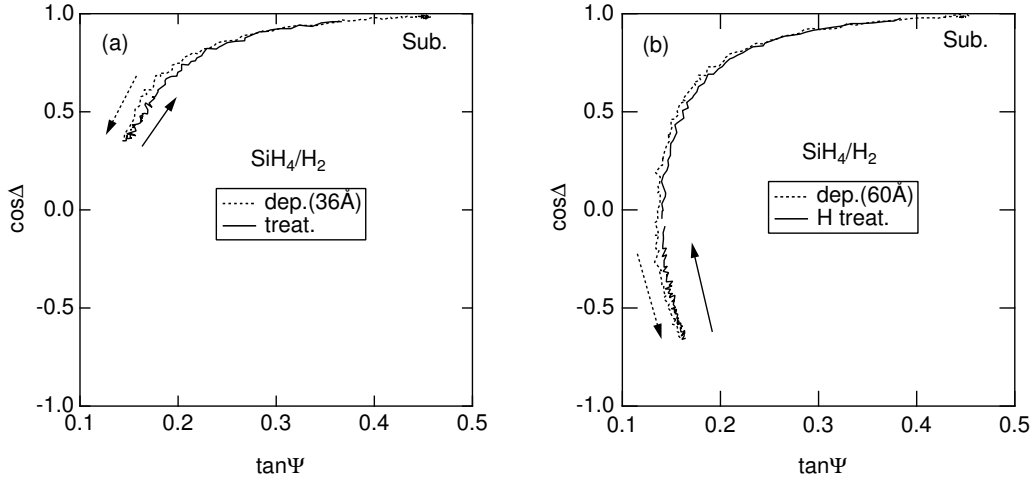

Fig. 5.16: Trajectories during film deposition using SiH_4/H_2 plasma and H radical treatment for the film thickness of (a) 36Å and (b) 60Å.

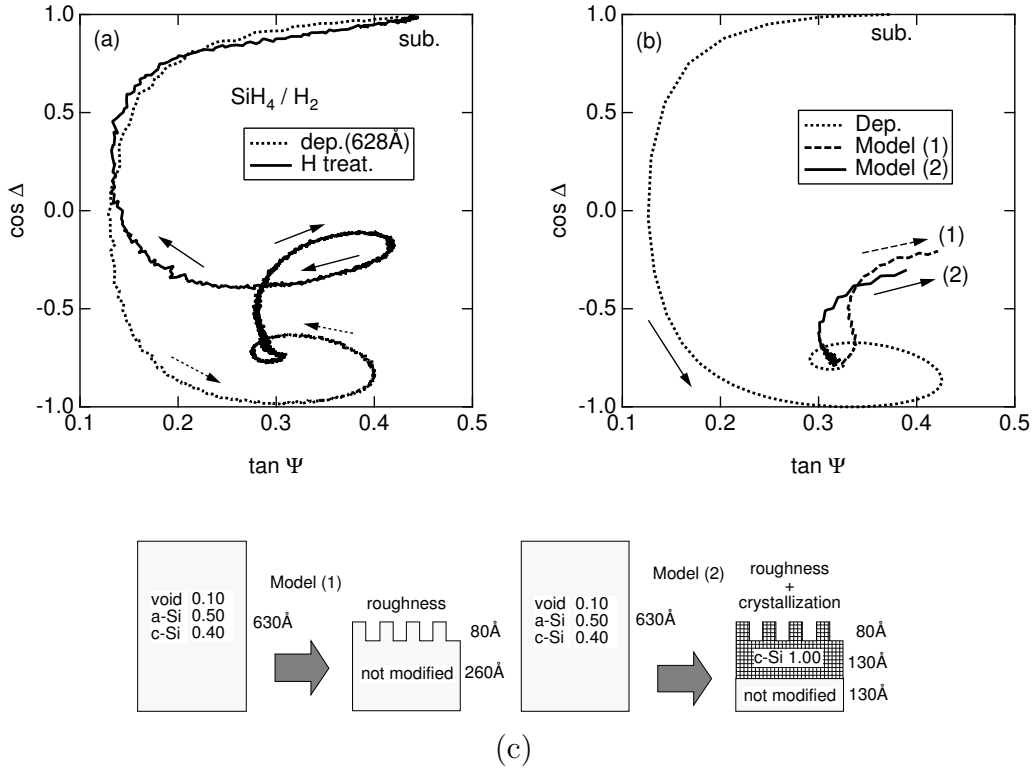

Fig. 5.17: (a) Measured trajectory during deposition up to 628Å using SiH_4/H_2 plasma and H radical treatment. (b) Trajectories calculated using the model shown in (c).

Model(1) pure etching and roughness formation, and

Model(2) pure etching, roughness formation and surface crystallization,

based on the schemes shown in Fig.5.17(c). The films are assumed to have uniform composition. In relation to the deposition sequence, the experimental and calculated results show good agreement. Summarizing the above results, we conclude that H radicals cause both etching and crystallization. The crystallization effect reaches layers deeper than those affected by etching, since a crystallized layer remains on the surface after etching. The almost pure etching of thin films is considered to be due to the fact that the thickness is insufficient for a crystallized layers to remain, and that films are formed with weak Si-Si bonds which can easily be broken. The roughness of the thick films is considered to be due to an increase in the Si-Si bond strength, and the partial removal of Si atoms due to breaking of the weaker bonds.

5.5.3 Roles of hydrogen radicals on fluorinated films

The hydrogen radical enhanced CVD proposed by Shimizu and co-workers uses fluorinated precursors, and be used to prepare polycrystalline or epitaxial Si successfully [5, 31, 32]. The effects of H radical treatment on films deposited using SiF_4-containing plasma are expected to be different from on films deposited with SiH_4 plasma, because the Si-F bond is stronger than the Si-H bond. As the degree of decomposition of SiF_4 is approximately 1/6 of that of SiH_4 at an RF power of 10 W, deposition of the films was carried out at 100 W so that the degree of decomposition was 1/2 that of SiH_4. The conditions for the H radical treatment ware the same as those above.

Figures 5.18(a) and 5.18(b) show the trajectories for deposition and H radical treatment of films of 38 and 62Å thick. Comparing these figures to Figs.5.16(a) and 5.16(b), one can see that they are almost the same. This means that H radicals act mainly as etchants for thin films, even if the films are deposited with SiF_4-containing plasma.

On the other hand, the trajectory for a film 700Å thick shown in Fig.5.19(a) is different from those for thin films in Figs.5.18(a) and 5.18(b). As the film composition in this case is different from that of the films deposited using SiH_4/H_2, the basic shape of the trajectories is different from that in Fig.5.17(a). As the trajectory in this case is also the reverse of that for the deposition

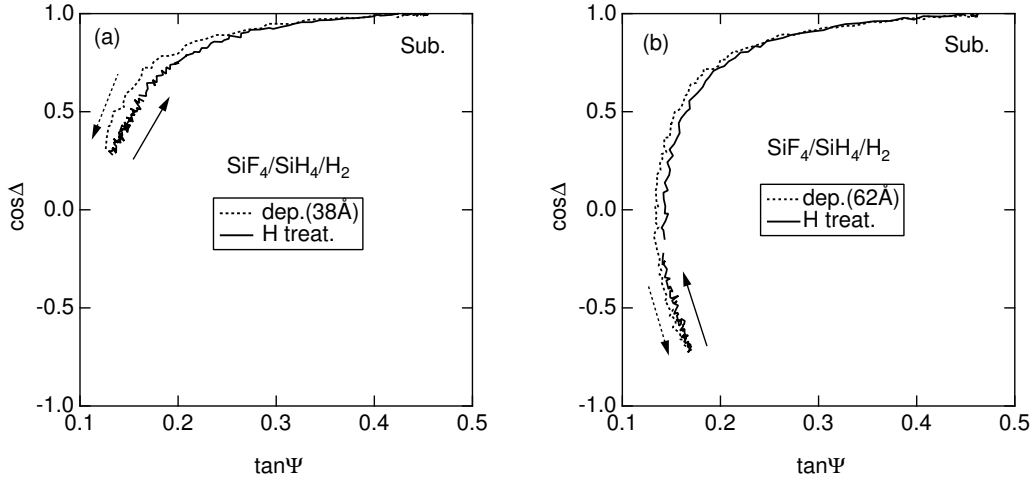

Fig. 5.18: Trajectories during film deposition using $SiF_4/SiH_4/H_2$ plasma and H radical treatment for film thickness of (a) 38Å and (b) 62Å.

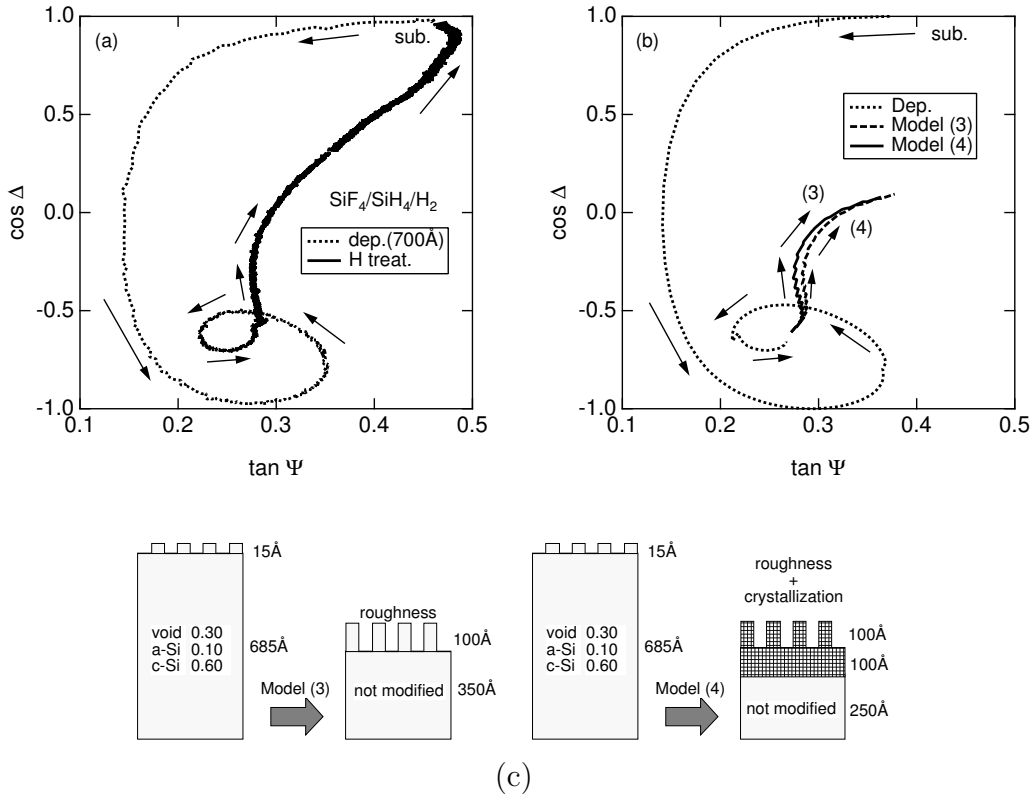

Fig. 5.19: (a) Measured trajectory during deposition of up to 700Å using $SiF_4/SiH_4/H_2$ plasma and H radical treatment. (b) Trajectories calculated using the models shown in (c).

process, etching occurs.

In order to explain this behavior, the experimental trajectories are compared to calculated ones. The model used here is similar to that used in the previous subsection. Figure 5.23(b) shows trajectories calculated using models (3) and (4) which represent the etching process without and with surface crystallization, respectively. The schematic diagrams for these models are shown in Fig.5.23(c).

In contrast to the calculated trajectories for films deposited without SiF_4, the difference between the trajectories for the films with and without surface crystallization is small. This is because the volumetric fraction of the crystalline phase is already high during the deposition sequence. Regarding the initial stage of the trajectory calculated using the model (3), which is represented by a dashed line in Fig.5.19(b), only $\cos\Delta$ increases and $\tan\Psi$ is almost constant. On the other hand, $\tan\Psi$ in the trajectory calculated using the model (4) which is represented by a solid line in Fig.5.19(b) decreases once, which shows better agreement with the experimental trajectory.

I have expected a difference in the H radical effects on films deposited with and without SiF_4. However, these results indicate that there are no marked differences in the effects of H radical treatment in these cases at the initial stage of the treatment.

5.6 Summary

In summary, a spectroscopic ellipsometry method has been successfully used for monitoring the temporal change in the film composition in the plasma CVD of polycrystalline silicon films with mixed source gases of SiH_4 and SiF_4 diluted by H_2. Even without SiF_4 addition, the inclusion of crystalline component has been recognized, but the crystalline fraction has saturated at 50%. At higher mixing ratio of SiF_4, the crystalline fraction has increased up to 80% at an optimum flow ratio of $SiF_4/SiH_4/H_2$, although the growth rate has decreased and the surface roughness has increased.

Repetition of SiF_4 plasma treatment and SiH_4/H_2 plasma deposition has also increased crystalline fraction without saturation. Etching rate of a-Si in SiF_4 plasma has been approximately three times higher than that of c-Si. These results mean that the increase in the crystalline fraction with mixing SiF_4 is due to semi-preferential etching of amorphous tissue which sup-

press growth of crystalline region. From the gas-phase simulation, most likely etchant has been determined to be fluorine radicals.

Dominant deposition precursor predicted from the gas-phase simulation and mass analysis has been SiH_3 from SiH_4, and the density of fluorinated precursors such as SiH_2F and $SiHF_2$ is lower than the dominant precursor. Contribution of SiF_3 and SiF_2 has also been predicted to be low from the relationship between deposition rate and dissociation degree of SiF_4 gas.

Roles of hydrogen radicals have been investigated by using a separated hydrogen radical source. *In situ* ellipsometric monitoring of surface during hydrogen radical treatment of the grown film surface has revealed that hydrogen radicals have effects of etching and surface crystallization. For thin films less than 100Å, hydrogen radicals work mostly in etching, and crystallization effect has appeared for thick films more than 500Å.

References

[1] Y. Toyoshima, K. Arai and A. Matsuda: J. Non-Cryst. Solids **114** (1980) 819.

[2] A. Matsuda: J. Non-Cryst. Solids **59–60** (1983) 767.

[3] H. Kakinuma, M. Mohri, M. Sakamoto and T. Tsuruoka: J. Appl. Phys. **70** (1991) 7374.

[4] T. Nagahara, K. Fujimoto, N. Kohno, Y. Kashiwagi and H. Kakinoki: Jpn. J. Appl. Phys. **31** (1992) 4555.

[5] M. Nakata, A. Sakai, T. Uematsu, T. Namikawa, H. Shirai, J. Hanna and I. Shimizu: Phil. Mag. B **63** (1991) 87.

[6] E. Ohno, A. Yoshinouchi, T. Hosoda, M. Itoh, T. Morita and S. Tsuchimoto: Jpn. J. Appl. Phys. **33** (1994) 635.

[7] P. S. Hauge and F. H. Dill: IBM J. Res. Develop. **17** (1973) 472.

[8] M. J. D. Powell: *Numerical Methods for Unconstrained Optimization*, Ed. W. Murray (Academic Press, New York, 1973) pp.29–55.

[9] D. E. Aspnes: Thin Solid Films **89** (1982) 249.

[10] D. E. Aspnes: Am. J. Phys. **50** (1982) 704.

[11] G. E. Jellison, Jr and F. A. Modine: *Optical Functions of Silicon at Elevated Temperatures Determined by Polarization Modulation Ellipsometry* (Oak Ridge National Laboratory, Oak Ridge, 1985) ORNL/TM-9718.

[12] D. E. Aspnes, A. A. Studna and E. Kinsbron: Phys. Rev. B **29** (1984) 768.

[13] A. Matsuda: Jpn. J. Appl. Phys. **20** (1981) L439.

[14] J. P. Boeuf: Phys. Rev. A, **36** (1987) 2782.

[15] T. Shirafuji, S. Nakajima, Y. -F. Wang, T. Genji and K. Tachibana: Jpn. J. Appl. Phys. **32** (1993) 1546.

[16] M. J. Kushner: J. Appl. Phys. **63** (1988) 2532.

[17] M. Hayashi: *Swarm Studies and Inelastic Electron-Molecule Collisions*, Ed. L. C. Pitchford, B. V. McKoy, A. Chutjian and S. Trajmar (Springer Verlag, New York, 1985) p.167.

[18] T. Nakano and H. Sugai: J. Phys. D **26** (1993) 1909.

[19] *Gas-phase Chemical Physics Database* (Elsevier Science Publishers, New York, 1988).

[20] A. Yuuki, Y. Matsui and K. Tachibana: Jpn. J. Appl. Phys. **28** (1989) 212.

[21] H. U. Lee, J. P. de Neufvill and S. Ovshinsky: J. Non-Cryst. Solids **59–60** (1983) 671.

[22] T. Akasaka, Y. Araki, M. Nakata and I. Shimizu: Jpn. J. Appl. Phys. **32** (1993) 2607.

[23] A. Asano: Appl. Phys. Lett **56** (1990) 533.

[24] K. Nomoto, Y. Urano, J. L. Guizot, G. Ganguly and A. Matsuda: Jpn. J. Appl. Phys. **29** (1990) L1372.

[25] H. Shirai, J. Hanna and I. Shimizu: Jpn. J. Appl. Phys. **30** (1991) L679.

[26] M. Otobe: Jpn. J. Appl. Phys. **31** (1992) L1443.

[27] T. Kaneko, K. Onisawa, M. Wakagi, Y. Kita and T. Minemura: Jpn. J. Appl. Phys. **32** (1993) 4907.

[28] K. Nakamura, K. Yoshino, S. Takeoka and I. Shimizu: Jpn. J. Appl. Phys. **34** (1995) 442.

[29] H. Shirai: Jpn. J. Appl. Phys. **34** (1995) 450.

[30] K. Tachibana: Jpn. J. Appl. Phys. **33** (1994) 4329.

[31] N. Shibata, K. Fukuda, H. Ohtoshi, J Hanna, S. Oda and I. Shimizu: Mater. Res. Soc. Symp. Proc. **95** (1987) 225.

[32] T. Akasaka, Y. Araki and I. Shimizu: Jpn. J. Appl. Phys. **33** (1994) 956.

Chapter 6

Conclusions

6.1 Conclusions

In this study, reaction kinetics in the photo and plasma enhanced chemical vapor deposition of a-Si:H, μc-Si and poly-Si thin films have been investigated with the aid of simulation and *in situ* gas-phase and surface monitoring techniques. The investigations have been focused on the roles of the radical species generated in the gas phase and contribute to the deposition and modification of the films and their surface.

In chapter 2, I have shown that the combination of Si_2H_6 and 147-nm excitation can prepare high quality a-Si:H films, which have low defect-state density, low hydrogen concentration, low Si-H_2 bond density, low photo-degradation, high photoconductivity.

In chapter 3, I have investigated the reason why the combination of Si_2H_6 and 147-nm excitation brings about such high quality. From a simulation of gas-phase and surface reactions, it has been concluded that the good properties are caused by the smaller contribution of biradicals such as SiH_2 and Si_2H_4 and larger contribution of monoradicals such as SiH_3 and Si_2H_5 to deposition of the films.

In chapter 4, density of SiH_2 radicals has been measured using an intra cavity laser absorption spectroscopy in SiH_4 and Si_2H_6 plasmas diluted with He, Ar and Xe. The density of SiH_2 radicals has increased with the dilution. Performing the reaction simulation technique, this result has been explained in terms of increase in dissociation rate of parent-gas molecules. Its main cause is increase of electron energy as for He dilution, while that is increase of electron density as for Xe dilution. In case of Ar dilution, both of them contribute to the increase in the dissociation rate. A Monte-Carlo surface reaction simulation has been performed in order to clarify the cause of increase in the density of

Si-H_2 bonds in the films with increase of contribution of SiH_2 radicals. The increase in Si-H_2 bond density has been explained that SiH_2 radicals with higher sticking probability than SiH_3 radicals results in rough surface, and that the roughness causes a lower rate of the interconnection reactions which eliminate Si-H_2 bonds. The surface roughness formation has been verified using *in situ* ellipsometric monitoring of the growth of the growing film surface.

In chapter 5, reaction simulation techniques and *in situ* gas phase and surface monitoring technique has been applied to μc and poly-Si growth process in order to clarify roles of hydrogenated and fluorinated radicals in $SiH_4/SiF_4/H_2$ plasma. The increase in the crystalline fraction with mixing SiF_4 has been due to semi-preferential etching of amorphous tissue which suppress growth of crystalline region. From the gas-phase simulation, most likely etchant has been determined to be fluorine radicals. Dominant deposition precursor has been SiH_3 from SiH_4, and the density of fluorinated precursors such as SiH_2F and $SiHF_2$ is lower than the dominant precursor. Contribution of SiF_3 and SiF_2 has also been predicted to be low from the relationship between deposition rate and dissociation degree of SiF_4 gas. Hydrogen radicals have effects of etching and surface crystallization. For thin film less than 100Å, hydrogen radicals work mostly in etching, and crystallization effect has appeared for thick films more than 500Å.

6.2 Future prospects

In this study, it has been demonstrated that a combination of reaction simulation and *in situ* process monitoring worthful for understanding mechanisms in CVD processes. Although these techniques have been applied just for investigation of surface phenomena, it can be applied to controlling the process by feeding the monitored results back to the process parameters. Although current semiconductor processes use static process parameters, I expects that the process parameters will be controlled in more dynamic manner [1] on the basis of *in situ* monitoring of the process and prediction by simulations. Especially on the growth of polycrystalline silicon films, the process parameters for nucleation and growth is different, and they must be switched at suitable timing, which requires above mentioned *in situ* monitoring and controlling. In order to realize such an environment, however, the techniques used in this thesis must be improved.

Regarding *in situ* monitoring techniques, ellipsometry in UV and visible region presented in this work is not valid for detecting chemical species. Spectroscopy in infrared (IR) region can be used for the detection of chemical species as in infrared reflection absorption spectroscopy [2–4], attenuation total reflection [5] and infrared ellipsometry [6–8]. As these IR-techniques mostly utilize Fourier transform infrared spectrometer as a light source, light intensity is not high enough to detect low-density species on the surface. I expect that these conventional IR-techniques will be improved by using variable-wavelength high intensity IR-lasers.

Regarding reaction modeling techniques, at present, surface reaction modeling techniques are not fully established in comparison to gas-phase reaction modeling. In this thesis, I have performed modeling and simulation for only the deposition of amorphous films, and predicted film properties only by using the *ratio* of radical flux. However, there is another important parameter of *total* flux, namely, deposition rate which competes *relaxation time* for bonding configuration to be fixed on surface. The reason why I have successfully been able to predict structure of deposited films is that the relaxation time is short enough to be neglected, because amorphous structure is basically *freezed* at a metastable state. In the case of crystalline growth such as μc-Si and poly-Si growth, the relaxation time will become longer at the same temperature because the configuration of Si-Si bonds must be changed until they are fixed at the ground state, namely, crystalline structure. Although there are no surface reaction models to predict μc-Si and poly-Si growth at present, I expect that the proper model can be achieved by taking the *relaxation time* into account.

References

[1] M. Kildemo, P. Bulkin, S. Deniau and B. Drévillon: Appl. Phys. Lett. **68** (1996) 3395.

[2] T. Wadayama, H. Kayama, A. Hatta, W. Suëtaka and J. Hanna: Jpn. J. Appl. Phys. **29** (1990) 1884.

[3] Y. Toyoshima, K. Arai, A. Matsuda and K. Tanaka: Appl. Phys. Lett. **57** (1990) 1028.

[4] V. M. Bermudez: J. Vac. Sci. Technol. A **10** (1992) 3478.

[5] E. S. Aydil, Z. H. Zhou, R. A. Gottscho and Yves J. Chabal: J. Vac. Sci. Technol. B **13** (1995) 258.

[6] B. Drévillon: Appl. Surf. Sci. **63** (1993) 27.

[7] K. Tachibana, T. Shirafuji and S. Muraishi: Jpn. J. Appl. Phys. **35** (1996) 3652.

[8] T. Shirafuji, W. W. Stoffels, H. Moriguchi and K. Tachibana: J. Vac. Sci. Technol. A **15** (1997) 209.

List of publication

Full paper

1. *a-Si:H Deposited by Direct Photo-CVD Using a Microwave-excited Xe Lamp*
   Hiroyuki Matsunami, Tatsuru Shirafuji, Takashi Fuyuki and Masahiro Yoshimoto: Mater. Res. Soc. Symp. Proc. **192** (1990) pp.505–510.

2. *Low-hydrogen-concentration a-Si:H Deposited by Direct Photo-CVD*
   Tatsuru Shirafuji, Masahiro Yoshimoto, Takashi Fuyuki and Hiroyuki Matsunami: Solar Energy Mater. **23** (1991) pp.256–264.

3. *Measurement of SiH_2 Densities in an RF-Discharge Silane Plasma Used in the Chemical Vapor Deposition of Hydrogenated Amorphous Silicon Film*
   Kunihide Tachibana, Tatsuru Shirafuji and Yasuji Matsui: Jpn. J. Appl. Phys. **31** (1992) pp.2588–2591.

4. *Direct Photochemical Vapor Deposition of Hydrogenated Amorphous Silicon — Effects of Excitation Wavelengths and Source Gases —*
   Tatsuru Shirafuji, Sagara Nakajima, Yun-Fen Wang, Takeshi Genji and Kunihide Tachibana: Jpn. J. Appl. Phys. **32** (1993) pp.1546–1557.

5. *Measurement and Calculation of SiH_2 Radical Density in SiH_4 and Si_2H_6 Plasma for the Deposition of Hydrogenated Amorphous Silicon Thin Films*
   Tatsuru Shirafuji, Kunihide Tachibana and Yasuji Matsui: Jpn. J. Appl. Phys. **34** (1995) pp.4239–4246.

6. *In Situ Ellipsometric Monitoring of the Growth of Polycrystalline Silicon Thin Films by RF Plasma Chemical Vapor Deposition*
   Kunihide Tachibana, Tatsuru Shirafuji, Yasuaki Hayashi, Shinji Maekawa and Tatsuo Morita: Jpn. J. Appl. Phys. **33** (1994) pp.4191–4194.

7. *In Situ Ellipsometric Monitoring of Low Temperature Growth of Poly-Si Films by RF Plasma CVD*
   Tatsuru Shirafuji, Yasuaki Hayashi and Kunihide Tachibana: Mater. Res. Soc. Symp. Proc. **336** (1994) pp.73–78.

8. *Thickness Dependence of H Radical Treatment of Si Thin Films Deposited by Plasma-Enhanced Chemical Vapor Deposition Using $SiF_4/SiH_4/H_2$*
   Tatsuru Shirafuji, Hisao Kondo and Kunihide Tachibana: Jpn. J. Appl. Phys. **35** (1996) pp.2047–2051.

Short note

1. *Monte-Carlo Simulation of Surface Reactions in Plasma-Enhanced Chemical Vapor Deposition of Hydrogenated Amorphous Silicon Thin Films*
   Tatsuru Shirafuji, Wei-Ming Chen, Mikio Yamamuka and Kunihide Tachibana: Jpn. J. Appl. Phys. **32** (1993) pp.4946–4947.

Letter

1. *Low Density of Gap States in a-Si:H Deposited by Vacuum UV Direct Photochemical Vapor Deposition Method*
   Tatsuru Shirafuji, Masahiro Yoshimoto, Takashi Fuyuki and Hiroyuki Matsunami: Jpn. J. Appl. Phys. **30** (1991) pp.L538–L540.

International conferences

1. *a-Si:H Films by Direct Photo-CVD and Doping Characteristics*
   Hiroyuki Matsunami, Katsumi Tokuda, Tatsuru Shirafuji, Takashi Fuyuki and Masahiro Yoshimoto: Proc. 4th Int. Photovoltaic Sci. and Eng. Conf., Sydney, 1989 (IREE, 1989) pp.289–293.

2. *Low Hydrogen-Concentration a-Si:H Deposited by Direct Photo-CVD*
   Tatsuru Shirafuji, Masahiro Yoshimoto, Takashi Fuyuki and Hiroyuki Matsunami: Tech. Digest 5th Int. Photovoltaic Sci. and Eng. Conf., Kyoto, 1990 (PVSEC, 1990) pp.31–34.

3. *Photoelectric Properties of a-Si:H with Low Gap-States Deposited by VUV Photo-CVD*

Tatsuru Shirafuji, Masahiro Yoshimoto, Takashi Fuyuki and Hiroyuki Matsunami: Proc. 10th European Photovoltaic Solar Energy Conf. and Exhibition, Lisbon, 1991 (E-PVSEC, 1991) pp.420–423.

4. *In Situ Ellipsometric Monitoring of Growth of Amorphous and Polycrystalline Silicon Thin Films Deposited by RF Plasma CVD*
   Tatsuru Shirafuji, Yasuaki Hayashi and Kunihide Tachibana: Proc. 11th Int. Symp. Plasma Chem., Loughborough, 1993 (IUPAC, 1993) pp.817–822.

5. *In Situ Ellipsometric Monitoring for the Growth of Poly-Si Thin Films by RF Plasma Chemical Vapor Deposition*
   Tatsuru Shirafuji, Shinji Nakajima, Yasuaki Hayashi, Kunihide Tachibana, Shinji Maekawa and Tatsuo Morita: Proc. 2nd Int. Symp. Reactive Plasmas, Yokohama, 1994 (Organizing Committee of ICPR-2/SPP-11, 1994) pp.649–652.

6. *Roles of H Radicals in the Low Temperature Growth of Poly-Si Films by Plasma CVD Using $SiF_4/SiH_4/H_2$*
   Tatsuru Shirafuji, Kunihide Tachibana and Tatsuo Morita: Proc. 12th Int. Symp. Plasma Chem., Mineapolis, 1995 (IUPAC, 1995) pp.2125–2130.